

**Roles of plate locking and block rotation in the tectonics of the
Pacific Northwest**

Zuoli Ning

A dissertation submitted in partial fulfillment of the requirements for the degree of

Doctor of Philosophy

University of Washington

2003

Program Authorized to Offer Degree: Department of Earth and Space Sciences

UMI Number: 3111110

INFORMATION TO USERS

The quality of this reproduction is dependent upon the quality of the copy submitted. Broken or indistinct print, colored or poor quality illustrations and photographs, print bleed-through, substandard margins, and improper alignment can adversely affect reproduction.

In the unlikely event that the author did not send a complete manuscript and there are missing pages, these will be noted. Also, if unauthorized copyright material had to be removed, a note will indicate the deletion.

UMI[®]

UMI Microform 3111110

Copyright 2004 by ProQuest Information and Learning Company.


All rights reserved. This microform edition is protected against unauthorized copying under Title 17, United States Code.

ProQuest Information and Learning Company
300 North Zeeb Road
P.O. Box 1346
Ann Arbor, MI 48106-1346

©Copyright 2003

Zuoli Ning

In presenting this dissertation in partial fulfillment of the requirements for the Doctoral degree at the University of Washington, I agree that the Library shall make its copies freely available for inspection. I further agree that extensive copying of the dissertation is allowable only for scholarly purposes, consistent with "fair use" as prescribed in U.S. Copyright Law. Requests for copying or reproduction of this dissertation may be referred to Proquest Information and Learning, 300 North Zeeb Road, Ann Arbor, MI 48106-1346, to whom the author has granted "the right to reproduce and sell (a) copies of the manuscript in microform and/or (b) printed copies of the manuscript made from microform."

Signature:  _____

Date: Dec. 05. 2003

University of Washington
Graduate School

This is to certify that I have examined this copy of a doctoral dissertation by

Zuoli Ning

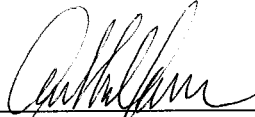
and have found that it is complete and satisfactory in all respects,
and that any and all revisions required by the final
examining committee have been made.

Chair of Supervisory Committee:

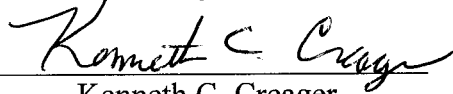


Anthony Qamar

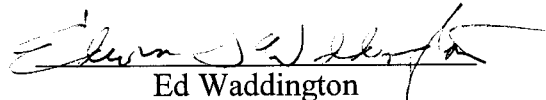
Reading Committee:



Anthony Qamar



Kenneth C. Creager



Ed Waddington

Date: Dec. 05, 2003

University of Washington

Abstract

Roles of plate locking and block rotation in the tectonics of the Pacific Northwest

Zuoli Ning

Chair of the Supervisory Committee:
Professor Anthony Qamar

Department of Earth and Space Sciences

The Pacific Northwest has potential for huge megathrust earthquakes. The influence of plate locking in the Cascadia subduction zone dominates crustal deformation off the shores of Washington and Oregon, but does not much affect areas far from the trench. The maximum principal strain rate ϵ_1 is -0.013 ± 0.007 $\mu\text{strain/yr}$ in the Olympic Peninsula, 0.007 ± 0.005 $\mu\text{strain/yr}$ in the Puget Sound, -0.005 ± 0.005 $\mu\text{strain/yr}$ at Mt. Rainier, -0.004 ± 0.005 $\mu\text{strain/yr}$ along the northern Oregon coast, and 0.011 ± 0.006 $\mu\text{strain/yr}$ in central Oregon. The minimum principal strain rate ϵ_2 is -0.083 ± 0.008 $\mu\text{strain/yr}$ N56°E in the Olympic Peninsula, -0.034 ± 0.007 $\mu\text{strain/yr}$ N63°E in the Puget Sound, -0.020 ± 0.006 $\mu\text{strain/yr}$ N53°E at Mt. Rainier, -0.051 ± 0.014 $\mu\text{strain/yr}$ N85°E along the northern Oregon coast, and -0.010 ± 0.006 $\mu\text{strain/yr}$ N71°E in central Oregon. A new model of plate locking on the Cascadia subduction zone is similar to a model (1997). The uncertainty of the widths of the locked and transition zone in the model is about 25km - 40km.

Guided by computed site velocities, seismicity patterns, heat flow, volcanic data, and geological structures, we find it is necessary to divide the crust in the Pacific Northwest into separate moving blocks. We have analyzed a model in which the Oregon block is separated from the Washington block at latitude 46°. The Washington block has been further divided into 5-subblocks, three in the forearc and two in eastern Washington. We remove contributions of JDF plate locking from the site velocity field and determine a rotation pole and a strain rate for each sub-block. We conclude that Juan de Fuca plate locking has little direct effect on crustal earthquake occurrence in the Pacific Northwest (except for periodic

megathrust earthquakes). In the Oregon block, plate locking and rigid block rotation are sufficient to explain GPS observations and the lower rate of seismicity in Oregon. The Washington block is more. The southwestern Washington sub-blocks have higher rotation rates and smaller residual strain rates than the northern sub-blocks. The Olympic sub-block shows the greatest north-south compression ($0.017 \mu\text{strain /yr}$). The Puget Lowland sub-block and Mt. Rainier sub-block are shortening along a NNE direction, roughly consistent with the direction of maximum principal stress from fault plane solutions. The overall north-south shortening across the Puget Sound is 3mm/yr , sufficient to generate M7+ earthquakes in the future. NS compression dominates eastern Washington near Yakima which is also consistent with principal stress directions derived from fault plane solutions. Northeast Washington sub-block is currently poorly constrained by GPS data.

As western Washington is pushed northward against the British Columbia, block rotation in Oregon is slowed down in Washington and the motion produces NS compression in northern Washington. The sub-blocks in southwestern WA act as a transition zone between Oregon and British Columbia. Residual strain rate is proportional to crustal seismicity. The great variation of residual strain rate in WA compared to Oregon may explain their crustal seismicity difference. GPS derived velocities in NE Washington are still too uncertain to determine the details of block rotation and strain rate there.

TABLE OF CONTENTS

LIST OF FIGURES	III
LIST OF TABLES.....	V
CHAPTER 1: INTRODUCTION.....	1
1.1 OBJECTIVES.....	1
1.2 INTRODUCTION	2
1.2.1 <i>Tectonic Overview</i>	3
1.2.2 <i>Seismicity</i>	8
1.2.2.1 Earthquake History.....	8
1.2.2.2 Earthquake spatial distribution	11
1.2.3 <i>Overview of Cascade volcanoes</i>	13
1.2.4 <i>Geological overview</i>	16
CHAPTER 2: GPS DATA COLLECTION AND PROCESSING.....	24
2.1 INTRODUCTION	24
2.2 GPS HISTORY.....	24
2.3 MAIN FEATURES OF GPS	24
2.4 GPS WORKING PRINCIPLES	26
2.5 GPS DATA COLLECTION	29
2.6 GPS DATA PROCESSING.....	33
2.6.1 <i>Pre-Processing</i>	34
2.6.2 <i>Processing</i>	40
2.6.3 <i>Post processing</i>	43
CHAPTER 3: MODEL OF CASCADIA SUBDUCTION ZONE	48
3.1 INTRODUCTION	48
3.2 THEORY OF ELASTIC DISLOCATION MODELING	49
3.3 TWO DIMENSIONAL MODELING OF SURFACE DEFORMATION.....	50
3.4 THREE DIMENSIONAL MODELING	51
3.5 INVERSE THEORY.....	52
3.6 PREVIOUS STUDIES OF THE CASCADIA SUBDUCTION ZONE	57
3.7 MODEL CONSTRUCTION	59
3.7.1 <i>Data resources</i>	59
3.7.2 <i>Geometry parameter sensitivity</i>	60
3.7.3 <i>Three-dimensional inverse modeling</i>	63
3.7.4 <i>Geometry uncertainty of Cascadia subduction zone</i>	66
3.8 SUMMARY	68
CHAPTER 4: RIGID BLOCK ROTATION AND STRAIN ANALYSIS	71
4.1 INTRODUCTION	71

4.2 BASIC THEORY	71
4.3 RIGID-BLOCK ROTATION.....	73
4.4 PREVIOUS STUDIES.....	75
4.5 DATA RESOURCES AND ANALYSIS	77
4.6 STRAIN RATE AND TRANSLATION VELOCITY CALCULATION.....	78
4.7 RIGID BLOCK ROTATION IN OREGON AND WASHINGTON.....	82
4.8 WHERE ARE THE BLOCK BOUNDARIES?	87
4.9 STRAIN RATE AND BLOCK ROTATION	93
CHAPTER 5: DISCUSSION.....	97
5.1 INTRODUCTION	97
5.2 THE CASCADIA SUBDUCTION ZONE (CSZ).....	97
5.2 RIGID-BLOCK ROTATION IN OREGON.....	104
5.4 KINEMATICS IN WASHINGTON.....	108
5.4.1 <i>Introduction</i>	108
5.4.2 <i>Rigid body rotation in Washington</i>	108
5.4.3 <i>Residual strain analysis in Washington</i>	112
5.5 FURTHER DISCUSSION	119
5.6 POSTGLACIAL REBOUND.....	120
CHAPTER 6: CONCLUSION	122
FUTURE WORK	125
BIBLIOGRAPHY	127
APPENDIX A. OCCUPATION HISTORY OF CAMPAIGN SITES.....	142

List of Figures

Figure Number	Page
1.1	2
1.2	4
1.3	5
1.4	6
1.5	9
1.6	12
1.7	13
1.8	14
1.9	15
1.10	17
1.11	18
1.12	19
1.13	20
1.14	23
2.1	30
2.2	31
2.3	32
2.4	44
2.5	45
2.6	46
3.1	48
3.2	51
3.3	51
3.4	52
3.5	53
3.6	58
3.7	59
3.8	60
3.9	61
3.10	62
3.11	64
3.12	67
3.13	68
4.1	74
4.2	75

4.3	<i>The observed site velocity field in the Pacific Northwest</i>	77
4.4	<i>Principal strain rates in the Pacific Northwest</i>	79
4.5	<i>Smoothed translation vectors in the Pacific Northwest</i>	81
4.6	<i>Vectors shown here are the residual velocities</i>	83
4.7	<i>Residuals after removing contributions</i>	84
4.8	<i>Assume Washington</i>	85
4.9	<i>Residuals in the Pacific Northwest</i>	86
4.10	<i>Theoretical site velocities resulted from two estimated poles</i>	87
4.11	<i>Seismicity and sub-block separation</i>	88
4.12	<i>Bouguer gravity map of the Puget</i>	90
4.13	<i>Cross section of earthquake hypocenters centered</i>	91
4.14	<i>Residual vectors of averaged site velocities</i>	96
5.1	<i>Depth contours on the top of the Cascadia subducting slab</i>	99
5.2	<i>Depth distribution of earthquakes</i>	101
5.3	<i>Predicted contribution of plate locking</i>	102
5.4	<i>Residuals after removing contributions</i>	104
5.5	<i>Site velocity residuals in Oregon</i>	106
5.6	<i>Residual strain rate in the vicinity of the Klamath mountains</i>	107
5.7	<i>Relative motion on boundaries between sub-blocks</i>	111
5.8	<i>Map showing locations of earthquakes</i>	114
5.9	<i>Horizontal projection of the maximum principal stress axis</i>	115
5.10	<i>Earthquake magnitude versus cumulative frequency</i>	116
5.11	<i>Number of earthquakes (1985 – 2001) as a function of depth</i>	117
5.12	<i>Horizontal projection of the maximum principal stress axis</i>	118
5.13	<i>Orientations of P axes</i>	119
5.14	<i>Tectonic setting of the northern Cascadia subduction zone</i>	120
6.1	<i>Sensitivity of vertical surface velocity</i>	126

List of Tables

Table Number	Page
2.1	26
2.2	34
2.3	35
2.4	36
2.5	37
2.6	38
2.7	39
2.8	40
2.9	41
2.10	46
3.1	61
3.2	67
4.1	92
4.2	94
4.3	95
5.1	109
5.2	110
5.3	110
5.4	113
5.5	113

Acknowledgments

This dissertation would not have been possible without other people's help. First I would like to thank my research advisor Anthony Qamar for his time, energy, patience, and advice over the years here as a graduate student. I also would like to thank Kenneth Creager for his time, advice, and support. Ed Waddington also gave me some advice over the years here. Kelin Wang gave me permission to use his programs and some good suggestions. I would like to thank them all here. I also would like to thank Robert McCaffrey for his discussion with me and letting me use his data.

Second, I would like to thank all the following agencies to let me use their data: the U.S. Geological Survey (USGS), the Pacific Northwest Geodetic Array (PANGA), the U.S. Coast Guard CORS Array, the IGS, the NGS HARN (National Geodetic Survey High Accuracy Reference Network), the Western Canada Deformation Array (WCDA) of the Geological Survey of Canada (GSC), the University of Washington (UW), the Rensselaer Polytechnic Institute (RPI), and the Oregon State University (OSU).

My wife, Xian Liu, and my parents are very dear to me and without their support and love over the years, none of this would be possible.

Chapter 1: Introduction

§1.1 Objectives

The surface of the earth is composed of eight major tectonic plates and many minor plates. Their interactions produce many natural events near their boundaries, such as mountain folding in the Himalaya Mountains, volcanic eruptions, and earthquakes. Some of the physical mechanisms that produce these events are still unknown. Fortunately in the Pacific Northwest we have a natural “backyard laboratory”, the Cascadia Subduction zone between the young and hot Juan de Fuca (JDF) plate, and the overriding North America (NA) plate. However, because plate motions are very slow (millimeters per year), it is very hard to monitor their movement using traditional techniques. Today the Global Positioning System (GPS) provides an efficient way to understand plate tectonics and some associated natural disasters. The primary goal of this thesis is to use high precision GPS measurements, inverse theory, and strain analysis techniques to understand the nature of plate interaction in the Pacific Northwest. The computed crustal deformation is used to constrain the kinematics and dynamics of the continental lithosphere, and strain accumulation in the Pacific Northwest. This thesis addresses the following scientific questions:

- ◆ What is the deformation velocity field and its spatial distribution in the Pacific Northwest?
- ◆ What is the regional strain pattern and what is its relation to the Cascadia Subduction Zone (CSZ)?
- ◆ What are the tectonic driving processes that affect the geodetic observations and what is their relative importance?
- ◆ How are the geodetic data related to seismological and geological data?
- ◆ How does the rotation of western Oregon and Washington change in northern Washington and southern British Columbia?
- ◆ What are the boundaries and what is the kinematics of crustal blocks comprising the forearc and how is the geodetic strain related to block boundaries?
- ◆ What is the role of the Cascades in regional tectonics?

§1.2 Introduction

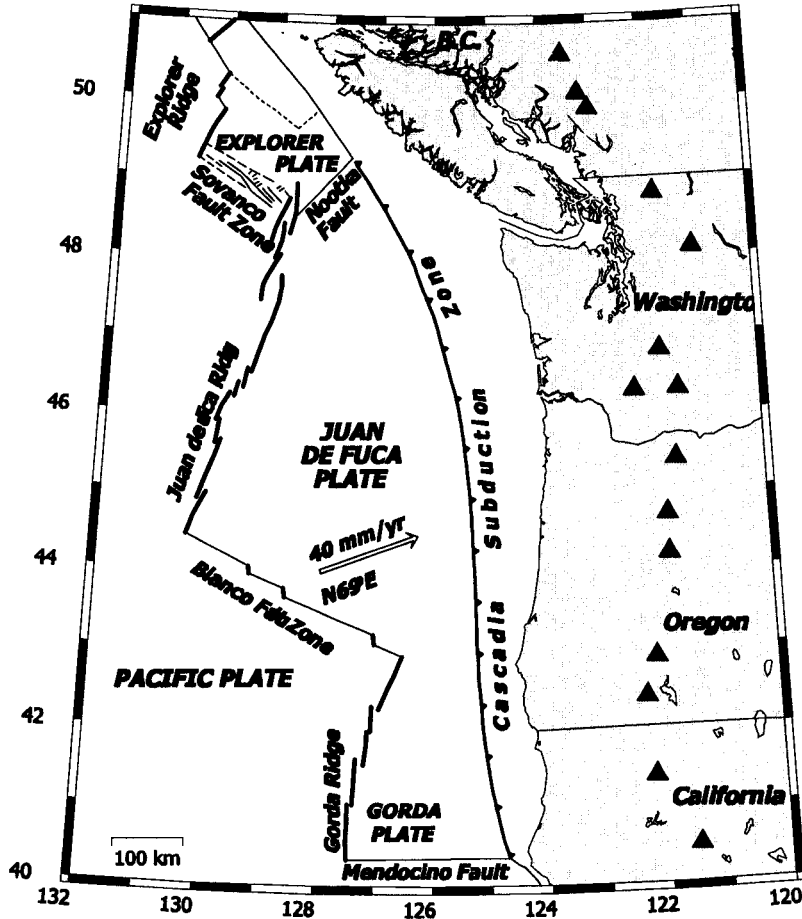


Figure 1.1. Map of the Pacific Northwest. The triangles are major volcanoes. The arrow indicates the convergence of the Juan De Fuca plate relative to the North America plate.

My research area is Cascadia in the Pacific Northwest which comprises southern British Columbia (Canada), Washington, Oregon, and northern California. It includes a part of the North America plate boundary and the fore-arc of the only subduction zone in the conterminous U.S (Figure 1.1). Thus it is an ideal place to study the relationship between the subduction zone earthquake cycle, crustal earthquakes, and the behavior of a magmatic arc. Before presenting my results, I will first describe tectonic, seismological, volcanic, and geological overviews of this area. In chapter V, I will provide some interpretations that combine geodetic observations with geology, tectonics and seismicity.

§1.2.1 Tectonic Overview

The Pacific Northwest (PN) region addressed in this thesis is bounded on the north and south by two small plates, the Explorer and the Gorda (Figure 1.1) and on the east by Idaho. This region deforms in response to complex North America (NA), Juan de Fuca (JDF), and Pacific plate (PP) boundary interactions. As a result of these interactions, the small Juan de Fuca plate has been subducting under the NA plate for 35M year (*Engebretson et al.*, 1984) and produces the Cascadia subduction zone, the only subduction zone in the continental U.S. The plate system has a history of complex motion in the late Cenozoic. The oblique convergence rate (relative to the North America plate) changes, to various degrees, along the continent margin (*Atwater*, 1970; *Wells et al.*, 1998). It decreased from 6-7cm/yr 7Ma ago to the present comparatively slow rate of 4.4cm/yr in the direction N62°E (*Riddihough*, 1984). The NUVEL-1A global plate motions model predicts an average convergence rate between these plates at Seattle be 40 mm/yr in the direction N70°E (*DeMets et al.*, 1990; 1994). Since the JDF is relatively small, the oceanic crust produced at the JDF ridge doesn't have to travel a long time before subducting at the trench. Thus, the subducting slab, with a moderate thickness about 6 km (*Parsons et al.*, 1998), is very young at the deformation front, approximately 8M years. Thermal arguments and elastic dislocation models indicate that the boundary between the NA and PP plates has a completely locked part and a partially locked part that together make up the seismogenic zone (Figure 1.2). The down-dip boundary of the locked zone lies offshore and varies in width and depth (*Dragert et al.*, 1994; *Mitchell et al.*, 1994; *Wang et al.*, 1994; *Hyndman and Wang*, 1993, 1995; *Verdonck*, 1995; *Fluke et al.*, 1997; *McCaffrey et al.*, 2000). The dip angle of the subducting plate changes not only along the margin, where it varies between 5° and 15°, but also increases normal to the margin where it varies from 2°-7° to 12° where it encounters a 20km thick Siletz terrane or other accreted oceanic crust (*Parsons et al.*, 1998). The temperatures at the deformation front, the boundary between the locked zone and transition zone, and the downward end of the seismogenic zone are about 250°C, 350°C, and 450°C respectively (*Hyndman and Wang*, 1993) (Figure 1.2). Although "Benioff zone" earthquakes in the Pacific Northwest occur at a depth of no more than 100 km, other evidence such as tomography indicates that the slab of the JDF plate penetrates to 400-600 km depth beneath Washington, but rarely reaches that depth below Oregon (*Rasmussen and Humphreys*, 1988; *Bostock and VanDecar*, 1995). The shape and varied tectonic regime of the

margin may be related to a number of second-order effects, including arching of the Juan de Fuca plate beneath the Olympic Mountains and the Puget Sound (*Crosson and Owens, 1987; Weaver and Baker, 1988*) and inherited heterogeneity in the overlying North American plate (*Trehu et al., 1994; Wells, 1994*). There is evidence for a depressed Moho beneath the central Cascade ranges in Washington (*Crosson and Owens, 1987*).

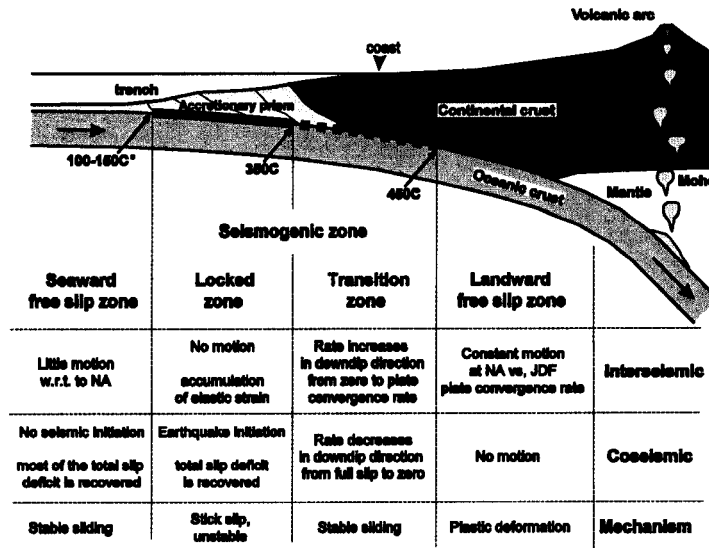


Figure 1.2 The subducting slab scheme. The arrows are the directions of the oceanic plate movement. The table gives properties for different zones. The dark-grey area is the NA continent while the upper part of the subducting slab is light grey. Extracted from *Flück, 1996*.

Parallel to the margin of the continent, the Cascadia volcanic arc is characterized by a cluster of volcanoes that separate the Pacific Northwest into three parts longitudinally. To the west the fore-arc encompasses the coast range (CR), the Olympic Mountains, and the densely populated Puget-Willamette Lowland. The arc comprises the Cascade range and associated mountains. The back-arc lies to the east of the Cascade Mountains.

Using evidence about uplift rate, geometry of the arc--fore-arc--trench system, seismic character, volcanic activity, heat flow data and paleomagnetic studies (*Beck et al., 1986; Blackwell et al., 1990; Ludwin et al., 1991; Mitchell et al., 1994; Trehu et al., 1994; Weaver and Baker, 1988*), the CSZ can be segmented into three distinct parts latitudinally (*Figure 1.3*): a northern part in Washington, a central part in Oregon, and a southern part in north-central California. The northernmost segment is characterized by the presence of a “compressional” volcanic arc, high seismic activity, low magmatic extrusion rate, low heat flow, folded basement and small blocks

in the forearc west of the Cascade Range. In this segment, the seismogenic zone of the CSZ is wide, up to 200km at the Olympic Peninsula, and the oceanic plate is not subducting steeply (Flüke *et al.*, 1997). To the north at Vancouver Island the convergence becomes much more margin - normal and the subduction is slightly oblique at Washington transect.

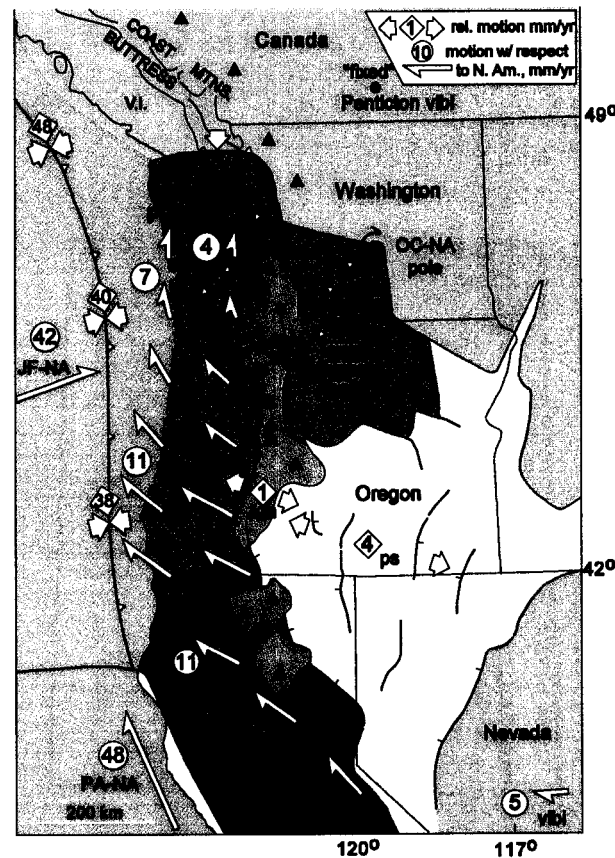


Figure 1.3: Major tectonic units along the Cascadia subduction zone. From south to north, the forearc is divided into three tectonic blocks/segments: Sierra-Nevada (SN); Oregon Coastal (OC) and Washington (W). Thick arrows indicate observed relative rates from very long baseline interferometry, paleoseismology and magmatic spreading. Figure is adapted from Wells *et al.* (1998).

In the north segment of the CSZ the northward migration of the forearc is resisted by a “backstop” of the pre-tertiary rocks of the Canadian Coastal Mountains. This causes the northern section of the forearc to be broken into small blocks which undergo large vertical motions due to the continuing north-south compression which in return generates significant structural units such as the Tacoma, Seattle, Everett, and Port Townsend basins in the Puget lowland (Brocher *et al.*, 2001). These units are associated with low gravity, indicating the presence of thick (5-10 km) low density sedimentary layers (Blakely and Jachens, 1990; Finn, 1990; Pratt *et al.*, 1997). The

associated negative gravity anomalies are separated from the surrounding gravity highs by steep gradients, with remarkably linear geometry, suggesting that these basins are separated from each other by east-west oriented faults (*Gower et al., 1985; Brocher et al., 1999*) (Figure 1.4). One of the faults is the Seattle fault, comprising three or more fault strands over a 4~7 km wide zone (*Johnson et al., 1994, 1999; Pratt et al., 1997*) which can presumably generate a M7.7 crustal earthquake (*Pratt et al., 1997*). The Seattle and Tacoma fault zones together bound the Seattle uplift, one of the E-W pop-up structures underlying Puget Lowland from the Black Hills to the San Juan Islands (*Brocher et al., 1999, 2001*).

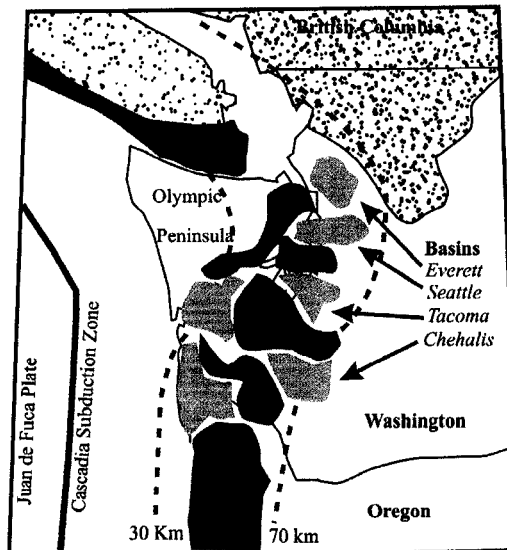


Figure 1.4. Schematic map of gravity anomalies in western Washington and northern Oregon. Gravity lows are indicated by light grey and highs by dark grey. The stippled area is pre-Tertiary basement in British Columbia that is also exposed in the North Cascades of the US. The gravity lows and highs are separated by faults that have undergone considerable vertical motion producing basins such as the Seattle Basin. The southern boundary of the Seattle Basin is the so-called Seattle fault. The dashed line shows depth contours on the top of the subducted portion of the Juan de Fuca plate, which lies below North America.

Paleomagnetic evidence suggests that southwestern Washington is rotating in a similar way to the western Cascades of Oregon, indicating that clockwise Miocene-age rotation extends northward into Washington and eastward into the axis of the arc (*Hagstrum et al., 1999*). The right-lateral St. Helens and West Rainier seismic zone take an important position in regional tectonism (*Hagstrum et al., 1999; Moran et al., 1999*) and may form a diffuse eastern boundary of the migrating fore-arc terrane. To the east of the arc, the Yakima fold and thrust belt with long, narrow, regularly spaced anticlinal folds and thrust faults is thought to be an analog of planetary wrinkle ridges (*Watters, 1992; Mege et al., 2001*).

The central segment of the CSZ is located in Oregon, and is characterized by currently aseismic oblique subduction, large forearc rotation, low seismicity, high magma extrusion, an “extensional” arc, and the presence of an axial graben in the Cascade range (Figure 1.3). The Oregon forearc, west of the Cascades, behaves as a rigid semi-block rotating clockwise (*Goldfinger et al.*, 1997; *McCaffrey & Goldfinger*, 1995; *Wells*, 1990; *Wells et al.*, 1998; *McCaffrey et al.*, 2000; *Savage et al.*, 2000; *Wells et al.*, 2001; *Svarc et al.*, 2002) with a rotation pole on the eastern Oregon/Washington boundary (*McCaffrey et al.*, 2000; *Wells et al.*, 2001). Due to extension from the eastern Basin Range and Cascade arc, and the shear motion of the Sierra Nevada block, the rotation of the forearc causes western Oregon to move towards the subduction trench and away from the arc, as well as migrate northward, producing compressional deformation in Washington where the block rotation meets some resistance. In this model the Cascades arc defines the long-term and major tectonic boundary between the rotating fore-arc and the extensional Basin and Range province. The Oregon volcanic arc has little seismicity, similar to a slow-spreading oceanic ridge. The southwestern and northeastern boundaries of a structural basin now occupied by Portland, Oregon and Vancouver, Washington are the Portland Hills fault zone and the Frontal fault zone, respectively, and they exhibit clear aeromagnetic anomalies (*Blakely et al.*, 1995). The central segment of the CSZ is thought to move in response to tectonic activity in eastern California and the Basin and Range of northwestern Nevada, and eastern Oregon and provides a connection between the seismically active zones of northern California and southern and central Washington.

The third segment of the CSZ is a short section located in northern California (Figure 1.3). It includes the seismically active and rapidly deforming Mendocino triple junction region (*McCrorry*, 1995; *Velasco et al.*, 1994), and is characterized by a transpressive arc with high rates of seismicity, a high magma extrusion rate, and small forearc rotations (*Wells et al.*, 1998). The shear motion of the Sierra Nevada block is accommodated by roughly 12 mm/a in the Eastern California shear zone (*Argus & Gordon*, 1991; *Sauber et al.*, 1994, *Pezzopane et al.*, 1993). The Eastern California shear zone and its northern extension, the Walker Lane and Central Nevada seismic belt, splays into the Pacific Northwest (*Pezzopane et al.*, 1993).

All three segments of the CSZ are kinematically linked (*Wells*, 1990; *Wells et al.*, 1998); they may

also be dynamically linked (*Satake et al.*, 1996; *Wells et al.*, 1998). Their boundaries are not exactly defined. The clockwise rotation of the middle segment broadly accommodates extension behind the southern segment and transpression behind the northern segment.

§1.2.2 Seismicity

Seismicity gives valuable insight into the tectonics of the Pacific Northwest. First, Benioff – Wadati zone seismicity can be used to define the location of the Cascadia subducting slab, a critical factor in modeling crustal strain. Second, the seismicity pattern reveals seismically active areas and quiet areas which can help us define crustal block boundaries when combined with other tectonic and geological evidence. Third, earthquake mechanisms help us understand the stress systems that produce the tectonics.

§1.2.2.1 Earthquake History

The Pacific Northwest is subject to three types of earthquakes: A) shallow crustal earthquakes occurring in the overriding NA crust; B) deeper intra-slab earthquakes within the subducting JDF plate; and C) Inter-plate subduction earthquakes that occur along the interface between the JDF and NA plates (Figure 1.5). Subduction does not proceed as a smooth and continuous process; it happens in fits and starts. When the locked part of the subduction zone accumulates sufficient strain energy on either side of the fault, the energy may be released as a catastrophic subduction earthquake.

Due to the lack of historic recording of megathrust earthquakes, the CSZ was thought to be aseismic for some time. After comparison with other similar subduction zones having huge historic earthquakes such as southwestern Japan and southern Chile, *Heaton & Kanamori* (1984) concluded the CSZ was capable of producing huge megathrust earthquakes. The most compelling evidence for such megathrust earthquakes come from geologic studies of marine estuaries along the coast of the Pacific Northwest (e.g. *Atwater et al.*, 1995). The most recent such earthquake was a magnitude 9 event which occurred in 1700 AD and apparently ruptured the entire CSZ from Vancouver in British Columbia to northern California (*Atwater et al.*, 1995; *Satake et al.*, 1996; *Clague*, 1997, 1999). Radiocarbon and tree ring dating of the buried soils and tsunami deposits in Washington and Oregon reveal a recurrence interval of approximately 500 years for

great CSZ earthquakes (*Atwater et al.*, 1991; *Yamaguchi et al.*, 1997). However, intervals between the most recent seven events ($M \geq 8$) range from less than 200 years to 700-1300 years, indicating that the interval is not uniform (*Clague*, 1997, 1999). Holocene sediments from Lake Washington near Seattle show that more than 30 depositional events have occurred in the past 12,000 years, and 21 disturbances happened after the deposition of the Mt. Mazama ash about 7,600 year ago. If all events were caused by earthquakes, the recurrence interval of major earthquakes on the Seattle fault and/or the CSZ is about 300 – 400 years (*Karlin et al.*, 1996). The largest earthquake in the 150 – year written history of Washington and Oregon was probably

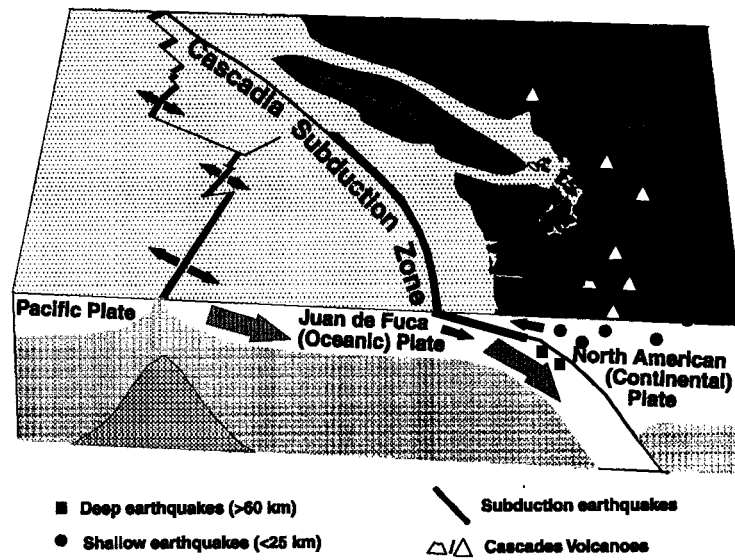


Figure 1.5. 3D view of three types of earthquakes. The paired arrows indicate the spreading of oceanic ridge. The shaded arrows represent the motion of the subducted oceanic plate.

the magnitude 7.4 Cascade earthquake of 1872 (*Malone & Bor*, 1979). Based on the number of aftershocks, the general character of current seismicity in eastern Washington, and intensity pattern of the main shock, the hypocenter of the 1872 earthquake was estimated to lie within the NA crust. The largest historical deep earthquake was the 1949 M7.1 event with depth 54 km near Olympia. It caused eight deaths and \$150M (in 1984 dollars) damage (*Noson et al.*, 1988). In 2001, a M6.8 earthquake occurred at nearly the same location at a depth of 52km, and caused considerable damage to roads, buildings, bridges, parks, etc. In 1965, a M6.5 earthquake with a depth of 60km occurred between Tacoma and Seattle, causing 7 fatalities and \$50M (in 1984 dollars) damage (*Noson et al.*, 1988, *Ludwin et al.*, 1991). These types of events are classified as

intra-plate or intra-slab earthquakes and are included in the “Wadati - Benioff” zone of seismicity that helps to constrain the geometry of the JDF plate beneath the North American continent. The M5.8 1939 earthquake, the M6.1 1946 earthquake, the 1995 M5.0 earthquake at Robinson Point at a depth of 20km (*Dewberry and Crosson, 1996*), and the 1997 M 4.9 event at a depth of 7 km beneath Point White on southwestern Bainbridge Island are all examples of crustal earthquakes in the Puget Sound. Their occurrence indicates that the Seattle fault remains active and raises the possibility of a repeat of a major ($M > 7$) earthquake that happened 1100 years ago and resulted in 7m of uplift at Restoration Point near Seattle (*Bucknam et al., 1992*).

Further north, the South Whidbey Island fault shows a similar potential for a major shallow earthquake. The 6 to 7 km wide fault zone shows evidence of both strike-slip (right-lateral) and thrust offset (*Johnson et al., 1996*). Like the Seattle fault, the South Whidbey Island fault displays over 400m of offset on the base of Quaternary sediments and can presumably generate earthquakes bigger than M7.

At the northern margin of Cascadia, a peaty marsh soil near Tofino and Ucluelet shows evidence of coastal subsidence indicating a great earthquake between 100 and 400 years ago that affected Vancouver Island, British Columbia (*Clague et al., 1994*). Three layers of sand within a sequence of muddy gyttja on the central coast of Vancouver suggests three plate-boundary earthquakes on the CSZ about 2600, 1600 and 300 years ago. It is estimated that during the earthquakes less than half of the interseismic uplift was recovered (*Hutchinson et al., 2000*). The latest magnitude seven earthquakes in central Vancouver Island were the 1918 M7.0 and the 1946 M7.2 events which occurred in sparsely populated areas and thus caused little damage (*Yelin et al., 1994*).

By using buried marsh soil at Sixes River estuary, southern Oregon, *Kelsey et al. (2002)* checked for evidence of plate boundary earthquakes and tsunamis of the past 5500 years. The 6000-year-long stratigraphic record revealed a suite of at least 11 buried marsh soils, suggesting an average recurrence interval of CSZ boundary earthquakes of ~510 years. The youngest buried soil at the mouth of the river subsided during the A.D. 1700 Cascadia earthquake (*Satake et al., 1996; Jacoby et al., 1997; Yamaguchi et al., 1997*). However, not all CSZ boundary earthquakes

have ruptured the entire subduction zone and some have triggered local upper-plate folding (*Kelsey et al.*, 2002). In 1873, a M7.3 earthquake occurred near the California - Oregon coast and most likely was located on the CSZ or within the NA plate (*Bakun*, 2000).

There is additional strong geologic evidence for subsidence, tsunamis, and ground shaking from major earthquakes along the CSZ and in the forearc region (*Adams*, 1990; *Atwater*, 1987; *Atwater et al.*, 1995; *Dariento et al.*, 1995; *Nelson et al.*, 1995). In addition, geodetic data indicates ongoing crustal deformation in the Pacific Northwest (*Rielinger and Adams*, 1982; *Savage and Lisowski*, 1991; *Savage et al.*, 1981). Modeling of the CSZ using GPS data suggests strain energy is accumulating and will be released in a future mega-earthquake (*Dragert et al.*, 1994; *Flück et al.*, 1997; *Hyndman and Wang*, 1995; *Savage et al.*, 1991). The subduction zone thus poses a significant seismic hazard to the densely populated areas in the Pacific Northwest, such as the greater Seattle and Portland metropolitan areas and rapidly developing communities along the west flank of the Cascades (*Heaton and Hartzell*, 1987; *Heaton and Kanamori*, 1984).

§1.2.2.2 Earthquake spatial distribution

Figure 1.6 shows seismicity in the Pacific Northwest from 1971 – 2002. A noticeable feature of this figure is the general decrease of seismic activity south of 45° north latitude. Washington state is clearly more seismically active than most of Oregon. Every year more than 1,000 earthquakes are recorded in Washington, although most of them are small. A dozen or more reported earthquakes are felt each year (*Noson et al.*, 1988). Most seismicity concentrates in the Puget Sound and the western Cascade Range between west longitude 121.5° and 123.0°, and north latitude 45° and 49° (Figure 1.6). West of the Cascades, most earthquakes have depths between 0 and 30km. East of the Cascades, depths are shallower, 0-15km. In the Olympic Peninsula there are few crustal earthquakes. Events with depth more than 55km are not very common (Figure 1.7). The presence of the CSZ slab can be seen in this figure because the earthquake hypocenters are believed to occur within the top of the subducting plate (*Crosson et al.*, 1987; *Leiph Preston*, Pers. Comm.). Two prominent linear zones are the nearly 90km long, northwest-oriented Saint Helens seismic zone (SHZ) and the West Rainier seismic zone (Figure 5.8). A M5.5 earthquake occurred in the SHZ's middle section in 1981. Two earthquakes (M4.8 and M5.1) occurred at the

SHZ's southern end in 1961. Earthquakes on the SHZ are shallower than in Puget Sound. Seismicity in eastern Washington occurs mainly on the western side of the Columbia basin and along the eastern flank of the Cascade Range, approximately between 119°W and 121°W, 46°N and 47°N. Most earthquake depths there are less than 8km. Outside of the Columbia basin, some seismicity exists between Chelan and Wenatchee. Although Spokane has very sparse seismicity, a M4.0 and a M3.3 earthquake occurred within the city in Nov., 2001.

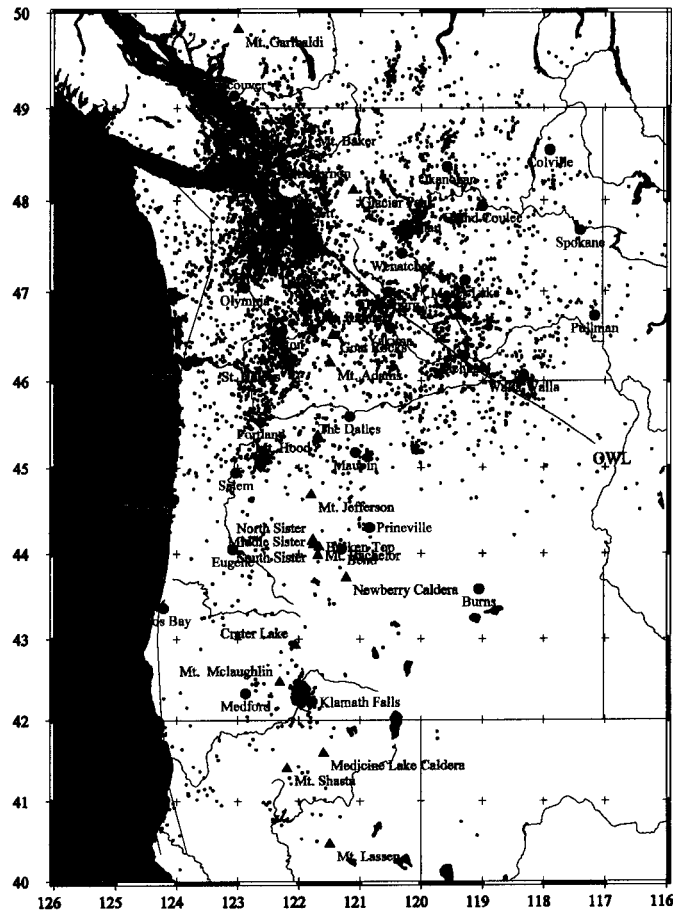


Figure 1.6 Seismicity pattern in the Pacific Northwest. Events with magnitude larger than 1.5 were used here. All events are from The Pacific Northwest Seismograph Network (PNSN) from 1971 to 2002

Compared to Washington, Oregon has much less seismicity. Portland has experienced some earthquakes with depths of 15-20km. The biggest earthquake occurred in 1962, M5.2. In northeast Oregon, the activity decreases and earthquakes are shallow. Seismicity in central and southern Oregon has been low historically, except for a swarm of earthquakes including M5.1, and M5.0 events near Adel in 1968, and M5.9 and M6.0 earthquakes near Klamath Falls in 1993.

§1.2.3 Overview of Cascade volcanoes

The major Cascade volcanoes lie in a 1000 mile long, generally less than 75 km wide zone from southern British Columbia to northern California. Two are in British Columbia, six are in Washington, fifteen are in Oregon and four are in California. The average eruption rate in the Cascades is about 1-2 times per century during the last 4000 years (Figure 1.8). Since volcanic processes vary along the Cascade arc, researchers have separated the arc into several segments. The typical approach is to define segments based on the alignment of active stratovolcanoes (e.g., *Hughes et al.*, 1980), the areal distribution of volcanism and seismicity, or a combination of these (*Weaver et al.*, 1985). In Hughes's scheme segment boundaries are based on normal faulting,

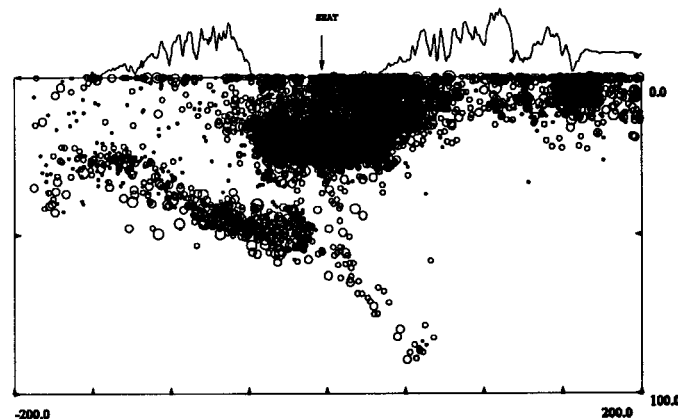


Figure 1.7 East-west cross section of seismicity through Seattle from 1969 to 2002. The arrow points to Seattle. The terrain elevation is exaggerated vertically. The left side is West. The units for both axes are kilometers. Events between 47°N and 48° were used in this figure. Earthquakes with poor quality have not been filtered out.

shallow seismicity, basaltic cinder cones, and catastrophic large eruptions. *Guffanti and Weaver* (1988) used the spatial, temporal, and compositional distribution of approximately 4000 volcanic vents in Washington, Oregon, northern California, and northwestern Nevada in the last 16Ma, especially 2821 vents formed in the last 5Ma, to segment the Cascade Range into six parts (Figure 1.9). The first segment includes the Meager Mountain volcanic complex, and Mount Garibaldi in British Columbia, and Mt. Baker and Glacier Peak in northern Washington. The Meager Mountain volcanic complex is the northernmost volcano in the Garibaldi Volcanic Belt which is dominated by plagioclase porphyritic andesite to rhyodacite lava and pyroclastic breccias. Mt. Garibaldi is notable both for its excellent internal structure exposures and for its striking topographic anomalies. Mt. Baker is the most heavily glaciated of the Cascade volcanoes

after Mt. Rainier. Although fumarolic activity at Mt. Baker has increased from 1975 to the present, there are no other changes suggesting that magma movement is involved (*Gardner, et al., 1995*). Glacier Peak is the most remote volcano in Washington and not remarkably visible from any city. But it produced the most explosive eruption in the state 11,000 years ago. The most recent eruption was about 300 years ago (*Mastin & Waite, 2000*).

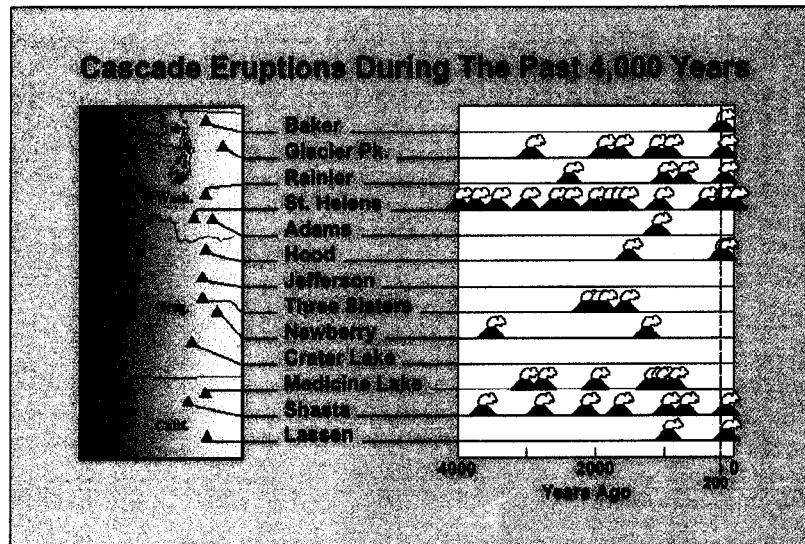


Figure 1.8 Cascade volcanoes and their history in recent 4000 years (from *USGS/Cascades Volcano Observatory*)

The second volcanic segment according to *Guffanti and Weaver (1988)* extends from Mt. Rainier to Portland, Oregon, and is dominated by large stratovolcanoes. Mt. Rainier is the highest and third-most voluminous volcano in the Cascades after Mounts Shasta and Adams. It is also the most dangerous volcano because it is close to the Seattle-Tacoma metropolitan area and because it possesses a huge volume of ice and snow on its flanks. The last eruption was 150 years ago. Mt. Adams, one of the largest volcanoes in the Cascade Range, dominates the Skamania, Yakima, Klickitat, and Lewis county areas. It has been quiet for the past few thousand years and has not erupted frequently (Figure 1.8). Mt. St. Helens, the youngest volcano among the Cascade volcanoes has erupted most frequently and is just 50 miles away from Portland. It is a composite and very active volcano and erupts explosively, thus posing extreme danger to nearby life and property. Mt. Hood is the highest mountain in Oregon and one of the most-often-climbed peaks in the Pacific Northwest, just 75 miles away from Portland. Its most recent eruption occurred 1,500 years ago.

The third volcanic segment extends from south of Mt. Hood to the vicinity of the Oregon-California border. In this segment, Mt. Jefferson has erupted repeatedly for hundreds of thousands of years. It has been quiet for some time since its last eruptive episode during the last major glaciation, 15000 years ago.

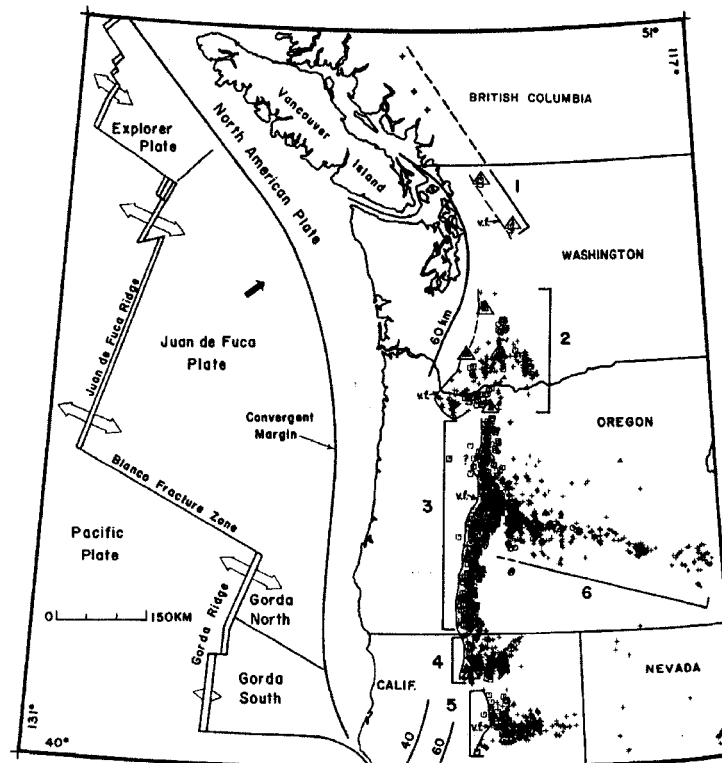


Figure 1.9 Volcanic segmentation of the Cascade arc based on vents less than 5 MA. Open arrows show ridge-spreading directions. Solid arrow shows the motion of the Juan de Fuca plate relative to the North America plate. Numbers and bold brackets refer to segments. Dashed ends mean uncertainty. The 60 km contour shows depth of seismicity in the Juan de Fuca plate (Weaver and Baker, 1988). The figure is adopted from *Guffanti & Weaver, 1988*.

The fourth volcanic segment comprises Mt. Shasta and Medicine Lake volcano in California and their surrounding vents. Segment five includes the Lassen Peak area and is spatially isolated from the rest of the Cascade Range. Volcanic segment six is formed by vents of the High Lava Plains along the northern margin of the Basin and Range province in Oregon and is not clearly connected with the Cascade arc (*Guffanti et al., 1988*).

The axis of the Cascade Range parallels the strike of the JDF subducting plate and is perpendicular to the direction of convergence between JDF and NA plates. The first segment is

characterized by the presence of isolated strato-volcanoes and low rates of volcanic extrusion. Segment two is wider and marked by the presence of basaltic vents on both sides of the andesitic arc. The orientations of segment one and two change from north-west in northern Washington to north-east in southern Washington, parallel to the 60km depth contour of the subducting slab (Figure 1.9). Between the two segments, there is a 90km wide volcanic gap possibly due to the fact that the landward portion of the subducting slab beneath Puget Sound had a very small dip angle ($<10^\circ$) due to the arching of the Juan de Fuca plate. The volcanic front of segment one is farther east of the 60km contour than that of segment two, probably because of the steeper dip of the oceanic slab under segment two. Segment three is characterized by a dense distribution of andesitic vents and a seismically quiet portion of the subduction zone. The narrowness of this segment may indicate a steep dip of the subduction plate beneath the Cascade Range in Oregon. In the Basin and Range province, volcanism migrated to its current position in the Cascade 10-5Ma ago. Since 5Ma, the westward migration of the Basin-Range is evident from the cessation of volcanism in southern Oregon, the continuation of volcanism in northeastern California and the decrease of mafic volcanism around Mt. Shasta, Medicine Lake, and Lassen Peak (Guffanti *et al.*, 1988; Blackwell *et al.*, 1990).

Based on the distribution of late Cenozoic volcanism, many proposed tectonic models assume that the difference in the amount of observed volcanism is the result of the difference in interaction between the NA plate and the subducting JDF plate. Such models postulate that volcanism at isolated major stratovolcanoes in Washington and British Columbia results from compression in the NA crust and that widespread volcanism in Oregon reflects crustal extension there (Weaver *et al.*, 1983, 1985; Rogers, 1985). In such models the stress difference was thought to come from 1> the velocity variation of convergence between NA and JDF plates along the subduction margin (Rogers, 1985) and the dip angle variation of the oceanic subducting slab (Weaver *et al.*, 1985; Michaelson *et al.*, 1986), and 2> the extension of Basin and Range (Priest *et al.*, 1983; Smith *et al.*, 1984).

§1.2.4 Geological overview

Based on gross geological features, the Pacific Northwest is divided into four parts, two outboard

units: the *Cascadia Accretionary Wedge* (CAW) and the *Coast Range* (CR), and two inboard units: the *North America Basement* (NAB) and the *Cascade Volcanic Arc* (CVA) (Figure 1.10).

The CAW underlies most of the offshore continental margin east of the trench (*Clowes et al.* 1987) and formed outboard of the coast range terrane. It is widely thought to be generated by frontal accretion and underplating starting around ~ 35 Ma (*Brandon et al.*, 1990, 1998; *Batt et al.* 2001). In Washington, the CAW includes the Olympic subduction complex (OSC) which has been locally

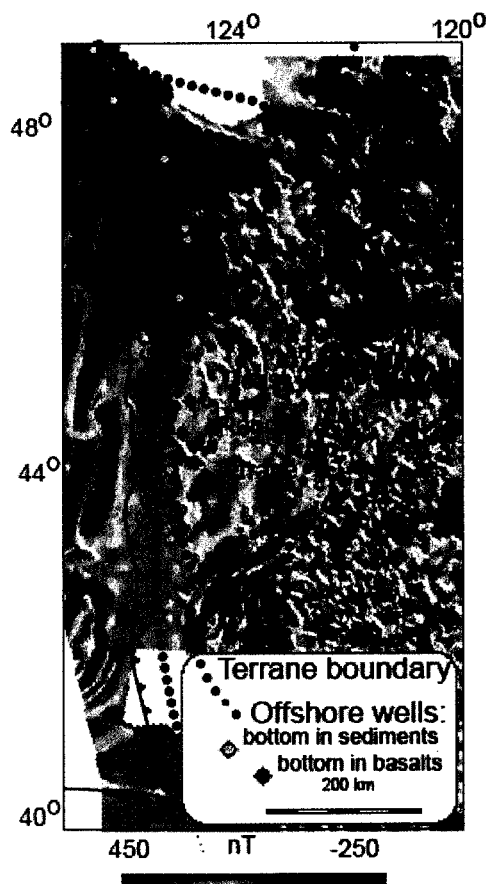


Figure 1.10: Geologic units in the Pacific Northwest. Dotted line delineates approximate outline of main geologic terranes along the CSZ: *North America Basement* (NAB), the *Coast Range* (CR), *Cascade Volcanic Arc* (CVA) and the *Cascadia Accretionary Wedge* (CAW) including the Olympic Subduction Complex (OSC). Filled circles show the location of offshore wells. Blue circles indicate wells bottoming in sediments and red circles bottoming in basalts. Figure adopted from *Wells et al.* (1998).

uplifted since ~ 18 million years ago and exposed in the core of the Olympic uplift (*Tabor and Cady*, 1978). The uplift and erosion have tilted the Peripheral sequence into a steep east-plunging anticline (*Tabor and Cady*, 1978). The driving force of the uplift results from both accretion and wedge deformation (*Brandon et al.* 1992, 1998). The short-term uplift is very fast in the

Olympics, ranging from 1.2 ~ 3.2 m/ka, with the highest rate along the west side (*Pazzaglia et al., 2001*). The exposed accreted sediments are hard, well - lithified rocks.

The OSC mainly consists of a relatively competent and homogeneous assemblage of sandstones & mudstone (*Tabor and Cady, 1978*). The Hurricane Ridge fault (HRF) separates the OSC from coast range terrane (Figure 1.11, 1.12). *Tabor and Cady 1978* divided the OSC into 5 major litho - tectonic units mainly based on sandstone petrology. *Brandon et al. (1998)* used detailed fission - track data to study the exhumation processes occurring in the Olympic Mountains, and used these data together with geological mapping to define three regional units called upper, lower, and coast units. The upper unit is dominated by Eocene clastic sediments, mainly turbidite sandstone

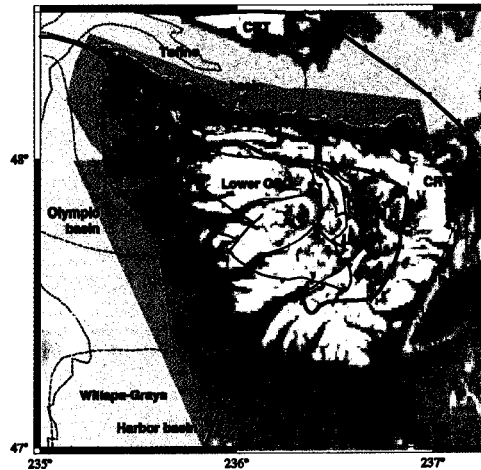


Figure 1.11 The three units in the Olympic Peninsula. The dashed red lines enclose young basins surrounding the Olympic Mountains uplift, and the black dotted line shows the shelf edge. Abbreviations: Lw.—lower; Up.—upper; CRT—Coast Range terrane; OSC—Olympic subduction complex; PL—Puget Lowland, SJF—Straits of Juan de Fuca; WL—Willamette lowland; GL—Georgia lowland; NF—Nitnat submarine fan; and AF—Astoria submarine fan. Figure is reproduced from *Brandon et al. 1998*.

and subordinate mudstone, with exposed pillow basalts stratigraphically and compositionally identical to Crescent basalts and related to the Coastal Range Terrane (CRT). The lower unit is solely composed of clastic sediments of late Oligocene and early Miocene age. The coastal unit is a Miocene accretionary unit and mainly consists of turbidites, mudstone, and minor pillow basalts. The similarity of the basalt blocks and the Crescent formation suggests that basalt blocks might have been generated by submarine landsliding from overlying Coast Range terrane (Figure 1.11). The low dip angle of subduction slab beneath the Olympics resulted in a relatively early emergence of this region and rapid uplift of the Olympic massif comparing with adjacent regions

of the subduction zone (Pazzaglia *et al.*, 2001). Using deformed erosional benchmarks to estimate long-term permanent strain rates, Pazzaglia and Brandon 2001 disproved major margin – parallel deformation across the Olympics. Batt *et al.* 2001 also concluded that margin – parallel transport does not play a significant role in driving uplift of the Olympics.

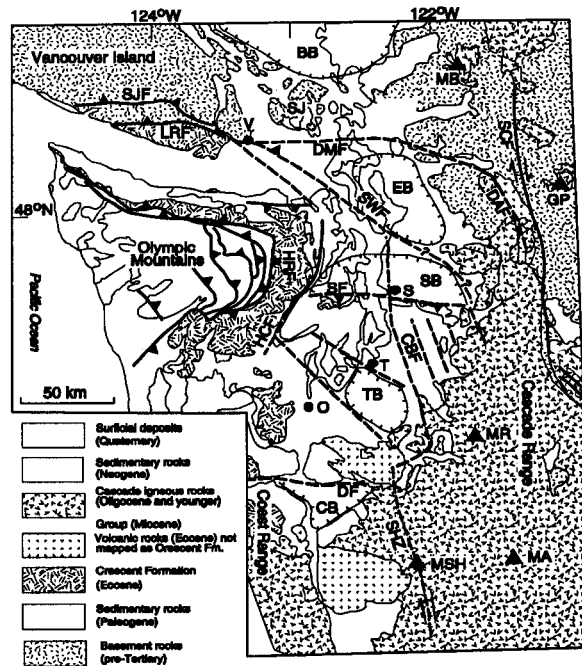


Figure 1.12: Schematic geologic map of western Washington. Abbreviations for cities (black circles): O = Olympia; MP = Mt. Persis; S = Seattle; T = Tacoma; TM = Tiger Mt.; V = Victoria. Abbreviations for faults (heavy lines): CBF = Coast Range boundary fault; DAF = Darrington fault; DF = Dotty fault; DMF = Devils Mountain fault; HCF = Hood Canal fault; HRF = Hurricane Ridge fault; LRF = Leech River fault; SCF = Straight Creek fault; SF = Seattle fault; SWF = Southern Whidbey Island fault. Abbreviations for Cenozoic sedimentary basins (enclosed hachured areas): BB = Bellingham basin; CB = Chehalis basin; EB = Everett basin; SB = Seattle basin; TB = Tacoma basin. Abbreviations for modern Cascade volcanoes (triangles): GP = Glacier peak; MA = Mt. Adams; MB = Mt. Baker; MR = Mt. Rainier; MSH = Mt. St. Helen. See Figure 1 in Johnson *et al.* (1999) for more details.

In the central Oregon subduction zone, the main features are a set of late Quaternary thrust faults and folds. These faults extend parallel to the deformation front and from the front to the continental high (Peterson *et al.*, 1986; Goldfinger *et al.*, 1992b). Goldfinger *et al.* (1997) used sidescan sonar, seismic reflection profiles, and swath bathymetric data and found nine WNW trending left-lateral strike-slip faults (Figure 1.13). Among them, five faults cross the deformation front and extend into the Juan de Fuca plate with a slip rate of 5.5 ~ 8.5 mm/yr obtained from offsets of subsurface piercing points and roughly dated submarine channels. The possible driving forces of these strike-slip faults might be the dextral shearing of the subduction slab. These faults propagate upward through the overlying accretionary wedge. The accreted sedimentary rocks are

thrust beneath some major eastward dipping boundary faults under the Coast Range (*Tabor and Cady, 1978; Snavely 1987*).

The second outboard unit, the Coastal Range (CR) terrane extends a distance of 750km from the Klamath mountains in northern California to the southern tip of Vancouver Island (*Clowes et al. 1987*). It covers most of the forearc west of the Cascades with a thick Eocene mafic basement which is locally called the Crescent Formation in Washington, Siletz terrane in Oregon, and Metchosin Volcanics in British Columbia (*Snavely et al., 1968; Irving, 1979*). The main rocks of the Siletz terrane are tholeiitic submarine pillow lavas and breccias which erupted locally as alkalic basalts (*Snavely et al. 1968; Duncan et al. 1991*). Its thickness varies along the margin, reaching a maximum of 24 – 32 km beneath west central Oregon (*Tréchu et al., 1994*). It thins to

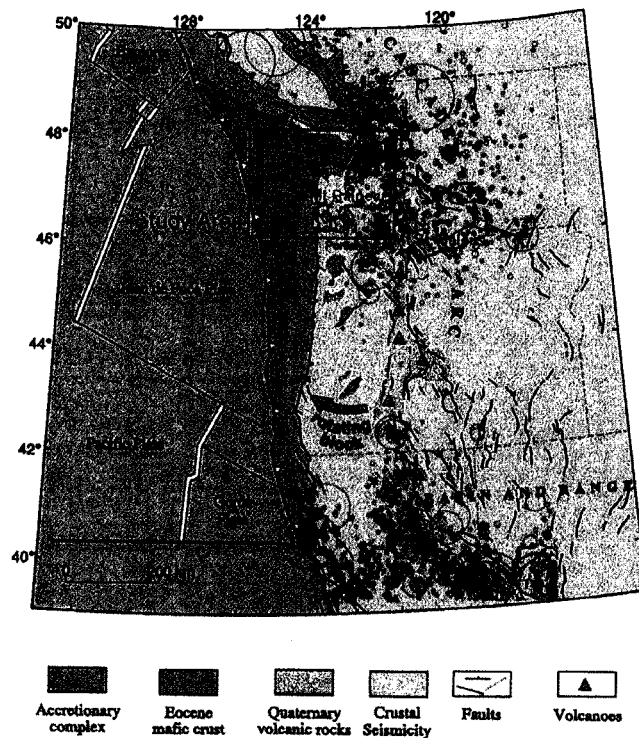


Figure 1.13. Major tectonic elements and geological features of the Cascadia subduction zone. There are important structural variations along the margin. The accretionary complex broadens progressively along the margin, reaching its widest point at the Olympic Mountains. Volcanic production is greatest in the central arc, where the seismicity rate is lowest. Extracted from *Parsons et al., 1999*.

20 km beneath northwestern Oregon and southwestern Washington (*Stanley et al., 1987; Tréchu et al., 1994; Parsons et al., 1998*), the same thickness as oceanic crust beneath the pre-Tertiary terranes of Vancouver Island (*Hyndman et al., 1995*). This variation in thickness influences

long-term and short-term deformation in the forearc, and the thickest part rotates as a coherent block (*Wells et al.*, 1984; *Tréchu et al.*, 1994; *Parsons et al.*, 1998; *Wells et al.*, 1998). The ophiolitic basement of the CR may have originated as an oceanic plateau or by backarc or forearc oblique marginal rifting with a complex subsequent emplacement history (*Wells* 1984; *Clowes et al.*, 1987). The CR generally has gentle to horizontal attitude except near the Olympic Peninsula where it is steeply dipping and overturning, and wraps around the mountains. The deformation of the CR reflects the prolonged uplift and exhumation of the Olympics (*Tabor and Cady* 1978a, 1978b). The Eocene submarine and subaerial tholeiitic basalt in the Olympics is thought to be the exposed mafic basement of the Coast Range. In southern Washington, multiple accretionary structures were generated during late Mesozoic and early Tertiary plate convergence (*Stanley et al.* 1990); and an electrically conducting body (conductor) up to 15km thick was formed as a sequence of Paleogene marine sedimentary rocks. The conductor's western boundary is the 90-km-long, 5~15-km-deep, northwest oriented St. Helens seismic zone (SHZ), which is thought to be the eastern boundary of the CR.

The central and northern Oregon coast mainly consists of westward – dipping (around 60°) Tertiary sedimentary rocks (*Fleming & Tréchu*, 1999). These rocks form the west flank of a structural high from latitude 43° to 45° north which acts as a west boundary of the Coast Range. This N-S trending, roughly 200km long silver is buried beneath the accretionary complex and is derived possibly from the following sources: a “silver” detached from main Siletz terrane; imbricated and thickened subducted oceanic crust that is in place; an aseismic ridge rafted in on the subducting crust; and a series of ridges and/or seamounts rafted in for a long time and transferred from the subducting crust to overlying plate (*Fleming & Tréchu*, 1999). The dextral strike – slip fault, referred as the Coast Range boundary fault (CBF), along the eastern margin of the rifted Coast Range high with different lithology, basin evolution, and potential – field defines the CR's inland boundary (*Johnson* 1984a; *Johnson et al.*, 1994; *Finn et al.*, 1990). The isostatic residual gravity shows a long, north – south gravitational depression lying near the western limit of the Western Cascades and stopping around the Oregon/Washington boundary. This depression defines the CBF's Oregon part (*Johnson et al.*, 1996). After crossing several faults on southeastern Puget Lowland, the CBF connects with the southern Whidbey Island fault (*Johnson*

et al., 1996) and extends farther north to merge with west – trending Leech River fault in Vancouver Island (*Clowes et al.*, 1987).

The Puget Lowland – Willamette Valley comprises discontinuous basins extending from Puget Sound to southern Oregon. In Washington, these basins are the Grays Harbor, Astoria, Chehalis, and Puget Sound basins. They are filled with sedimentary sequences eroded from the Olympic mountains. Puget Sound is cut by east – west striking folds and faults formed in Mid – Cenozoic time (*Johnson 1984a; Johnson et al.*, 1994).

The North America Basement (NAB in Figure 1.10), a rigid part of NA continent, originated from pre-Tertiary (Mesozoic and Paleozoic) rocks sutured to NA sometime in the Jurassic and Cretaceous (*Monger et al.*, 1982).

The *Cascade Volcanic Arc* is a Tertiary-to-recent magmatic arc and was formed approximately 38 Ma years ago (*Heller, 1987*) as a consequence of subduction. In the northern Cascades, the volcanoes are Quaternary stratovolcanoes that rest on Tertiary crust. In southern Washington, the Cascades are a transitional zone characterized by unconformably folded Quaternary composite volcanoes. In Oregon, the composite volcanoes rest on a broad platform of Pliocene and Holocene mafic lava flows (*Guffanti and Weaver, 1988*).

The Cascades of Washington and Oregon are characterized by high heat flow, 80 – 100 mWm⁻². Heat flow in northeastern Washington is greater than 70 mWm⁻² and in southeastern Washington it is 60 mWm⁻². In the fore-arc area of Washington the heat flow is below normal and averages 40 mWm⁻². The highest heat flow, 80 mWm⁻², is along the axial region that coincides with the India Heaven, Mt. Adams, and Goat Rocks centers of Quaternary volcanism (Figure 1.14) (*Blackwell et al.*, 1990a). In the Oregon fore-arc, the heat flow is 40 – 50 mWm⁻². In the Cascade Range in Oregon, the heat flow is about 100 mWm⁻² (*Blackwell et al.*, 1990b). The region of low heat flow in Washington is wider than in Oregon, which is thought to correspond to trench-arc separation, subducting plate dip and increased upper seismicity (*Gutscher et al.*, 2003). Based on heat flow, seismicity pattern, and well documented margin (*Henry and Pollack, 1988; Gutscher et al.*, 2000), *Gutscher et al.* (2003) suggested that the flat subduction between 46° and 49° has a causal relation

to the observed heat flow there.

A prominent alignment of topographic features starts from the northern edge of the Olympic Peninsula and extends to the southeast along the northeastern rim of the Willowa Mountains in northeastern Oregon. It is called the Olympic – Willowa Lineament (OWL) and is a wide zone first defined by Raisz in 1945. It consists of a series of north-west striking ridges and thrust faults and marks a northern boundary of the Yakima fold and thrust belt (*Reidel, 1984; Beeson et al., 1990; Wells et al., 1998*).

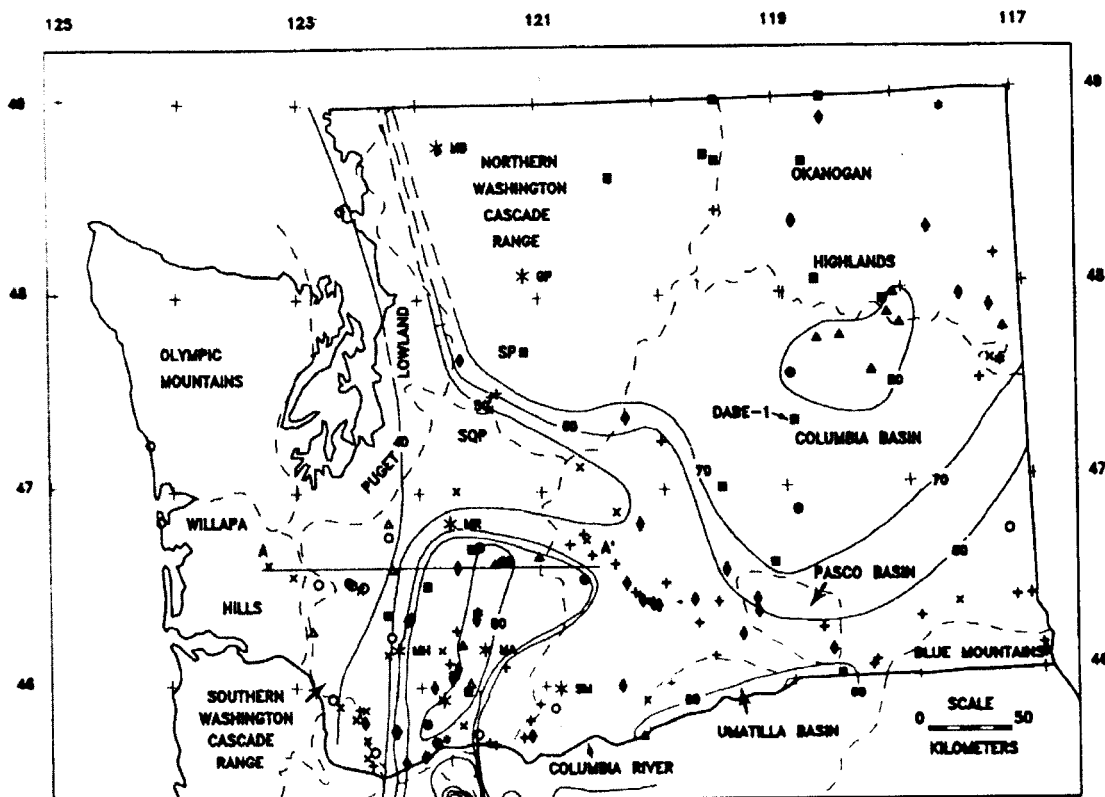


Figure 1.14 Heat flow map of Washington. Physiographic provinces are outlined with dashed lines and identified. The volcanoes in the Cascade Range (large asterisks with a two-letter identification) are also shown for reference. The map is contoured at 10 mWm^{-2} intervals. Heat flow symbols are triangle, $20\text{-}30 \text{ mWm}^{-2}$; circle, $30\text{-}40 \text{ mWm}^{-2}$; cross, $40\text{-}50 \text{ mWm}^{-2}$; plus, $50\text{-}60 \text{ mWm}^{-2}$; solid diamond, $60\text{-}70 \text{ mWm}^{-2}$; solid square, $70\text{-}80 \text{ mWm}^{-2}$; solid triangle, $80\text{-}90 \text{ mWm}^{-2}$; dot, $90\text{-}100 \text{ mWm}^{-2}$; star, $100\text{-}110 \text{ mWm}^{-2}$; small asterisk, $>100 \text{ mWm}^{-2}$. Figure is extracted from *Blackwell et al. (1990a)*.

Chapter 2: GPS Data Collection and Processing

§2.1 Introduction

GPS has many applications, and in geodesy, it can be used to monitor positions of permanent monuments with millimeter accuracy at sites around the world. Proper data collection and processing are critical to obtain such accuracy. In this chapter, first I will describe briefly the history of GPS, its main features, and its working principles. Then I will review the history of GPS data collecting and the procedures to process GPS data in the Pacific Northwest.

§2.2 GPS history

Space-based navigation has been pursued by the U.S. military and NASA since the early 1960s. One successful satellite positioning system was the Navy Navigation Satellite System (TRANSIT). However TRANSIT was terminated in 1996 because this system couldn't provide positions with high resolution. The satellites had low earth - orbits so they were affected by local gravity variations and the satellite transmission frequencies, at 150 and 400Mhz, were more susceptible to ionospheric disturbances and weather. Finally, each satellite was only visible for three hours at a time.

GPS was developed by the U.S. Department of Defense (DoD) to address these problems in 1978. The original purpose of GPS was military navigation and the system initially cost about 8 billion U.S. dollars. GPS gives the absolute position of any place on earth in real time. With improved GPS technology and the dramatic decrease in the cost of GPS receivers in the early 1990s, people began to use the system in a wide range of non-military applications. Because of its ability to get very high resolution at low cost compared to traditional trilateration methods, GPS is now the preferred tool to monitor crustal deformation.

§2.3 Main features of GPS

In order to get the position of a particular site, we need to install an antenna with a receiver that

can record signals from GPS satellites. The distance L between a satellite and a receiver equals the velocity of electromagnetic waves times the time the signal needs to travel from the satellite to the receiver. Given this distance, the position of the receiver is somewhere on a spherical surface of radius L whose center is at the satellite. Theoretically three satellites would be sufficient to determine the exact position of the receiver. However, because of uncertainty in the clock correction of the receiver, a fourth satellite is needed to determine the position plus clock correction. After 1993, a full constellation of 24 GPS satellites was achieved in orbits at an altitude of 20,200 km. Each of the six orbital planes, inclined at 55° to the equatorial plane, has 4 satellites. With this configuration one can use land-based GPS receivers to estimate the absolute position of any place on earth at any time.

Like the TRANSIT system, GPS transmits two carrier waves, L1 and L2. The L1's transmission frequency is 1575.42MHz, 154 times the "fundamental frequency", 10.23MHz. The L2's is 1227.60MHz, 120 times the fundamental frequency. The two carriers are modulated by the pseudorandom noise (PRN) P(Y) code and the coarse/acquisition C/A code. The P(Y)-code (wavelength $\lambda \approx 30$ meters) doesn't repeat itself for 37 weeks so that all satellites can transmit on the same carrier frequency and be distinguished. All codes are initialized once per GPS week at midnight on Saturday. The C/A code ($\lambda \approx 300$ meters) belongs to the family of Gold codes which can be utilized to rapidly distinguish signals simultaneously received from various satellites. The C/A code contains 1023 bits and its period is about one msec. It's available on the L1 carrier and can also be put on the L2 carrier (Table 2.1). The C/A code is the basis of Standard Positioning Service (SPS) which can provide an accuracy of 10 meters with 95% confidence with "Selective Availability" off (Leick, 1995). Selective Availability (SA) is a procedure that intentionally degrades the C/A code positioning capability to 100m but has not been in use for several years. For civilian applications SA degradation is effectively reduced by relative positioning of co-observing receivers and by making ample use of carrier phase observations. Compared with precise positioning service (PPS) available to the military, SPS's accuracy can be lowered by intentionally introducing artificial errors in the transmitted clock and broadcast satellite ephemeris by the DoD. However, Carrier phase signals and precise orbit information can be combined to calculate positions with high precision. This approach is always used in geodesy to

get a few mm accuracy in horizontal and 5-8 mm in vertical positioning (Khazarazde, 1999).

Table 2.1 Comparison of P(Y) code and C/A code (Leick, 1995)

	C/A	P(Y)
Chipping rate	1.023Mbps	10.23Mbps
Length per chip	293m	29.3m
Repetition	1 ms	1 week
Code type	Gold	Pseudo random
Carried on	L1	L1, L2
Feature	Easy to acquire	Precise positioning, jam resistant

§2.4 GPS working principles

From the last section, the distance (L_{rx}) between a receiver r and a satellite x can be computed as the following:

$$L_{rx} = v \times t_{rx} \quad (2.1)$$

v is the speed of electromagnetic waves, t_{rx} is the travel-time from the satellite to the receiver.

Since the path of GPS signal is not entirely in a vacuum, we need consider other factors like ionospheric and tropospheric delays. We also need to estimate clock errors of satellites and receivers. The carrier observable (L1 or L2) between receiver r and satellite x at time t can be expressed in units of distance as:

$$L_{rx} = \rho_{rx} + N_{rx} + I_{rx} + T_{rx} + C_{rt} - C_{xt} + M_{rx} + m_{rx} \quad (2.2)$$

ρ_{rx} is the true distance between a satellite and a receiver.

N_{rx} is an integer number of phase bias expressed in terms of wavelengths between a satellite and a receiver. The procedure to get this number is called bias-fixing or ambiguity resolution. One approach to estimate N_{rx} is to use “double differences” based on “single difference” observation which uses the difference in the N_{rx} observable at two receivers recording signals from the same satellite. The difference is independent of the satellite. Then one can use the same two receivers

to record signals from another satellite which will give us another single difference. Combining these two single differences, we can form a double difference observation independent of both satellite and receiver by subtracting one from another. For a detailed theoretical description, refer to P255 – P263 in Leick (1995). For more information about algorithms and implementation, refer to Blewitt (1989).

I_{rxt} is a distance equivalent to an ionospheric time delay of the signal which equals:

$$I_{\text{rxt}} = \frac{40.30}{f^2} \text{TEC} \quad (2.3)$$

f denotes the carrier frequency and TEC is the total electron content which can be calculated by the following equation:

$$\text{TEC} = \int_{\text{path}} N_e ds \quad (2.4)$$

The TEC represents the number of free electrons in a 1-square meter column along the path in units of (e/m²). N_e is the local electron density with units of (e/m³). From (2.3) we can see that signals with higher frequency are delayed less than lower frequency signals, so L2 will be delayed more than L1. Using the typical TEC value and combining phase measurements at L1 and L2 frequencies, we can get an ionosphere free observable (denoted as LC) by removing the first order ionosphere delay (2.5). This approach requires dual-frequency receivers which are more expensive than single frequency ones.

$$LC = \frac{f_1^2}{f_1^2 - f_2^2} L_1 - \frac{f_2^2}{f_1^2 - f_2^2} L_2 = 2.546L_1 - 1.546L_2 \quad (2.5)$$

Here, f_1 and f_2 are L1 and L2's carrier frequencies.

T_{rxt} is a distance term due to atmospheric (troposphere, tropopause, stratosphere) time delay.

Since the atmosphere is neutral and non-dispersive, its impact (refraction) does not depend on frequency and, consequently, affects both the code modulation and the carrier phases in the same way and can't be eliminated by using dual frequency receivers, unlike the ionosphere time delay. This delay depends on atmosphere temperature, humidity and pressure, and varies with height. Like I_{rx} , T_{rx} can be calculated by using the tropospheric refractivity (N_T):

$$T_{\text{rx}} = \int_{\text{path}} N_T ds \quad (2.6)$$

Based on an empirical formula including meteorological parameters, we have:

$$N_T = (77.624 \frac{p}{T} - 12.92 \frac{e}{T} + 371900 \frac{e}{T^2}) 10^{-6} \quad (2.7)$$

Here p denotes the total atmospheric pressure in mbar, e represents the partial pressure of water vapor in mbar, T is the surface temperature in Kelvins. The first term in (2.7) represents the dry atmosphere which contributes about 90% of the total tropospheric refraction and can be modeled to about 2-5% based on the laws of ideal gases using surface temperature and pressure (Leick, 1995). The second and third terms are for wet components and are hard to model due to turbinate water vapor variations (Blewitt, 1993). Fortunately their contributions are only about 10% of N_T and can be modeled to within 2-5 cm by assuming an exponential vertical profile (Leick, 1995).

C_{rt} and c_{xt} are distance factors caused by satellite and receiver clock errors. Although the accuracy of satellite cesium atomic clocks is relatively high, clock oscillation drift still exists. GPS receivers use less stable quartz crystal oscillators and, consequently, have clocks with a higher drift rate. "Double differencing" is one way to eliminate most clock errors, but not the only way. Stochastic techniques can also be used to estimate clock errors by using a "white noise" model (Blewitt, 1993).

M_{rx} is caused by signal scattering or reflecting near the antenna. Signals from satellites that travel along slightly different paths will arrive at the antenna at different times. Some of the signals enter the antenna after reflecting or scattering and can be recorded by the receiver together with

direct arriving signals at the same time. This phenomenon is called multipathing. Signals from satellites near the horizon are more susceptible to multipathing. Although much antenna design work has been done to prevent signals below a horizontal plane through the antenna, reflecting or scattering from antenna edges is still a big problem.

m_{rx} accounts for errors which can be classified into two categories: random errors and systematic errors. It includes errors from antenna mis-calibrations, reference point mis-measurements, antenna mis-leveling, local weather, and ground instability. For example, alternate wet and dry conditions can cause a tripod to go out of balance, slightly moving the antenna.

§2.5 GPS Data collection

In this study, GPS data come from two sources: permanent GPS sites and temporary “campaign” GPS sites. Compared with campaign sites, permanent sites have the following advantages: continuous recording 24 hours a day, high precision data (the RMS scatter of estimated positions is small), fewer and more stable sources of errors which can be eliminated in data processing, and short term data availability during all phases of the earthquake cycle. However, they also have some disadvantages: they have high installation cost, and are often widely spaced. The spacing is often filled in with campaign sites. Since the late 1980s GPS has played a more and more important role in the study of the earth. Due to the diversity of GPS applications and continued growth in the number of GPS sites (especially after the early 1990s when receiver cost was dramatically decreased and GPS analysis techniques were more sophisticated), the international scientific community was urged to set up international standards for GPS data acquisition and analysis, and deploy and operate a common and comprehensive global tracking system. As a part of this effort, the International GPS Service (IGS) based on worldwide continuous GPS sites was established in 1993 by the International Association of Geodesy. It comprises networks of tracking stations (Figure 2.1) analyzed by at least three IGS analysis centers for the purpose of computing precise satellite orbits, seven data centers including operational, regional, and global data centers, and analysis and associate analysis centers.

It also includes an analysis coordinator, working groups and pilot projects, a central bureau, and a

governing board. IGS provides the following products:

- High accuracy GPS satellite ephemerides
- Earth rotation parameters
- Coordinates and velocities of the IGS tracking stations
- GPS satellite and tracking station clock information
- Ionospheric information
- Tropospheric information.

These products are available for download via the internet and are critical to get high precision estimation of positions for crustal deformation monitoring.

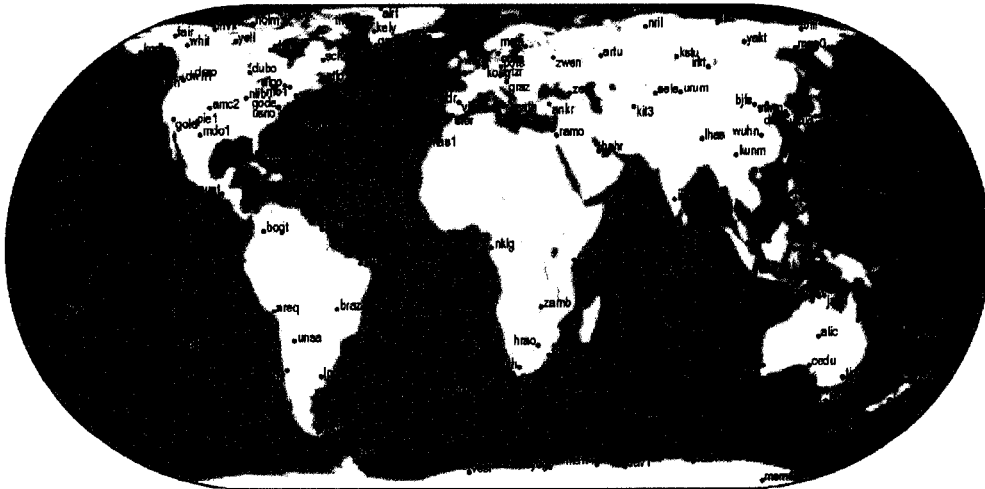


Figure 2.1 IGS worldwide continuous GPS stations. From IGS <http://igsceb.jpl.nasa.gov/network/globals.html>

Today, numerous continuous GPS arrays are operating worldwide. The largest one is in Japan (Kato et al., 1998). In the United States, the National Geodetic Survey's CORS (Continuously Operating Reference Stations) program comprises a nationwide network of permanently operating GPS sites (Figure 2.2). In the Pacific Northwest, the Geological Survey of Canada built up the first permanent GPS array in southern British Columbia, called the Western Canada Deformation Array (WCDA) (Dragert et al., 1995). The University of Washington (UW) installed site SEAT on the university campus and site NEAH near Neah Bay in the Olympic Peninsula in 1995, the first continuous GPS sites in Washington State. In 1996, the US Coast Guard and the

National Geodetic Survey set up an additional three permanent GPS sites: FTS1, WHD1, RPT1.

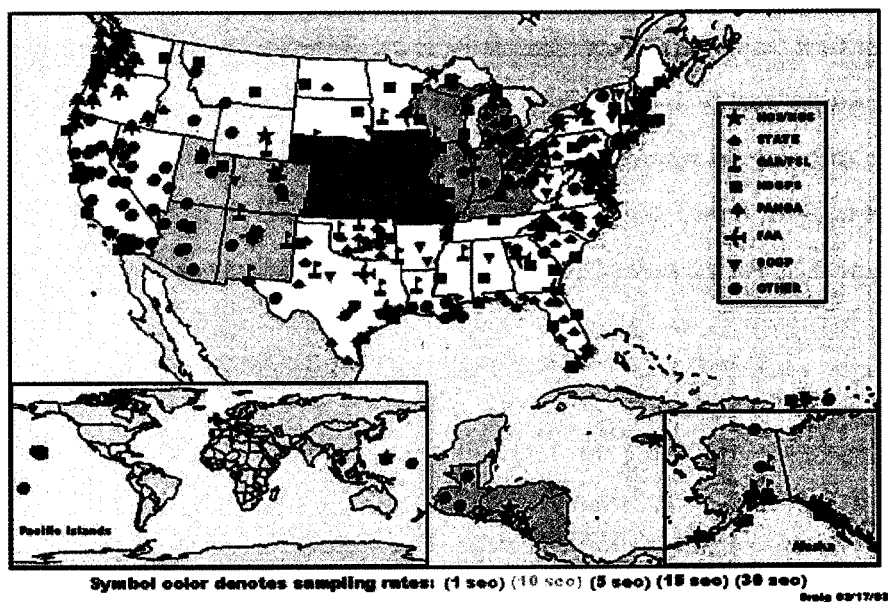


Figure 2.2 Coverage of permanent GPS stations in the CORS program in the U.S. From <http://www.ngs.noaa.gov/CORS/>

In order to promote and coordinate the efficient collection, analysis, interpretation of high precision deformation measurements using GPS, and further study the characteristics that determine how active tectonics leads to earthquake and volcanic hazards in Northern California, Oregon, Washington, and British Columbia, the regional Pacific Northwest Geodetic Array (PANGA) was established in 1997. It comprises instruments operated by WCDA, UW, Oregon State University (OSU), Central Washington University (CWU), the US Geological Survey (USGS), and Rensselaer Polytechnic Institute (RPI). Currently, it has 17 permanent sites and has a data processing center located at Central Washington University. In the upcoming Plate Boundary Observatory (PBO) project, many new continuous GPS sites will be installed in the Pacific Northwest.

Besides permanent sites, many temporary campaign GPS sites were surveyed in the Pacific Northwest, beginning in 1986. In 1994 there was a joint UW/USGS survey. UW has carried out six independent GPS surveys in Washington State from 1995 to 2000. In 2001, UW cooperated with Rensselaer Polytechnic Institute, and the Geological Survey of Canada, and surveyed campaign sites in Oregon, Washington, and British Columbia. Besides a re-survey of existing

sites, we also added many new benchmarks in northeastern Washington, the Olympic peninsula, and British Columbia. For each survey in a particular year the campaign sites were generally occupied at least twice. Each occupation took about eight hours, sometimes, several days. At safe sites the receiver can be left alone and picked up after eight hours; otherwise, an observer is required to stay with the instrument, a time consuming process. We occupied more than 300 sites from 1994 to 2001. Sites having GPS data spanning two years or more were processed for this study (Figure 2.3). For the survey history at each site, please refer to Appendix A.

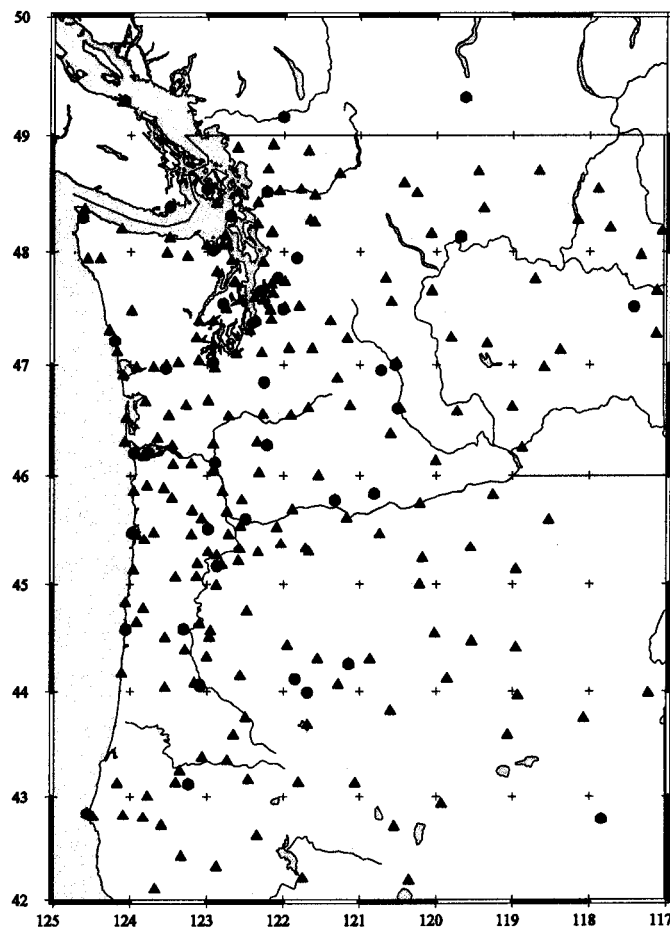


Figure 2.3. Campaign and permanent GPS sites processed in the Pacific Northwest for this study. Black triangles are campaign sites. Red circles are permanent sites

In campaign surveys, careful recording-keeping is required. First one needs any existing field logs for the particular site. Sometimes they are obtained from the USGS or as datasheets from the National Geodetic Survey (NGS). Even if equipped with a handheld GPS navigator, one can have

difficulty finding a site without a detailed description. Second, one must set up a tripod for the GPS antenna solidly; otherwise the tripod will not stay level over the course of the day. Sometimes bench marks are buried and it is necessary to dig out the mark. Although different GPS receivers have different setup procedures, one must always record site name, antenna type and serial number, receiver type and serial number, height of the antenna above the bench mark and time of occupation.

Our convention is to use universal time rather than local time on the log sheet. In general all antennas should be oriented consistently toward true north. Since lowering the elevation cutoff angle reduces the daily scatter in the computed vertical position, Bar-Sever et al. (1998) suggested using 7° cutoff to estimate horizontal gradients of tropospheric path delay, so our surveys used a 7° cutoff.

§2.6 GPS data Processing

After GPS data have been collected, the next step is to process them to estimate absolute site positions versus time and, thus, get a “time-series” (position vs. time) and velocity for each site. The software we used is called GIPSY/OASIS – II, an analysis package developed by the Jet Propulsion Laboratory (JPL) (Webb and Zumberge, 1997) in Los Angeles, CA. GIPSY and OASIS stand for GPS Inferred Positioning SYstem which is specifically for GPS data analysis, and Orbit Analysis and SIMulation Software which incorporates covariance analysis for earth orbiting and deep space missions (Gregorius, 1996). The combination, often simply called GIPSY, uses undifferenced GPS observables to reduce phase and pseudo-range data simultaneously. Besides GIPSY there are other types of software to do this kind of analysis (e.g. BERNESE, GAMIT) that use double-difference techniques. The advantages and disadvantages of using undifferenced or double-differenced methods can be found in Blewitt (1993).

Generally, we divide the GPS data processing procedure into three parts: pre-processing, processing and post-processing. The output of the first two steps is a free-network “stacov” file or a “stacov” file in a common coordinate reference frame (e.g. the international terrestrial reference

frame, ITRF2002). The stacov file (Table 2.2) contains the date and number of estimated parameters, estimated coordinates X, Y, Z for each site in meters in an earth-centered, earth-fixed cartesian reference frame with uncertainties for each parameter, and finally their covariances. The vertical antenna phase center offset information (distance from the antenna to the surveyed benchmark) is appended at the end.

Table 2.2 Free-Network Stacov File Format

3 PARAMETERS ON 96AUG09.					
1	ALBH STA X	-0.234133263072189E+07	+-	0.229455313322056E-02	
2	ALBH STA Y	-0.353904972658988E+07	+-	0.265265774469544E-02	
3	ALBH STA Z	0.474579125157239E+07	+-	0.298344657077350E-02	
2	1	0.470096706190010E+00			
3	1	-0.625991793650735E+00			
3	2	-0.792608797153501E+00			
	ALBH ANTENNA LC	0.1822	0.0000	0.0000	!up north east (m)
	! Reference frame: free-network				

After “stacov” files for each site-occupation have been created, we merge them into a combined stacov file in which coordinates are transformed into the reference frame desired. This work is in the post-processing stage of the analysis.

§2.6.1 Pre-Processing

After coming back from a campaign survey, we check station log sheets and put information about sites, antennas, and survey times into a Microsoft ACCESS database containing the occupation history of all surveyed sites. One must be very careful to determine correct survey times and antenna information, particularly the height measurements. Raw binary GPS data downloaded from receivers are converted to standard ASCII RINEX (Receiver INdependent EXchange) format files (Gurtner et al., 1989) using a program developed by UNAVCO called “TEQC”. If necessary, TEQC can segment very long data into small sections of no more than 24 hours duration which is required for processing using GIPSY software. TEQC also is used to check initial data quality and identify problems in the data, such as time gaps and an abnormally high number of cycle slips. For other TEQC capabilities, check the UNAVCO website.

Commonly, additional GPS data are available for a particular day from the National Geodetic Survey (NGS), Continuously Operating Reference Stations (CORS) operated by other agencies.

These agencies include the USGS, Canadian WCDA, and the IGS. If the data were stored on a CD, one must check whether the days you want are on the CD and read any included instruction very carefully to know how the CD was made. Sometimes, some DOY (Day Of the Year) days and survey periods in the instructions are not consistent with those in the data directory. In this case, one must read the RINEX file header to get the right DOY and recording periods. Sometimes, some sites have several survey sections on the same DOY day with each section using a different antenna. One must be careful to find the right antenna type and antenna height, and determine by what method the height was measured because antenna height errors are the most common problem in GPS processing.

Table 2.3 Format of site names in file "sta_ip"

AIS1	0	AIS1	
ALBH	1	ALBH	Vancouver Island, BC, Canada
ALGO	1	ALGO	ARO 883160
ANC1	0	ANC1	
APSA	1	APSA	Chehalis Airport, WA, USA
APSA	1	STAA	(STA.A_AP_1956_USCG) NGS PID: SC0205 Chehalis Airport, WA, USA
AREQ	1	ARE1	Arequipa, Peru (JPL)
ARLI	1	ARLI	Arlington Airport, WA, USA (CVO site) (UW Camp96)
ARLO	1	ARLO	Arlington Airport, WA, USA (NGS site) (UW Camp96)
ASTO	0	ASTO	
AVIA	1	AVI2	Aviation 2, NGS NOAA, Seattle, WA, USA
AVIA	1	AVIA	Aviation 2, NOAA, Seattle, WA, USA
AVIA	1	AVA2	Aviation 2, NOAA, Seattle, WA, USA, Ronnie added
B197	0	B174	(alternate name for Bremerton Air ie mistake)
B197	1	B197	B1974, Bremerton Airport, WA, USA (UW Camp96)

When processing GPS data, GIPSY requires all site and survey information be stored in the following files: sta_ip, sta_pos, sta_svec, pcenter, and antenna.truth which are kept in directories /goa/sta_info or /gpsstor/GIPSY_OTHER/ STA_INFO_UW/. They are all ASCII files so that they may be easily viewed and modified by a person using an editor. In file "sta_ip" the first column is the site name by which we normally refer to a station. The third column is reserved for an alias-name, a site name other people may use for the same station. The fourth and later columns are for any comments of what the site name represents (Table 2.3). Some sites may have several alias-names. In this case, all other names will be "converted" to the unique name in the first column. The "sta_pos" file contains the date a site was established and its X, Y, Z

coordinates. It also indicates if a site is permanent or temporary (Table 2.4). Usually this file doesn't require multiple time entries for a particular site even if it is occupied more than once every few years. Once a site's information is input, there is usually no need to change it.

Table 2.4 Format of file "sta_pos"

NEAH	1994	10	04	00:00:00.00	9999999.00	-2415625.5876	-3498394.0244	4739316.8471	0.0000000e+00	0.0000000e+00	0.0000000e+00	Sun	Mar	10	16:35:39	PST	1994	gia	stacov2sta_pos 2.4 /stor/GIPSY/GIA/ANAL/289/RUN3/results/95oct16.stacov	
CHEE	1994	10	04	00:00:00.00	9999999.00	-2415625.5876	-3498394.0244	4739316.8471	0.0000000e+00	0.0000000e+00	0.0000000e+00	Sun	Mar	10	16:35:39	PST	1994	gia	stacov2sta_pos 2.4 /stor/GIPSY/GIA/ANAL/289/RUN3/results/95oct16.stacov	
GWEN	1994	09	30	00:00:00.00	9999999.00		-2316901.0622	-3806506.8622	4548956.5305	0.0000000e+00	0.0000000e+00	0.0000000e+00	Mon	Nov	10	17:04:57	PST	1994	gia	stacov2sta_pos 2.4 /data10/GIPSY/PANGA_tseries/Run_itr93/final.stacov
POUL	1994	08	15	00:00:00.00	9999999.00	-2317551.9532	-3619717.7104	4696780.0663	0.0000000e+00	0.0000000e+00	0.0000000e+00	Thu	Oct	1	15:19:57	PDT	1998	gia	stacov2sta_pos 3.1 /gipsyhome/Gia/Camps/Camp94/227_xt-gipsy/bias_free.stacov	

For each entry, the first four upper letters indicate the name of one site. The following time is the site setup time. "9999999.00" means it's a permanent site. The following three values are X,Y,Z coordinates in the earth-centered Cartesian reference frame. "0.0000000e+00 0.0000000e+00 0.0000000e+00" are site velocities in meters/year. The rest parts are comments. "Sun Mar 10 16:35:39 PST 1994" indicates when the site position information was input to the file. The rest indicates how the information was input.

Another important file is "sta_svec" which needs updating whenever new data at a site will be processed. Each survey at a site should have an entry in this file which means a site may have multiple entries if it is surveyed many times over the years. Each entry consists of: a "to" station identifier and a "from" station identifier (Usually both are the same); an epoch of the site vector (year, month, day, hours, minutes and seconds); a duration (seconds), indicating the length of time the site vector is valid from the epoch time; an antenna type, corresponding to one of the antenna types in the pcenter file; an station site vector; an antenna height; a site vector coordinate system flag, where c indicates Cartesian coordinates (XYZ) and l indicates local east-north-up coordinates (ENU); a date the site vector was issued; and a comment about how this record was input (Table 2.5).

Antenna information is stored in the "pcenter" file which normally is not modified unless there is a new type of antenna added to the database. Generally three or more lines are used for each type

Table 2.5 Example of “sta_svec” file

MESA	MESA	1998	11	19	00:00:00.00	86400.00	TRIM_CGP	0.0000	0.0000
0.0000	2.0000	1	2001	09	04	Add from Access database			
B317	B317	1998	11	19	00:00:00.00	86400.00	TRIM_CGP	0.0000	0.0000
0.0000	2.0000	1	2001	09	04	Add from Access database			
FALL	FALL	1998	11	17	00:00:00.00	86400.00	TRIM_CGP	0.0000	0.0000
0.0000	2.0000	1	2001	09	04	Add from Access database			
VANC	VANC	1998	10	30	00:00:00.00	86400.00	TRIM_MIC	0.0000	0.0000
0.0000	1.5720	1	2001	09	04	Add from Access database			
CHAS	CHAS	1998	10	29	00:00:00.00	86400.00	TRIM_CGP	0.0000	0.0000
0.0000	2.0000	1	2001	09	04	Add from Access database			
HELE	HELE	1998	10	29	00:00:00.00	86400.00	TRIM_CGP	0.0000	0.0000
0.0000	2.0000	1	2001	09	04	Add from Access database			
VANC	VANC	1998	10	29	00:00:00.00	86400.00	TRIM_MIC	0.0000	0.0000
0.0000	1.9680	1	2001	09	04	Add from Access database			
VANC	VANC	1998	10	28	00:00:00.00	86400.00	TRIM_MIC	0.0000	0.0000
0.0000	1.5100	1	2001	09	04	Add from Access database			

of antenna. Each line gives the offset of the electrical phase center of the antenna from a standard measurement point on the antenna (usually the center of the base of the antenna) for various types of observables: L₁, L₂, LC, etc. Each line has the following fields: the antenna type, the phase center type, the phase center offsets in meters (east, north, and up), and a comment. The record format is (a9, 1x, a2, 3f9.4) (Table 2.6)

“Antenna_truth” is another important file that can be used to later correct a “stacov” file for errors caused by initial processing of the data with an incorrect antenna height. The post-processing program, heightfix, utilizes this file (Table 2.7). If the right antenna height is used in initial processing, this step is not necessary.

At the UW there are several ways to change these sta_info files. Two of them utilize the ACCESS database once the information there is absolutely correct. Before changing these files, one should first backup sta_info files in case something goes wrong and you need to restore them. One

method uses an ACCESS query which has columns (StationCode, DOY, StartDate, HI, Antenna_Type, HI_Type) to export a text file with autostart, save formatted options. Let's call the

Table 2.6 PCENTER format

ROGUE_T	L1	0.0000	0.0000	0.1100 TurboRogue
ROGUE_T	L2	0.0000	0.0000	0.1280 DORNE MARGOLIN T
ROGUE_T	LC	0.0000	0.0000	0.0822 Entered by Gia Khazaradze
ROGUE_T	P1	0.0000	0.0000	0.1100 10/28/1996 from IGS-01
ROGUE_T	P2	0.0000	0.0000	0.1280
ROGUE_T	PC	0.0000	0.0000	0.0822
ROGUE_T	C2	0.0000	0.0000	0.1280
ROGUE_T	DR	0.0000	0.0000	0.0000
ROGUE_T	R2	0.0000	0.0000	0.0000
ROGUE_R	L1	0.0000	0.0000	0.0780 DORNE MARGOLIN R
ROGUE_R	L2	0.0000	0.0000	0.0960 JPL design
ROGUE_R	LC	0.0000	0.0000	0.0502 Entered by Gia Khazaradze

file "campaign.txt". Remember DOY should be sorted in descending order so that the most recent times are first, consistent with the convention Gipsy uses for "sta_svec". Then use a text file editor to edit the above text file. Delete those stations you don't want due to lack of data and upload the text file into a machine where you process the data using GIPSY. Run "/u1/gps/bin/add_sta_info campaign.txt (the above exported text file)" to change sta_info files.

Another way to update the sta_info files is to use another query called "sta_info_export" including | StaCode | StartDate | StartTime | EndDate | EndTime | HI | AntTypeCode | HI_type | format for each line to export a text file with autostart and save formatted options. Let's call this exported text file "sta_info.txt", upload it to your machine and run "addsvect sta_info.txt". "addsvect" will split any record in the ACCESS database with more than 24 hours recording data

Table 2.7 Example of Antenna_truth file

MESA	98NOV19	2.080	2.000	?.????	??.????	?.????
B317	98NOV19	2.080	2.000	?.????	??.????	?.????
FALL	98NOV17	2.080	2.000	?.????	??.????	?.????
ANC	98OCT30	1.652	1.572	?.????	??.????	?.????
CHAS	98OCT29	2.080	2.000	?.????	??.????	?.????
HELE	98OCT29	2.080	2.000	?.????	??.????	?.????
SiteName	Date	Height ^①	a ^②	b ^③	c ^④	d ^⑤

^①Height == the height from the monument to the phase center. Height = c+d.

^②a == height from 1st to 2nd reference point (thickness of ant).

^③b == height to 1st reference point (in log, e.g. bottom chokering).

^④c == antenna reference point to phase center (e.g. TOC to PC).

^⑤d == height to 2nd antenna reference point (e.g. top of chokering). d = a+b

Columns a-d are for human consumption, and are not read by heightfix.

into several records beginning at time 00:00:00. Each record will account for no more than 24 hours of data, i.e., from 00:00:00 to 23:59:30. If the actual recording extends to the next day by a small amount (less than 2 hours), there is no need to split it. Any day with less than 2 hours data should be discarded. This is because the predicted orbits from the previous day will reasonably predict the satellite positions for a short time into the next day. "addsvec" will update files sta_svec, antenna.truth, and sta_id. For each entry in the sta_svec file, "addsvec" will input actual start-time of recording and duration in seconds instead of just using 0:0:0 starting time and 86400 second duration. Sometimes the start-time and end-time are not accurately known, it's better to insert a starting time in "sta_svec" that's 10 minutes earlier than the actual time in the ACCESS database and a duration in "sta_svec" that is 20 minutes longer than that calculated from ACCESS database to insure all data get processed. After running "addsvec", you will get the three files sta_ip, sta_pos, sta_svec. After making sure they are correct, move them into /gpsstor/GIPSY_OTHER/STA_INFO_UW/. You can over-write the three files if you choose the y option when running "addsvec sta_info.txt y". This option also allows script "addsvec" to backup the old sta_info files before updating. Station coordinates in your sta_pos file can be checked by using the website <http://www.ngs.noaa.gov/datasheet.html> and http://www.ngs.noaa.gov/FORMS/ds_desig.html. If the coordinates are not very close, update them in sta_pos. Finally, one should

check time-pole files before processing. These files contain information about polar motion and planetary ephemeris. For updating these files, please read /u1/gps/DOCUMENTS/PROCESSING/time-pole.notes carefully.

After sta_info files are ready, one needs to arrange RINEX data files before processing. First sort all your RINEX data according to their DOY. Use DOY to create separate directories. Put all data surveyed on the same DOY in the same year into the same directory. After this step, upload all your data into a working directory.

Table 2.8 JPL final products required for PPP analysis

File Name	Description
YYYY-MM-DD.eci_nf.Z ^①	Fiducial-free precise satellite orbits
YYYY-MM-DD.tpeo_nf.nml.Z	Time, polar motion and earth orientation information
YYYY-MM-DD.shad.Z	List of satellites in passing through the earth's shadow
YYYY-MM-DD_nf.tdpc.Z	Time dependent parameter file (TDP)

^① YYYY: year; MM: month; DD: day. .Z needs uncompression

§2.6.2 Processing

The strategy used here to process GPS data is Precise Point Positioning (PPP). The procedure is used to estimate the coordinates of a single station. Via a series of scripts, the procedure automatically downloads fixed orbits, satellite clock parameters, TPEO estimates (about Time, polar motion and earth orientation information), and satellite eclipse information from JPL, derived from a global fiducial network of stations (Table 2.8). The idea behind PPP is to estimate the orbits and satellite clocks once using a high-quality global fiducial - free network, and then to use all that information to estimate the station parameters of any site in the world on any specific day with high confidence. The four day-specific files can be downloaded by using anonymous ftp from sideshow.jpl.nasa.gov seven to ten days after the data are recorded. In each run, the PPP strategy only processes one site at a time which takes a couple of minutes on a SUN Ultra 10. The time needed to process a whole network of stations increases linearly, not geometrically, with the number of stations. This means that PPP can be used to efficiently process hundreds of sites. This makes PPP a robust tool, with an estimation accuracy that is comparable to that of global network solutions. However, PPP still has some shortcomings, such as, inability to account for correlations

between sites, and errors associated with imperfectly known satellite orbits.

When processing GPS data, two kinds of JPL products can be used. One is the final fiducial-free products of table 2.8 which are available about 10 days after data are recorded. Another one is rapid service products (Table 2.9) which are available within 24 hours after data recording. Compared to the final products, rapid service products give slightly less accurate results but are still very good for real-time applications. Table 2.9 lists all rapid products for rapid service. Note that the TPNML file doesn't have the \$earth_orientation group and there is no complete TDP file.

Table 2.9 JPL rapid products used in PPP

File Name	Description
YYYY-MM-DD.eci_nf.Z ^①	Fiducial-free precise satellite orbits
YYYY-MM-DD.TPNML_nf.Z	Time, polar motion and earth orientation information
YYYY-MM-DD.shadow_events.Z	List of satellites in passing through the earth's shadow
YYYY-MM-DD.gps_clocks_nf.Z	GPS clock file
YYYY-MM-DD.yaw_rates.Z ^②	Need be converted to TDP format

^① YYYY: year; MM: month; DD: day. .Z needs uncompression

^② Need be converted to TDP format and merged with the clock information by using script yaw_rates2tdp

After getting all "stacov" files for individual sites, PPP finally merges them into a combined stacov file and downloads an "x-file" to transform the daily solution into a specific reference frame, such as ITRF. For detailed information about what scripts PPP calls and the PPP procedure, please refer to Thierry Gregorius, 1996 and Webb & Zumberge, 1997.

A final optional step is to perform ambiguity resolution which generally gives a factor of 1.5 to 2 higher accuracy in site positions. There are four approaches to resolve ambiguities: double-differencing (refer to section §2.4), wide-laning, narrow-laning, sequential bias-fixing and sequential bias-optimising. For detail about these four methods and their mathematics, refer to Gregorius, 1996. Ambiguity resolution is implemented by program ambigon2 in GIPSY starting from undifferenced estimates (smcov.nio file). It sequentially executes programs smapper, smcov2oafilter, ambigon and edtpnt2. In order to resolve ambiguities, an ambiguity-free solution with a "wash template" file and a namelist file generated by amb_nml command must exist. The result is a final stacov file called YYMMMDD_fix.ITRF97.stacov. Here YY is the last two digits of the year, MMM is the first three letters of the month, DD is the day, and ITRF97 is the identification of the particular reference frame. You can run PPP and ambiguity resolution

separately or run them sequentially but automatically using the script called "point_amb". Currently, the maximum number of sites ambigon2 can run is less than 40. The following in bulleted text are the steps to get through all the processes:

- After sta_info files are ready and all data are uploaded, choose one day to process. Enter the DOY directory associated with that day and use ftp scripts in ~gps/bin to download other continuous data you don't have. Then unzip them using gunzip or z2rnz. Use the up2low script to convert all upper-case file names into names with lower-case letters. Since the number of sites processed in each run is limited, you should include some sites to create a good geometrical station distribution from available continuous sites. For example, choose sites uniformly located in a circle or a square. Otherwise, gipsy program ambigon2 will fail.
- Go into the directory above the DOY directory and runlow "startp" script by "runlow startp DOY >& log &". After "startp" is done, check the log file for each site to find if its processing has run correctly. The log file will exceed 1kbyte if processing is successful. If it is less than 1kbyte, the processing has probably failed. At the point_rnx level, there should be no problem. If some errors pop up, check time-pole files first and make sure you have the latest version. Most problems arise from incorrect or missing sites information in sta_info files or antenna information in "pcenter". If station information is missing, add it manually. Generally, "startp" will check if each site is in the "sta_pos" file. If it is not there, then "startp" will use the RINEX header to add it. If the position of a station in the "sta_pos" file is far from the actual position, for example, 100 meters, the final result will not be good and generate a bad point in the time-series later. "Startp" calls "point_amb" which I changed a little bit since it couldn't locate "x-file". You can check "point_amb" source file.
- When the processing is done, one must check the ambiguity results. If there are too many sites to process (limit is 37), you may only obtain "free.stacov" and "free.ITRF97.stacov" files for each site, and not the ambiguity outcomes. The program may dump at the last step of processing and create a "core" file. In this case, delete all files except the original RINEX files, reduce the number of RINEX files, and repeat the above steps.
- Sometimes, the processing stops without any apparent reasons. In this case, delete all other files except the RINEX files and re-arrange sites so that they are in a good geometry and do the processing again.

§2.6.3 Post processing

After all daily position solutions with ambiguity resolution are available, the next step is to produce “time series” and estimate the velocity of each individual station. Backup all the files including original RINEX files, log files, stacov files by compressing and downloading them to a PC, burning them to CDROM. Then move all non-fiducial ambiguity “stacov” files into a directory. If some days have multiple files, rename them by appending extra letters and keep the date information in the filename. Since errors in the antenna phase center vertical offset may exist in the initial GPS processing, script “heightfix” is used to correct them. Some “stacov” files might be in different International Terrestrial Reference Frames (ITRF), if so, download the appropriate “x-file” from JPL and use script “apply” to convert all non-fiducial ambiguity stacov files from one ITRF system to another. You can also use script “/u1/gps/bin/ConvertITRF” since it calls “apply”. For example, if want to convert all ambiguity stacov files to ITRF00, just run “ConvertITRF fix 00”. The transformation requires an x-file from JPL and JPL computes it by using continuous GPS sites around the world. The same sites are not always used in every computation which may introduce noise in the fiducial solution.

The JPL x-file computation doesn’t use many local stations so that the local factors affecting daily solutions are not considered. One solution is to compute a regional x-file using local continuous GPS stations. A localized time series has smaller scatter for all three components, x, y, z, and produce a better velocity determination (Dan Johnson, Personal communication). After all stacov files are in a local reference frame, the next thing to do is to check each stacov file to see if some sites have very big uncertainties by using “grep -i e+02 stacov_file”, then delete the lines with big errors from the stacov file. A Perl script called “removebadsite” can do this job automatically.

To extract positions of each site from all the stacov files one may use script “separatestations” and execute “separatestations [option]”. The option determines whether “heightfix” is run or not. If the option is y or Y, “heightfix” is run for each stacov file. Then the script reads sitename from “stacov” files and checks if the first line in stacov files has some date problem. For example, sometimes the first line contains 0AUG01 instead of 00AUG01, the script corrects it. The script

also checks if the site is in “sta_id”. If not, it prints a message saying “site is not valid”. “separatestations” will also change any station name aliases to conventional names. Finally the script generates subdirectories whose names are the same as station names. “separatestations” calls “statistics” with the -gd option to get absolute coordinates for each individual station for one particular day. These coordinates are saved in three files, called “sitename”.lat, “sitename”.lon, “sitename”.rad. “separatestations” uses the first point in each file as a reference, saves the three reference coordinates in three files called “latreference”, “lonreference” and “radreference”, and writes “sitename”.lat, “sitename”.lon, “sitename”.rad the site latitude, longitude and radius minus the reference values. The last step is to check all three files and delete abnormal values for each site manually. The reason I didn’t use “stamrg” to combine all “stacov” files when extracting stations is because it takes a very long time to process the data and it has a 999 days limit. Sometimes it will also fail due to large CHI^2/DOF (DOF means Degrees Of Freedom).

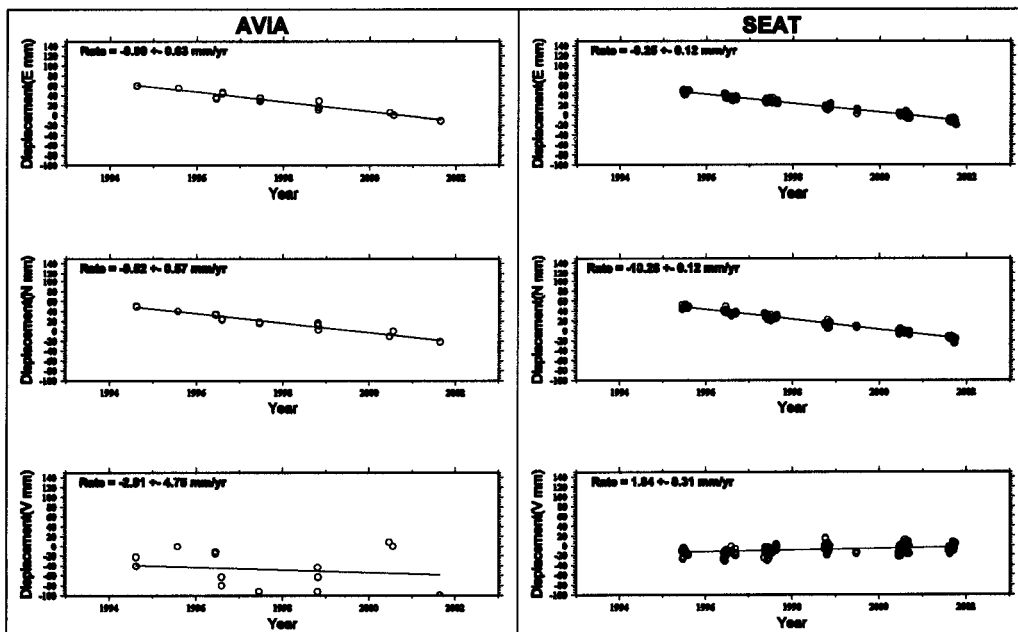


Figure 2.4 Time series for a GPS campaign station AVIA and a permanent station SEAT in the ITRF2000 reference frame generated by a Perl script “times”

A Perl script “times” is used to draw x, y, z time series and estimate station velocity and uncertainty using a least squares approach and GMT software. It automatically detects bad points and deletes those whose deviations are three times bigger than the computed standard deviation. Here x, y, z components mean east, north, and up respectively. The script generates a graph in

postscript format for each component as shown in figure 2.4 and outputs four files. File "vxyz" contains three components of velocities: v_x , v_y and v_z . File "vxy" contains two components of velocities: v_x and v_y . File "vframe" contains coordinates of each site. File "vname" contains sitenames with additional font settings used to draw sitenames on a postscript file.

All site velocities were estimated in the reference frame ITRF2000. All velocity vectors in figure 2.5 are oriented toward the southwest because the velocities are computed relative to the ITRF2000 reference frame, not relative to the stable part of the North America plate (NA). To transform the velocities from ITRF (ITRF2000) into a fixed North America reference frame we

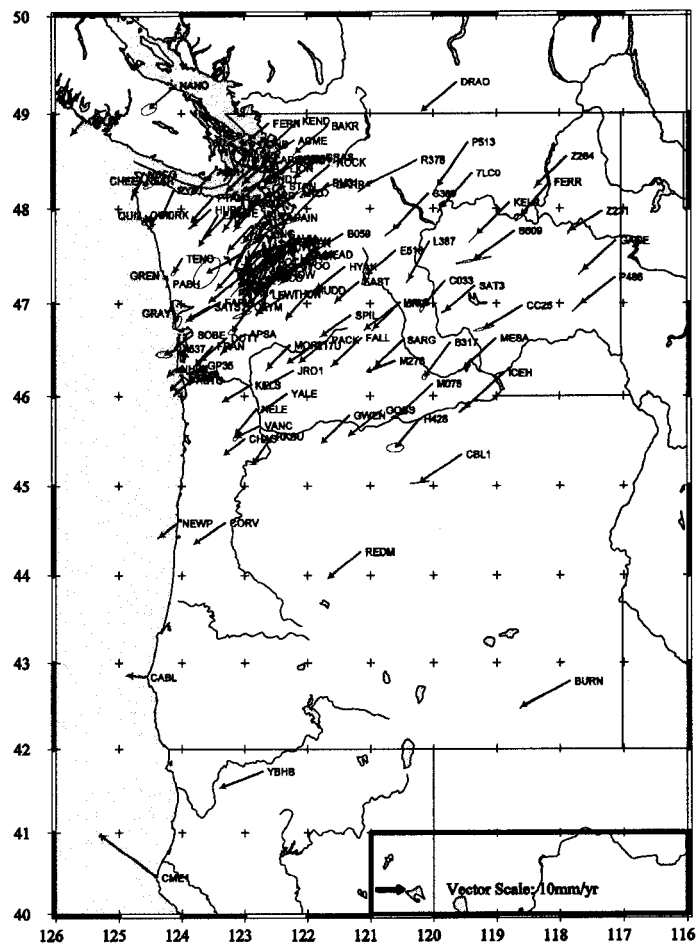


Figure 2.5 Site velocities in ITRF2000

subtract a no-net-rotation (NNR) model of current plate motions (Altamimi, Z, et al. 2002). The

following estimated NNR absolute rotation pole of the North America (NA) plate was used to estimate NA velocity for each GPS site (Table 2.10).

Table 2.10 ITRF2000 NNR Absolute Rotation Pole for the North America Plate

Plate Name	Latitude ($^{\circ}$ N)	Longitude ($^{\circ}$ E)	Ω ($^{\circ}$ /m.y. clockwise)
North America	-5.036 ± 1.142	-83.144 ± 1.945	0.194 ± 0.003

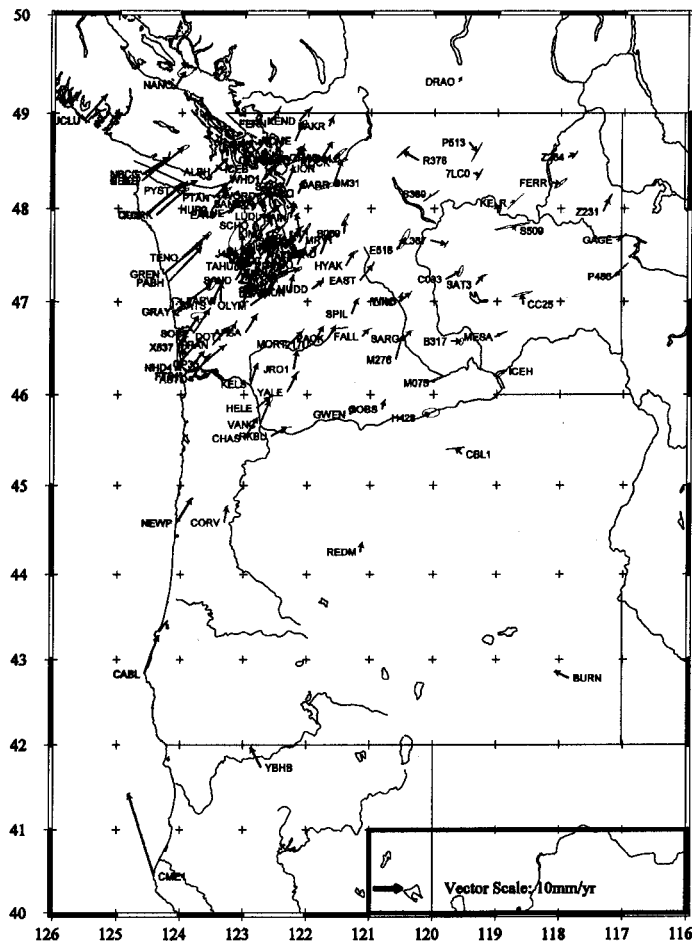


Figure 2.6 Deformation velocities relative to the North America continent after removing the motion of NA in the ITRF2000 reference frame. Sites in this figure include both campaign and permanent stations. The GPS data in the figure span from 1994 to 2001.

After this last transformation, all site velocities are expressed relative to the North America (NA) plate (Figure 2.6). Most sites along the Coast Range move toward NA in a direction almost perpendicular to the CSZ trench. The deformation velocities decay rapidly from the Coast Range to the backarc and vary from south to north in both magnitude and direction. For example, site

NEAH (Olympic Peninsula, Washington) moves 13mm/yr N65°E, WDH1 (Whidbey Island, WA) moves 7mm/yr, and site 7CL0 moves 2mm/yr. Note that stations far from the trench do not have zero velocities. Even station DRAO (Penticton, Canada) exhibits a small motion relative to stable NA, consistent with previous observations (Argus and Heflin, 1995; Argus and Gordon, 1996).

Most campaign sites that we have occupied are in western Washington. Some campaign sites are in eastern Washington. In Oregon, we do not have as many campaign occupations as in Washington. So I mainly processed GPS data from the sites in Washington (Figure 2.6).

Generally, we survey campaign GPS sites every few years and we process the current data and re-process the previous data in the most recent ITRF reference frame. In chapter 3, I will discuss results from data in Washington from 1994 to 2000 while in chapter four I will use an expanded data set from 1994 to 2001 in the Pacific Northwest, which was completely reprocessed using both Gipsy and GAMIT.

Chapter 3: Model of Cascadia Subduction Zone

§3.1 Introduction

In the previous chapter we described how site velocities in Washington are obtained from GPS data. In this chapter, we will investigate tectonic mechanisms that can cause these motions. The biggest earthquake in the history of the Pacific Northwest was caused by a rupture of the Cascadia Subduction Zone (CSZ) in 1700 AD (*Atwater et al.*, 1995; *Satake et al.*, 1996; *Clague*, 1997, 1999). Obviously the CSZ is a major element in the tectonics of the Pacific Northwest. Previous studies (*Wells et al.*, 1998; *McCaffrey et al.*, 2000; *Savage et al.*, 2000) show that western Oregon rotates clockwise as a rigid block. Here we explore the following questions: Does rigid block rotation exist in Washington? Are there any other mechanisms contributing to the observed crustal deformation? How important is each mechanism? What is the geometry of CSZ?

In this chapter, I will use an inverse three-dimensional model based on elastic dislocation theory and inverse theory to investigate the contribution of subduction to present-day observations of GPS data. We will see that in addition to subduction, we need to include both rigid block rotation and N-S compression (unrelated to subduction) in order to match GPS observations.

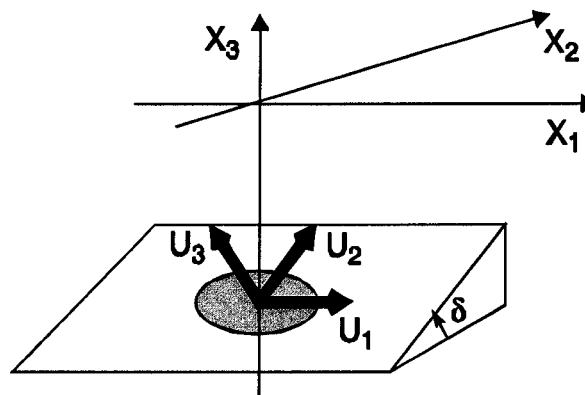


Figure 3.1: Point source representation of a fault plane. X_1 is oriented parallel to the strike of the fault, X_2 perpendicular to X_1 . The media where $X_3 \ll 0$ represents an elastic half-space. δ is the fault dip angle. U_1 , U_2 , and U_3 are the vectors representing the movement of the hanging wall relative to the foot wall for strike-slip, dip-slip, and tensile components of elementary dislocations on the fault surface (*Okada*, 1985).

§3.2 Theory of elastic dislocation modeling

Steketee (1958a) first applied elastic dislocation theory to surface displacement modeling. He showed that displacement field $u_j(x_1, x_2, x_3)$ caused by a dislocation $\Delta u_j(\xi_1, \xi_2, \xi_3)$ across a surface S in a uniform elastic half-space can be given by the following formula:

$$u_i = \frac{1}{F} \iint_S \Delta u_j \left[\lambda \delta_{jk} \frac{\partial u_i^n}{\partial \xi_n} + \mu \left(\frac{\partial u_i^j}{\partial \xi_k} + \frac{\partial u_i^k}{\partial \xi_j} \right) \right] v_k dS \quad (3.1)$$

Here, the coordinate system is shown in Figure 3.1

u_i : Displacement

F : Magnitude of a point source at (ξ_1, ξ_2, ξ_3)

Δu_j : Dislocation

λ, μ : Lamé constants

δ_{jk} : a Kronecker delta function

u_i^j : The i th component of displacement at (x_1, x_2, x_3) point due to the j th component of a point force with a magnitude F at (ξ_1, ξ_2, ξ_3) .

v_k : The outward normal unit vector to surface S.

dS : Surface element

Okada (1985) used *Volterra's* formula (Equation 3.1) to derive a complete suite of analytic expressions for surface displacements, strains and tilts for shear and tensile faults in three dimensions, based on previous work about elastic dislocation modeling. In 1992, he furthered his work and got compact and systematic expressions for internal displacements, strains due to shear and tensile faults in a half-space for both point and finite rectangular sources (*Okada*, 1992). These expressions are very powerful tools to do observational and theoretical analysis of static field changes due to earthquakes and volcanoes. Since then, numerous studies have used his formulas to do surface deformation modeling (*e.g.*, *Fluck* 1997) and strain accumulation (*e.g.* *Murray et al.*, 1994, 1996; *Verdonck*, 1995).

§3.3 Two dimensional modeling of surface deformation

Based on elastic dislocation theory, *Freund and Barnett* (1976) developed a two-dimensional model (Figure 3.3) to calculate the crustal surface displacement $u_x(x,0), u_y(x,0)$ and the slip plane shear stress distribution $\tau(\xi)$ assuming a net Burger's vector between neighboring points s and $s+ds$ of $\delta'(s)ds$.

$$u_\beta(x,0) = \int_a^{a+l} U_\beta(x,s)\delta'(s)ds \quad (3.2)$$

$$\tau(\xi) = \int_a^{a+l} T(\xi,s)\delta'(s)ds \quad (3.3)$$

where,

$$U_x(x,s) = \frac{s \sin \alpha (s - x \cos \alpha)}{\pi(x^2 + s^2 - 2xs \cos \alpha)} + \cos \alpha \tan^{-1} \left(\frac{x - s \cos \alpha}{s \sin \alpha} \right) \quad (3.4)$$

$$U_y(x,s) = \frac{xs \sin^2 \alpha}{\pi(x^2 + s^2 - 2xs \cos \alpha)} + \sin \alpha \tan^{-1} \left(\frac{x - s \cos \alpha}{s \sin \alpha} \right) \quad (3.5)$$

and $\beta = x$ or y for arbitrary relative slip $\delta(s)$. The constraint condition is $\delta'(a)=0$ and $\delta'(a+l)=0$. For other parameters, please refer to figure 3.2. $T(\xi,s)$ is not discussed further because we are concerned with surface deformation.

After this two dimensional model was proposed, *Savage* (1981) used it to model contemporary crustal deformation along the Cascadia subduction zone. In 1983, *Savage* refined his previous model by introducing a no-relative-slip "locking" zone between the subducting plate and over-riding plate. This was achieved by superposing a *supplemental solution*, which imposes a backward motion on the main thrust zone at a rate of the relative transverse plate motion and a locked zone in the shallowed asthenosphere, onto *steady state* subduction, moving at a constant plate convergence rate (*Savage*, 1983) (Figure 3.2). Later in 1991, he added a transition zone in models of interseismic strain accumulation in order to match an extended set of GPS observations.

In models with a transition zone, the crustal deformation does not decay so quickly as one moves inland away from the subduction zone. Other researchers used modified 2-D elastic models to estimate the geometry of CSZ. (Hyndman and Wang, 1993, 1995; Dragert et al. 1994; Dragert and Hyndman, 1995).



Figure 3.2. Elastic dislocation model of strain accumulation for a subduction zone. Arrows are the directions of plate movement. Streak lines indicate the locked place. (Savage 1983)

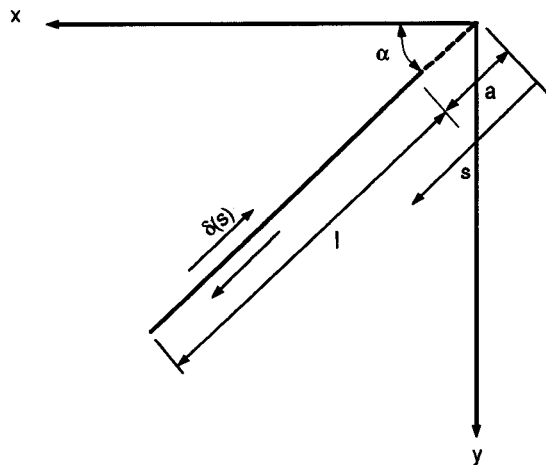


Figure 3.3 Geometry of the oblique dip-slip fault. The plane of deformation is the xy plane, the y direction is vertically downward. The proximity of the slipped region to the free surface is measured by a , s is the distance along the slip plane, α is the dip angle, l is the slip zone length, and $\delta(s)$ is the relative slip distribution. For detail, please refer to *L. B. Freund et al (1976)*.

§3.4 Three dimensional modeling

Although a modified two dimensional model can explain most observations of crustal deformation, *Verdonck (1995)* noticed shortcomings in previous studies and proposed a three dimensional model using a rectangular fault-plane source formula given by *Okada (1985)*. However, this 3D model could not account for the complex geometry of the Juan de Fuca plate. To improve this situation, *Flück (1996)* and *Flück et al. (1997)* developed a new three dimensional model based on *Okada's* point-source solution formula. This model divided the whole CSZ into a locked zone and a transition zone whose widths vary along strike. The variation in width was defined by sixteen profiles along the strike (Figure 3.4). The distance between profiles in the northern part of the CSZ is shorter than in the southern part to account for the

greater curvature in the north. The geometry of CSZ in this model is defined by depth contour lines at the top of the subducting oceanic crust derived from Benioff-Wadati seismicity, seismic reflection and refraction data, teleseismic receiver function analysis, and seismic tomography (e.g. *Crosson et al.*, 1987; *Owen et al.*, 1988; *Lapp et al.*, 1990; *Cassidy et al.*, 1993; *Cassidy*, 1995; *Trehu et al.*, 1995). The contours are well constrained except in central and southern Oregon (Figure 3.5). The other important factor in the model is the estimated velocity of the Juan de Fuca plate which has been discussed by other researchers (e.g., *Riddihough*, 1984; *DeMets et al.*, 1990). In *Flück's* model the plate moves at a constant velocity of 42mm/year and at an azimuth of 69 degrees. The widths of the locked and transition zones at both ends are narrower than they are near the Olympic Peninsula, where the plate dip angle is only 4° for the locked zone and 8° for the transition zone.

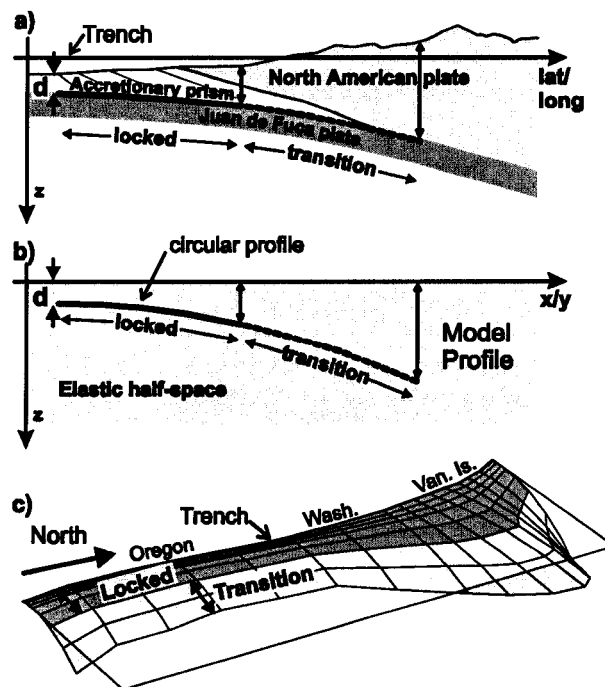


Figure 3.4 Flück's 3-D model. (a) and (b) are the 2-D view of the locked zone and transition zone. $Z \geq 0$ represents the elastic half space. (a) The real geometry. (b) Geometry approximation of the 3-D model profile. (c) 3-D view of the CSZ geometry in 3-D model. The view is from S-E in an elevation of 15°. This figure is taken from *Fluke* (1997)

§3.5 Inverse theory.

Inverse theory has been widely used in geophysics. Here I will briefly review its basics. Suppose

we are given a set of linearly independent elements $(x_1, x_2, x_3, \dots, x_N)$ in a Hilbert space H , and one unknown element $m \in H$ satisfying the following conditions:

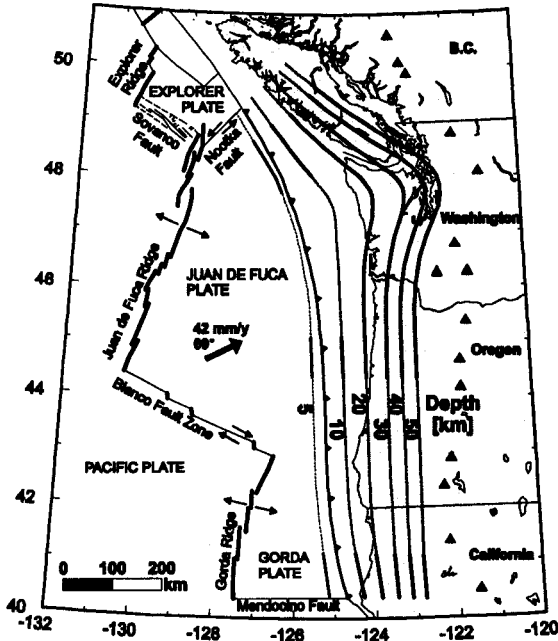


Figure 3.5. Contour lines for the depth of the Juan de Fuca plate in the Cascadia subduction zone. Solid lines indicate well-constrained depths. Dashed lines are extrapolated.

$$\begin{aligned}
 (x_1, m) &= d_1 \\
 (x_2, m) &= d_2 \\
 (x_3, m) &= d_3 \\
 &\vdots \\
 (x_N, m) &= d_N
 \end{aligned}
 \tag{3.6}$$

Here, (x, m) is an inner product which can be represented by the following:

$$(f, g) = \int_a^b f(t)g(t)dt
 \tag{3.7}$$

We call (3.6) the constraint equations. If we can express m as the sum,

$$m = \sum_{i=1}^K \alpha_i x_i
 \tag{3.8}$$

then we can write

$$\sum_{i=1}^K \alpha_i(x_j, x_i) = d_j \quad (3.9)$$

K is called the number of free parameters of m . Define $\boldsymbol{\alpha} = (\alpha_1, \alpha_2, \alpha_3, \dots, \alpha_K)$, $\mathbf{d} = (d_1, d_2, d_3, \dots, d_N)$, and matrix $\Gamma_{ij} = (x_i, x_j)$, then

$$\begin{aligned} \Gamma \boldsymbol{\alpha} &= \mathbf{d} \\ \boldsymbol{\alpha} &= \Gamma^{-1} \mathbf{d} \end{aligned} \quad (3.10)$$

Where $\boldsymbol{\alpha} \in \mathbb{R}^K$, $\mathbf{d} \in \mathbb{R}^N$, $\Gamma \in M(K \times N)$, \mathbb{R}^N is a real linear N -vector space. If the number of free parameters K is greater than N , the dimensions of H , the solution of m , $\boldsymbol{\alpha}$, is not uniquely determined.

Suppose we have a finite number of observation data d_j and an unknown model m that satisfies the data, we can write the solution of the forward problem as:

$$d_j = F_j[m], \quad j = 1, 2, \dots, N \quad (3.11)$$

where each function F_j relates the model $m \in H$ to the measurement $d_j \in \mathbb{R}$. If F_j is not only a linear but also a bounded function, we can write it in a general way by the Riesz Representation Theorem,

$$d_j = (x_j, m), \quad j = 1, 2, \dots, N \quad (3.12)$$

with $x_j \in H$. If the data are perfect, we can use the general way (3.6) to (3.10) to get a solution.

Assume that the ideal model is m , which, for some reasons we can't find exactly in reality. What we want to do is to find the closest model n . If let $n_0 + r = m$, then our task is to make the departure r from the ideal m as small as possible. Here $r, m, n_0 \in H$, and n_0 is the initial model.

Since, by equation (3.6),

$$(x_i, m) = d_i, \quad i = 1, 2, \dots, N \quad (3.13)$$

we get

$$\begin{aligned}(x_i, n_0 + r) &= d_i \\ (x_i, n_0) + (x_i, r) &= d_i\end{aligned}\tag{3.14}$$

Letting $(x_i, n_0) = d_0$, and $d_i - d_0 = \Delta$, and following equations, (3.6) to (3.10), we get

$$\mathbf{r} = \Gamma^{-1}\mathbf{\Delta}\tag{3.15}$$

then update the initial model n_0 by

$$n = n_0 + r\tag{3.16}$$

In order to get the smallest r , we need to repeat (3.14) to (3.16) until we think we have converged to a satisfactory model.

Although most problems in geophysics are non-linear, linear inverse theory remains a very important approximation. Let $z \in H$, a Hilbert space, and let $F: Y \subseteq H \rightarrow IR$ be a function on some domain Y in H . Then F is called a *Fréchet-differential* at the element z when we can find a D that for all Δ with $\|\Delta\| < \varepsilon$

$$F[z + \Delta] = F[z] + (D, \Delta) + R[\Delta]\tag{3.17}$$

and

$$R[\Delta]/\|\Delta\| \rightarrow 0 \text{ as } \|\Delta\| \rightarrow 0\tag{3.18}$$

Here $\Delta, D \in H$, R is another functional on H , and D is called a *Fréchet-derivative*.

We can also rewrite it as the following,

$$F[z + \Delta] = F[z] + \sum_{i=1}^N \Delta_i \frac{\partial F}{\partial z_i} + R\tag{3.19}$$

which also can be obtained from a *Taylor* series expansion. Consider a continuous differential function on E^N with an ordinary Euclidean norm and associated inner product. Then

$$(\mathbf{x}, \mathbf{y}) = \mathbf{x} \cdot \mathbf{y} = \sum_{i=1}^N x_i y_i\tag{3.20}$$

Compare (3.17) and (3.19), and use (3.20), the element D is equal to the ordinary gradient at z , namely $D = \nabla F$.

In general, if F is a bounded linear function on H , by the Riesz Representation Theorem:

$$F[z] = (x, z) \quad (3.21)$$

it follows that

$$F[z + \Delta] = (x, z + \Delta) = (x, z) + (x, \Delta) = F[z] + (x, \Delta) \quad (3.22)$$

Obviously the remainder R here is zero and the Fréchet derivative D is just x itself. Compare (3.17), (3.19) with (3.22), if we can make the remainder of non-linear problems, R , ignorable in (3.19), non-linear problems can be solved in a linear way from (3.6) to (3.16). To begin with the situation that we have N real data d_j already known; we are asked to find any model $m \in H$ that will fit the data exactly by a set of non-linear functionals F_j over an approximate Hilbert space H ,

$$d_j = F_j[m], \quad j = 1, 2, 3, \dots, N \quad (3.23)$$

We assume there is one solution m^* and one guessed model m_1 , and further assume each F_j is Fréchet-differentiable at m_1 , then

$$d_j = F_j[m^*] = F_j[m_1 + m^* - m_1] = F_j[m_1] + (D_j, m^* - m_1) + R_j \quad (3.24)$$

Suppose our guessed model m_1 is so accurate that R is ignorable, and we replace the true m^* with m_2 and let $\Delta = m_2 - m_1$, then we get a basis for an iterative scheme:

$$(D_j, \Delta) = d_j - F_j[m_1], \quad j = 1, 2, 3, \dots, N \quad (3.25)$$

Since m_1 and d_j are given, everything on the right is known. We can find the next approximation to the solution by $m_2 = m_1 + \Delta$. So the set of equations is exactly in the form of standard linear inverse problem for exact data. We can solve it using equations from (3.13) to (3.16). Here I will not discuss the existence and uniqueness of the solution to the non-linear problem. For this, see *Parker (1994)*.

§3.6 Previous studies of the Cascadia subduction zone

Savage (1981) is the first to model deformation of the CSZ. He created a 2D model based on elastic deformation theory in a half-space to model crustal deformation. In 1991 he included a transition zone in his model to refine his previous approach about strain accumulation and release at a subduction zone in 1983 after the observations from the Seattle and Peninsula trilateration networks were extended (*Savage*, 1983; *Savage et al.*, 1991). Today the combination of the locked zone and transition zone is called the seismogenic zone. Two dimensional elastic dislocation models with thermal constraints were used to estimate its width and location by *Hyndman and Wang* (1993), *Dragert et al.* (1994), *Dragert and Hyndman* (1995), *Hyndman and Wang* (1995), and *Oleskevich et al.* (1999) discussed thermal and geological controls to the updip and downdip rupture limits. At the updip end of the CSZ, the temperature is about 100°C, which is controlled mainly by the thickness of incoming sediment, the age of the incoming plate, and the heat flow that occurs there. The downdip limit is near a depth of 40km where the temperature reaches 350°C.

Based on the results from two-dimensional models, *Flück et al.* (1997) developed a general three dimensional elastic dislocation model to estimate the curved thrust fault geometry. The bend of the CSZ along the margin and the end effects of the subducting slab were included. In their best-fit model the average widths of the locked zone and the transition zone along the margin are both 60km at Vancouver Island and they vary smoothly from narrower and steeper in Oregon to wider and shallower in northern Washington. *Khazaradze et al.* (1999) used additional data from seven permanent GPS sites to get a “preferred” model in which the widths of the locked zone and transition zone in Washington are 100km and 130km, respectively. The increased width of the transition zone was required to explain the low rate at which the observed site velocities decay with distance away from trench.

In addition to elastic dislocation models, viscoelastic models have been used to determine the contemporary deformation of the Cascadia forearc. *Wang et al.* (1994) developed a two dimensional viscoelastic finite element model to better understand the dynamical changes of surface deformation. In this model, he used asthenospheric mantle with a viscosity of

$5 \times 10^{19} \text{ Pa s}$ and a mantle wedge between the subducted oceanic plate and overlying plate with a low viscosity of 10^{18} Pa s . Through various experiments, he concluded that the stick-slip zone is about 70km wide, close to the result from a simple elastic model. *Wang et al. (2001)* developed a three dimensional viscoelastic interseismic deformation model which used their previous seismogenic geometry of the Cascadia subduction zone. In this model, the deformation rate at inland sites first points seaward right after a megathrust earthquake, then gradually changes to the currently observed velocity 300 years after the earthquake. This model also better fits the rate at which the velocity decreases away from the trench.

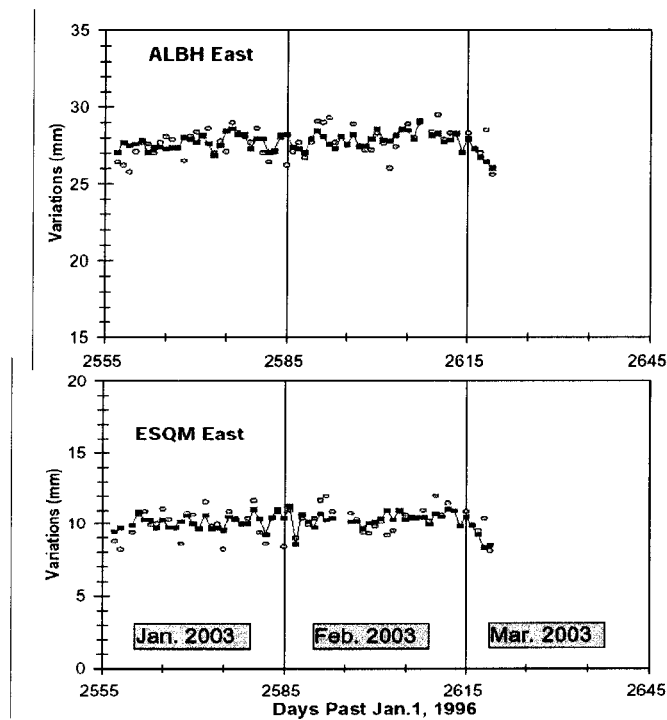


Figure 3.6. A silent slip event occurred on March 1, 2003. Daily relative positions in the east components. Circles give the raw output from the GPS analyses. Squares are regionally filtered results with network-wide (30 sites) correlated day-to-day variations removed. The change in trends over the last 4 days indicates westward motion.

When processing GPS data from permanent sites in British Columbia and Washington, *Dragert et al. (2001)* found that in the summer of 1999 a cluster of sites reversed temporarily their direction of motion without any accompanying seismicity. They interpreted the cause to be 2 centimeters of aseismic slip over a 50km x 300km area on the subducted interface downdip from the seismogenic zone. *Miller et al. (2002)* looked at changes in the lengths of seven baselines between Penticton, B.C. and other sites above the seismogenic zone and found additional evidence of multiple silent slip events. They estimated an average recurrence time for these

events of 1.2 ± 0.1 years since 1992. *Thatcher* (2001) also found silent slip on the Cascadia subduction interface. On March 7, 2003, Dragert announced a silent slip event that had begun on March 1 (Figure 3.6). These observations suggest that there is a silent slip zone downdip from the seismogenic zone.

§3.7 Model Construction

§3.7.1 Data resources

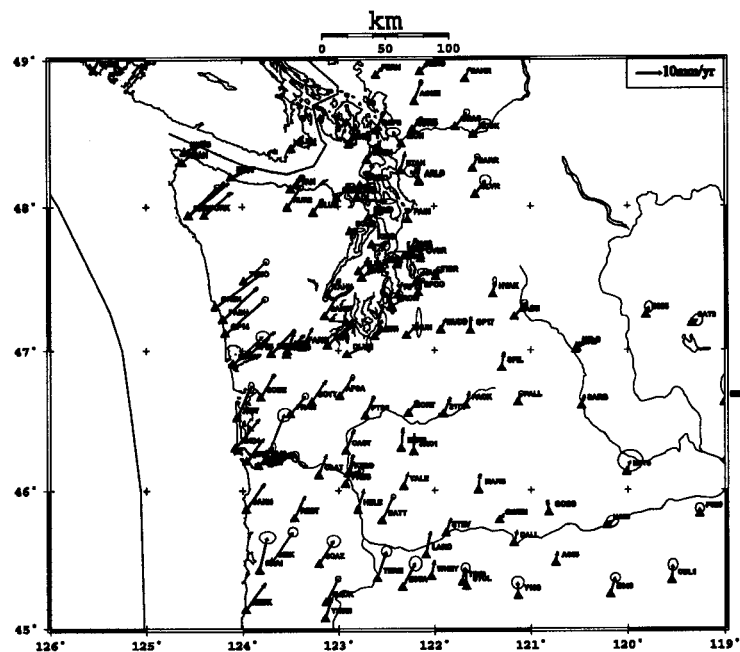


Figure 3.7 GPS data used. Yellow area is water. Data are from both campaign sites and permanent sites in Washington and northern Oregon. Ellipses are the uncertainties estimated from time-series using least squares method (Chapter 2).

The GPS data shown in Figure 3.7 were processed using GIPSY software and Point Positioning strategy (*Zumberge et al, 1997*) with an ambiguity strategy. The absolute positions of all GPS sites are in the ITRF97 reference frame (*Boucher et al., 1997*). Horizontal components of site velocities relative to North America with less than 3.0mm/yr uncertainties were used in subsequent models. A model's misfit was estimated from the variance:

$$\sigma^2 = \frac{\sum_{i=1}^N (\gamma_i)^2}{N-1} \quad (3.26)$$

Here, γ_i is the velocity residual (observed minus calculated) of the i th observation and N is the number of observations. There are 150 velocity vectors (2 components at each site) for a total of 300 observations.

§3.7.2 Geometry parameter sensitivity

Two-dimensional half-space elastic dislocation models have been widely used to study the changes of the surface deformation in early 1990s. Since such models do not consider topography and variations in the shape of the fault along strike, researchers began to use three dimensional models in the late 1990s. *Flüke* (1996) first showed how much each 3-D model parameter can affect the surface deformation in the Cascadia. Because 2-D models are simple and give similar model results to those from 3D models (*Flüke*, 1996), they are still been using in some circumstances. Here, we used the 2D model (Figure 3.8) given in table 3.1 and the method of *Freund and Barnett* (1976) to determine the sensitivities $\partial v_x / \partial X$ and $\partial v_x / \partial Z$ that were used to constrain the magnitude of parameter changes at each iteration of later 3D models:

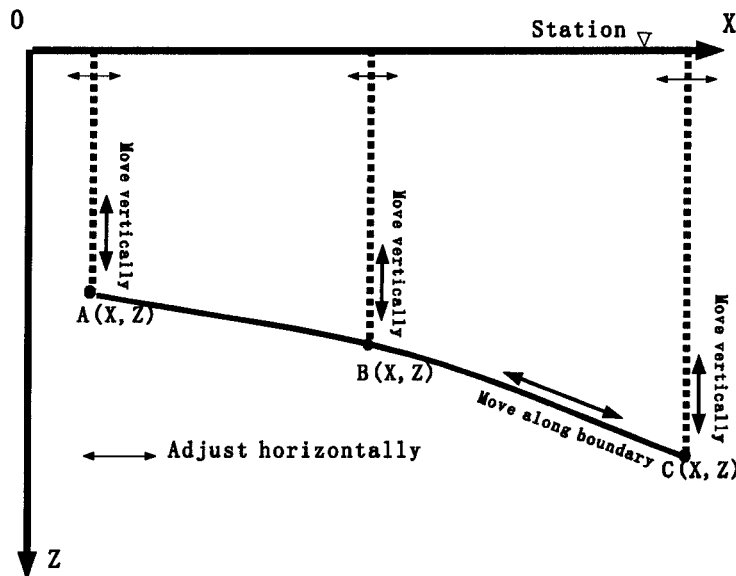


Figure 3.8. Control points used in 2D and 3D models for the Cascadia Subduction Zone. The heavy line is the top of the subducting slab. A, B, C are three control-points that specify the geometry of the subduction slab. In 2D models, each control point has fully adjustable x, z coordinates. In later 3D forward models the control points are constrained to move up and down dip along the circular profile. In the inversion the control points may move vertically as well as up and down dip.

In this 2D model the initial horizontal width of the locked zone is 80km and the initial horizontal width of transition zone is 95km.

Table 3.1 Control points of the initial 2D model

	Point A	Point B	Point C
X(km)	0	80	175
Z(km)	5	13	28
Slip deficit rate(mm/a)	42	42	0

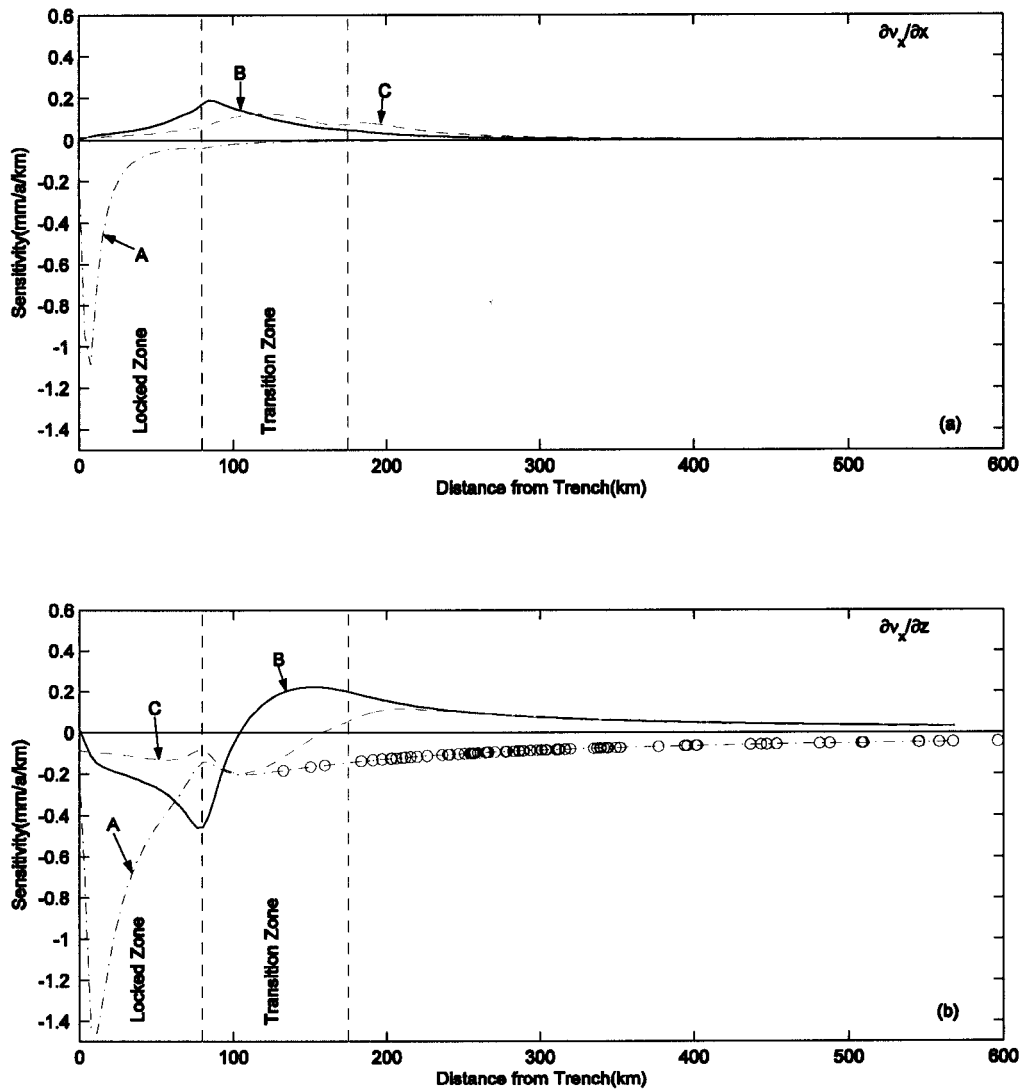


Figure 3.9: 2D model. Sensitivity of horizontal surface velocity V_x to variations in the X, Z coordinates of model control points, A, B and C (shown in Figure 3.8). The upper figure (a) shows the sensitivity to changing X at the control-points. The lower figure (b) shows the sensitivity to changing Z. The dashdotted curve is for control point A, the solid curve is for control point B, and the dashed curve is for control point C. In each figure, the origin is at the trench. The red circles are locations of projected GPS stations between latitude 47°N and 50°N. The vertical dashed lines indicate the boundaries between the locked and transition zones. The model parameters in this figure correspond to a NE cross-section through Seattle.

The program used for 2D model calculations is called *disloc2d* written by Dr. Anthony Qamar. It

calculates uplift, horizontal displacement, and derivatives by using formulae from *Freund and Barnett* (1976). The Cartesian coordinate it adopts is X horizontal pointing in the dip direction, Y horizontal pointing in the strike direction, Z pointing up. The program allows modeling complex faults with multiple segments having different dips and slip rates.

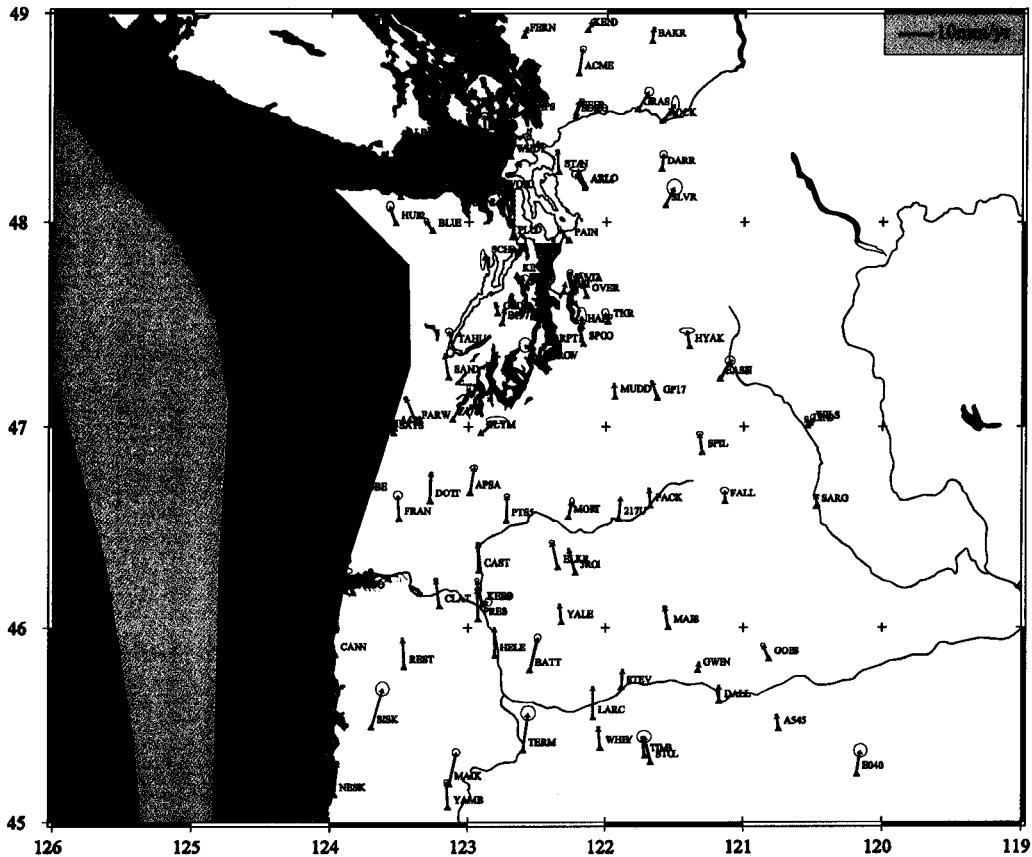


Figure 3.10: Velocity residuals after removing the effect of plate locking on the CSZ

The results (Figure 3.9) show that, for the CSZ, horizontal velocity at the surface is more sensitive to changes in the depths of the locked and transition zones than to changes to the widths of the zones. Any change of control point A is very sensitive to velocities observed at stations right above the trench (more than 1.0mm/a/km). Unfortunately no station has a distance less than 130km from the trench. For sites that are more than 200km away from control point A, changes of model parameters have little effect on site velocities. Hence observed velocities there provide no constraint on the subduction model. For sites along the coast in Washington, the maximum sensitivity to changes in depth and width of the locked and transition zones is about 0.2mm/a/km .

For control points A and B near the surface, site velocities are generally twice as sensitive to depth as to width of the locked zone.

§3.7.3 Three-dimensional inverse modeling

Since the geometry of the CSZ cannot be approximated well using a 2D model, we have used a 3D model to account for plate locking (*Flück et al.*, 1997). However, experiments with 3D models suggest that plate locking alone is not sufficient to explain the observed velocities as seen in figure 3.10. *Khazaradze et al.* (1999) suggested that an additional uniform N-S strain rate was necessary to explain the observed velocities, although this was based on only 7 continuous GPS sites. As seen in figure 3.10, velocity residuals, after removal of the effect of plate locking, show an apparent linear relationship with latitude (Figure 3.11(b)). Their relationship with longitude is not as obvious, but residuals to the west are slightly larger than those to the east (Figure 3.11(a)). *McCaffrey et al.* (2000) showed that clockwise block rotation of western Oregon could explain this effect at sites in Oregon, a mechanism also proposed by *Wells et al.* (1998). To evaluate these mechanisms in Washington, we have used a simplified model, in which Washington is treated as one rigid block, with three tectonic components: 3D elastic deformation from plate locking on the CSZ, a uniform North-South strain rate, and a clockwise rotation of western Washington relative to North America. The three components were inverted simultaneously with N-S and E-W velocities at each site given equal weight. For 3D forward modeling of plate locking on the CSZ, we used the method of *Flück et al.* (1997), which is based on the solution for a point-source dislocation in an elastic half-space medium (*Okada*, 1985). The starting model was identical to the model of *Flück et al.* (1997) and was defined by sixteen east-west profiles along the CSZ. For each profile, there are three control points to control the geometry of the subduction slab similar to those shown in Figure 3.8. In the forward program, the curvature defined by the initial control points is fixed and the control points are only allowed to move landward (positive) and seaward (negative) along the curve of the boundary in the plane of the profile, thus changing the widths of the locked and transition zones without changing its shape; the center of the circular boundary was constrained to be somewhere in the earth. In the inversion, control points A, B, C were allowed to move vertically as well as along the curve of the boundary. This provided 96 free parameters in my model. To account for the supplementary N-S compression in the inversion, we

assumed a uniform N-S strain rate over the whole region. This adds 2 free variables. Finally, clockwise rotation of western Washington adds an additional three free variables: the longitude and the latitude of the pole of rotation as well as the rotation rate. The total number of free parameters in a complete inversion was therefore 101. Since the surface deformation decays with distance away from the trench, stations in eastern Washington and Oregon have little sensitivity to the geometry of the CSZ seismogenic zone. The question arises here whether there are sufficient observations to constrain the parameters of the model. For example stations 200km east of the coast have less than 10% of the sensitivity to the horizontal positions of the subduction slab compared with stations on the coast. If we use 10% as a critical value, there are approximately 98 stations (196 observations) that are sensitive to the geometry of the CSZ (101 free parameters).

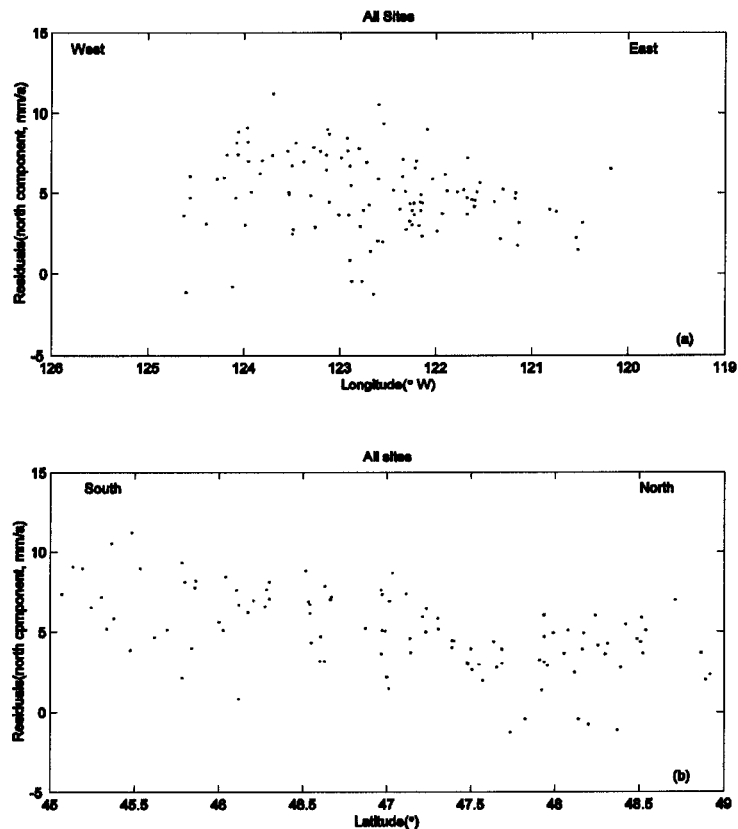


Figure 3.11 The north component of velocity residuals shown in Figure 3.10 as a function of longitude (a) and latitude (b).

In each iteration of the linear inversion, the d_j in equation (3.25) are the observed site velocities. *Flück's* 3-D model is our guess model m_1 in equation (3.25). *Flück & Wang's* program for modeling plate locking was used to calculate the site velocities, $F_j[m_1]$ in equation (3.25), and

partial derivatives of velocities with respect to the model parameters associated with the CSZ, D_j in equation (3.25). Since our guess model m_1 is close to the real model m^* (eq. 3.25) (Flück *et al.*, 1997), the remainder R is ignorable. An inverse program was used to calculate the changes of all free variables for CSZ and block rotation based on equation (3.25) and equations from (3.13) to (3.16). The sensitivities calculated in Figure 3.9 were used to set standards to check if the computed change in a model parameter associated with plate locking Δp_j was reasonable at each iteration. It was required that

$$\left| \left(\frac{\partial v_i}{\partial p_j} \right) * \Delta p_j \right| \leq |v_{io} - v_{im}|, \quad i = 1, N; j = 1, M \quad (3.27)$$

Here, i is the i th station, Δp_j is the computed change to the j th model parameter, $\partial v_i / \partial p_j$ is the sensitivity to this parameter, v_{im} is the velocity from the model, v_{io} is the observed velocity, N is the number of stations, M is the number of free variables. Any Δp_j that failed this condition was set to zero for a particular iteration. In addition, the depth of each point was required to remain greater than 0. Also the depth of point A was required to be smaller than that of point B which in turn was required to be smaller than that of point C. At each iteration the uniform N-S strain rate was computed by least squares from residuals like those in Figure 3.11(b) obtained after removal of plate locking and WB rotation effects. The model variance σ^2 was computed from equation (3.26). The fit of the observed velocities to the final model is illustrated in Figure 3.13.

Assuming the sample variance σ^2 (see equation 3.26) has a χ^2 probability distribution, we can use an F-test (Bruning & Kintz, 1977) to evaluate the influence of each proposed process in the model: plate locking, N-S compression, and block rotation. For example, one could test the significance of the ratio

$$F_{mn} = \sigma_1^2 / \sigma_2^2 \quad (3.28)$$

where σ_1^2 is the variance corresponding to the inclusion of plate locking only in the model and σ_2^2 is the variance corresponding to the inclusion of plate locking plus N-S compression. m and n are the number of degrees of freedom of σ_1^2 and σ_2^2 respectively. Here the number of degrees of freedom f equals the number of observations minus the number of free parameters in the model. In effect, the F-test in this example is used to determine whether the inclusion of N-S

compression or clockwise WB rotation produces a significant reduction in the variance of the model. The inclusion of plate locking by itself produces a significant reduction in the model variance from 64 (mm/yr)^2 ($f=300$) to 17.6 (mm/yr)^2 ($f=204$). The probability p of this happening by chance alone is miniscule ($p < 10^{-20}$). However, after removing the plate locking effect, the remaining variance in the N-S velocities [31.1 (mm/yr)^2] is considerably larger than the remaining E-W variance [4.0 (mm/yr)^2]. This asymmetry is removed by inclusion of a uniform N-S strain rate in the model which again produces a significant reduction in overall model variance to 4.0 (mm/yr)^2 ($f=202$, $p < 10^{-20}$). The inclusion of block rotation for the whole data set (southern Washington and northern Washington combined) produces no significant improvement in the variance.

§3.7.4 Geometry uncertainty of Cascadia subduction zone

In the 3D inverse modeling, we did not compute the uncertainty for each parameter, since we do not know what portion of the uncertainty belongs to plate locking, rigid block rotation, and NS compression. The way to distinguish these three parts is not addressed here. Since we used (3.26) to find the best model, we also can use it to estimate the uncertainty of the geometry of the CSZ by using a two-dimensional elastic dislocation model in a half space. In this model (Figure 3.8), we fix the curvature determined by the initial model and just let the three control points on each profile move freely along the curve as is done in *Flüke and Wang's* (1997) program for 3-D forward modeling. We assume the curve made by the initial 3 control points is a polynomial and then calculate the polynomial coefficients. Any changes in the X and Z coordinates of a control point (along the polynomial curve) will produce a change in the surface displacement because this changes the widths of the locked and transition zones. By keeping two control points fixed and changing the third one can compute a difference between the predicted site velocities from a 2-D model that approximates the 3-D model and the projections of the observed site velocities on the predicted velocities, and compute σ^2 using equation 3.26.

The 2D model parameters used are shown in table 3.2. The locked zone is 80km wide and the transition zone is also 80km wide. The CSZ fault in the 2D model goes roughly through point 125.5°W , 46°N and its strike is parallel to the coast in Washington. For this test of the acceptable limits of model parameters we use actual locations of GPS sites in a swath perpendicular to the

CSZ located roughly between latitude 46° and 49 . The model with minimum σ^2 in each sub-figure is the best. With the degree of freedom $f=153$ and 95% confidence, the critical F-test value is 1.375. The horizontal line in each sub-figure is the critical σ^2 corresponding to the F-test. If σ^2 of a model in sub-figures is greater than the critical σ^2 from F-test, the model is significantly different from the best model at the 95% confidence level. In other words, any model whose σ^2 is smaller than the critical σ^2 from the F-test cannot be distinguished from the best model. This produces an estimate for the uncertainty of the CSZ geometry. Figure 3.12 shows that variation of the downdip boundary of the locked zone (point B) affects site velocity the most. The uncertainty of the horizontal position from GPS data is about 57km for control point A, (25, -38)km for control point B, ± 30 km for control point C.

Table 3.2 Control points of the 2D model used to compute uncertainty in the CSZ geometry

	Point A	Point B	Point C
X(km)	0	80	160
Z(km)	5	15	28
Slip deficit rate(mm/a)	42	42	0

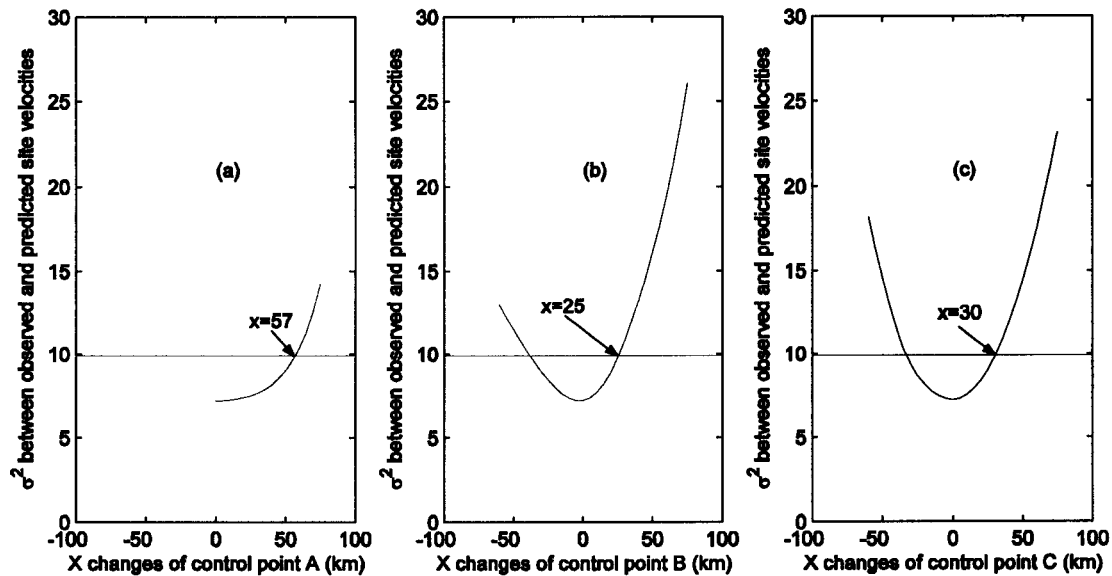


Figure 3.12 Uncertainty of the Cascadia subduction geometry. Values on X-axis are changes in the X-coordinate of control points A, B, or, C from the initial model. Values on Y-axis are σ^2 shown in equation (3.26) where γ_i is the difference between the observed and model predicted site velocities. Horizontal lines are the theoretical maximum σ^2 from F-test. Values with arrows are uncertainties of X-coordinate of control point A, B, C in figure 3.8

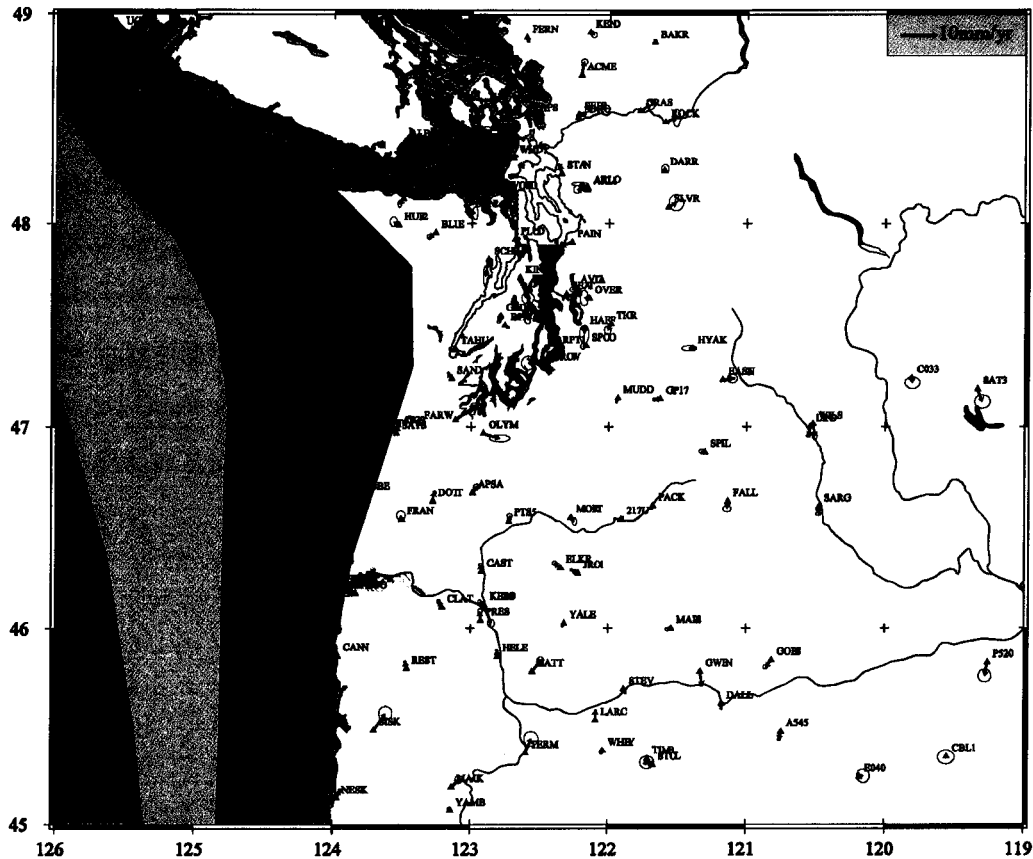


Figure 3.13: Velocity residuals of the best model that takes into account 3D plate locking, WB block rotation, and NS compression. The locked zone and transition zone of the CSZ are shown in different shades of gray. The final model includes a N-S strain rate of -0.94 ± 0.03 mm/deg of latitude per year and a clockwise rotation rate about a pole at 45.8°N , 241.7°E of no more than $0.03^\circ/\text{Ma}$.

§3.8 Summary

We have considered three processes to account for computed horizontal velocities obtained from GPS observations: plate locking, N-S compression and block rotation. In the preferred model, the widths of the locked and transition zones of the CSZ (Figure 1.3) are very close to the model of *Flück and Wang* (*Flück et al.*, 1997). The position of the trench moves less than a kilometer to the west of the model of *Flück et al.* (1997). The depths of the control points along the upper end of the locked zone are 0-2km shallower along the length of the CSZ. The changes of the depths at the lower-end of the locked zone are even smaller, generally less than 1.5km. The depths of the lower end of the transition zone are slightly deeper, but less than a kilometer. In the vicinity of the Olympic Peninsula, this depth is about 28 km. Thus, *Flück & Wang's* model does a good job of

accounting for the contribution of subduction to the observed station velocities. The computed depth of the downward end of the transition zone beneath the Olympic Peninsula is consistent with the geometry of the Juan de Fuca slab beneath western Washington based on intra-plate seismicity and broadband receiver function analysis (*Crosson and Owens, 1987; Lapp et al., 1990; Cassidy, 1991; 1995*).

Khazaradze et al. (1999) noted an apparent N-S strain rate in western Washington of approximately -1.8mm/deg of latitude per year based on data from 7 continuous GPS sites observed over 3 years. In our analysis (150 sites spanning 7 years) we determine a rate of -0.94 ± 0.03 mm/deg of latitude per year corresponding to a strain rate of about -0.84×10^{-8} /yr. By extrapolation, a linear fit to the N-S velocity residuals versus latitude reaches zero at $(51.7 \pm 1.5)^\circ$ N latitude. It is likely that the N-S compression ceases somewhere north of the US-Canada border, but our data do not directly address this question. It is well-known that much of western Washington from the Puget Sound to the Columbia basin is characterized by earthquakes with fault plane solutions having a N-S direction of maximum principal stress (*Qamar and Ludwin, 1992; Ma et al., 1996*). It is probable that the geodetically observed regional N-S strain rate is responsible for much of the earthquake hazard due to shallow faults in western Washington.

McCaffrey et al. (2000) analyzed GPS data in Oregon and found that two mechanisms adequately explain the observations: plate locking and clockwise rotation of the western Oregon block at a rate of 1.05° /Ma about a pole at 45.9° N, 118.7° W. Various paleomagnetic and geological evidence also supports the clockwise rotation of western Oregon by about 1.5° /Ma (*Magill et al. 1982; Beck 1984; Beck et al. 1986; Wells et al. 1998*). We find that on average GPS observations in much of western Washington are explained by a combination of plate locking and regional N-S compression with little contribution from block rotation if we treat Washington as one rigid block. In chapter 4, we will use more GPS data in the Pacific Northwest and improve this model.

However, there is evidence in the data (Figure 3.10) of a transition near latitude 47° from block rotation in Oregon to N-S compression in Washington, as the western block interacts with the unyielding “backstop” provided by basement rocks of northern Washington and southern British

Columbia (*Wang, 1996; Wells et al. 1998*). The details of the transition are still unclear, but an understanding of the transition is presumably related to changes in the style of seismicity (*Ludwin et al. 1991*) and volcanism (*Blackwell et al., 1990; Sherrod and Smith, 1990*) between Oregon and Washington, as well as the major bend in the Cascadia Subduction Zone (Figure 3.13). This is discussed further in chapter 5.

Chapter 4: Rigid block rotation and strain analysis

§4.1 Introduction

Because GPS gives absolute coordinates of places on the earth, it can be used to more easily determine strain, block rotation, and block translation than traditional geodetic methods (e.g. trilateration). GPS is now commonly used to estimate the contribution of elastic strain in the forearc of the subduction zone in response to the plate coupling, and the distribution of primarily NW-directed dextral shear relative to North America plate motion that affects southern California, Oregon, and the Cascadia arc and backarc region (*Pezzopane and Weldon, 1993*). It is hoped that GPS observations will also help to determine the secular deformation that loads crustal faults that cause shallow earthquakes in western Washington.

In Chapter 3, I introduced 3 physical mechanisms to explain observed deformation in western Washington: subduction along the CSZ, rigid block rotation, and regional north-south compression. However, I treated Washington as one simple rigid block and I did not consider data from all GPS sites available in Oregon. Previous studies using paleomagnetic evidence and GPS indicate western Oregon rotates as one rigid block (e.g. *Wells et al., 1998; McCaffrey et al., 2000*). Can Oregon and Washington be treated as one block? If not, how does rotation in Oregon change character in Washington? What is the role of the Cascade arc in the tectonics of the Pacific Northwest? What causes differences in seismicity in Washington and Oregon?

In this chapter, I will use an expanded set of GPS data in the Pacific Northwest to examine these questions. In the following sections, I will present a method to estimate block translation, rotation, and strain, and review previous studies. I will then provide estimates of these quantities based on GPS observations at both campaign stations and permanent stations from 1994 to 2001.

§4.2 Basic Theory

Since the vertical component of the observed station velocity derived from GPS data has a bigger

uncertainty than the horizontal component, I will focus on the horizontal components, v_x and v_y .

Assuming plane strain, we can express v_x and v_y in the following way:

$$\begin{aligned} v_x &= \frac{\partial v_x}{\partial x} x + \frac{\partial v_x}{\partial y} y + v_{ox} \\ v_y &= \frac{\partial v_y}{\partial x} x + \frac{\partial v_y}{\partial y} y + v_{oy} \end{aligned} \quad (4.1)$$

Here, (v_{ox}, v_{oy}) is the rigid-body translation velocity at origin O in a Cartesian coordinate system.

$$\bar{\mathbf{L}} = \begin{pmatrix} \frac{\partial v_x}{\partial x} & \frac{\partial v_x}{\partial y} \\ \frac{\partial v_y}{\partial x} & \frac{\partial v_y}{\partial y} \end{pmatrix} \quad (4.2)$$

is called the deformation velocity gradient tensor.

In the above equations, there are six unknown parameters, so observed velocities (i.e. v_x and v_y) at a minimum of 3 sites are needed to estimate all unknowns. Once this is done, we can calculate a best-fit translation vector (v_{ox}, v_{oy}) for the rigid block, a best-fit local rigid block rotation rate $\dot{\omega}$, and a principal strain rate tensor $\dot{\epsilon}$ as shown below.

The normal $(\dot{\epsilon}_{xx}, \dot{\epsilon}_{yy})$ and shear $(\dot{\epsilon}_{xy})$ strain rates are determined by:

$$\dot{\epsilon}_{xx} = \frac{\partial v_x}{\partial x} \quad (4.3)$$

$$\dot{\epsilon}_{yy} = \frac{\partial v_y}{\partial y} \quad (4.4)$$

$$\dot{\epsilon}_{xy} = \frac{1}{2} \left(\frac{\partial v_x}{\partial y} + \frac{\partial v_y}{\partial x} \right) \quad (4.5)$$

The local rigid-block rotation rate $(\dot{\omega})$ is obtained from velocity gradient tensor by:

$$\dot{\omega} = \frac{1}{2} \left(\frac{\partial v_x}{\partial y} - \frac{\partial v_y}{\partial x} \right) = -\dot{\omega}_{xy} \quad (4.6)$$

One can also rotate the coordinate system so that the shear strain rate $\dot{\epsilon}_{xy}$ is 0. When this is done, the resulting strain rate components are called principal strain rates and are denoted $\dot{\epsilon}_1$ and $\dot{\epsilon}_2$ where:

$$\dot{\epsilon}_1 = \frac{\dot{\epsilon}_{xx} + \dot{\epsilon}_{yy}}{2} + \left[\frac{(\dot{\epsilon}_{xx} - \dot{\epsilon}_{yy})^2}{4} + \dot{\epsilon}_{xy}^2 \right]^{\frac{1}{2}} \quad (4.7)$$

$$\dot{\epsilon}_2 = \frac{\dot{\epsilon}_{xx} + \dot{\epsilon}_{yy}}{2} - \left[\frac{(\dot{\epsilon}_{xx} - \dot{\epsilon}_{yy})^2}{4} + \dot{\epsilon}_{xy}^2 \right]^{\frac{1}{2}} \quad (4.8)$$

From (4.7) and (4.8), we can see $\dot{\epsilon}_2$ is the minimum strain rate. The azimuth of the direction of minimum principal strain rate relative to the unrotated coordinate system, α , can be computed in the following way (*Turcotte and Schubert, 1982*):

$$\alpha = \frac{1}{2} \text{atan} \left(\frac{2\dot{\epsilon}_{xy}}{\dot{\epsilon}_{xx} - \dot{\epsilon}_{yy}} \right) \quad (4.9)$$

In the rotated coordinate system, the $\dot{\epsilon}_1$ axis is perpendicular to the $\dot{\epsilon}_2$ axis. In the following sections, we use the equations above and all observed site velocities derived from GPS to compute the strain rate distribution and translation velocity field in the study area assuming that the assumption of plane strain applies locally.

§4.3 Rigid-Block Rotation

Suppose a small block on the earth's surface is rotating around a vertical axis P, located somewhere else on the earth. If A is one site in the small block, we can calculate the surface velocity caused by rigid block rotation of A about a pole P. The great angle between A and P is α , the rotating rate is ω , the radius of earth is R. Then the surface velocity at A is $\omega R \sin \alpha$,

and its gradient with respect to α is $\omega R \cos \alpha$ which goes to 0 when α is 90° (Figure 4.1). Hence, if a small block is far away from the rotating pole, the velocity gradients at sites within the block are very small. Velocity vectors at sites within such a block are almost uniform and can be treated as translations.

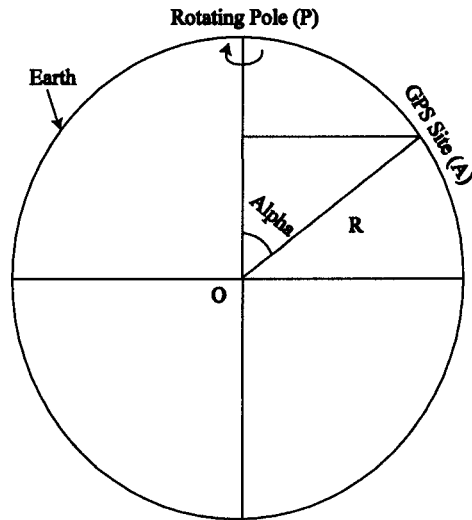


Figure 4.1. Spherical block rotation. The circle represents the earth. P is the pole of rotation of a block containing a site at A. The angle between A and P relative to the center of the earth is alpha.

Using the above method requires us to know the angle alpha between the rotation pole P and the GPS site A, given the longitudes and latitudes of A and P. Figure 4.2 shows a spherical triangle, formed by three intersecting great circles, with arcs of length (a, b, c) and vertex angles of ($\angle A$, $\angle B$, $\angle C$). The angle between two sides of a spherical triangle is defined as the angle between the tangents to the two great arcs, as shown in figure 4.2 for vertex angle B. The arc lengths (a, b, c) and vertex angles ($\angle A$, $\angle B$, $\angle C$) of the spherical triangle in figure 4.2 are related by the following cosine and sine formulae from spherical trigonometry.

$$\frac{\sin a}{\sin \angle A} = \frac{\sin b}{\sin \angle B} = \frac{\sin c}{\sin \angle C} \quad (4.10)$$

$$\cos a = \cos b \cos c + \sin b \sin c \cos \angle A \quad (4.11)$$

$$\cos c = \cos b \cos a + \sin b \sin a \cos \angle C \quad (4.12)$$

If A is placed at the North Pole and we know longitudes and latitudes of B and C (One is a rotation pole, the other is a GPS site) (λ_B, φ_B) and (λ_C, φ_C) , then the great angle a and $\angle C$ (the azimuth angle of point C) can be computed as following:

$$\cos a = \sin \varphi_B \sin \varphi_C + \cos \varphi_B \cos \varphi_C \cos(\lambda_B - \lambda_C) \quad (4.13)$$

$$\sin \angle C = \sin(\lambda_B - \lambda_C) \cos \varphi_B / \sin a \quad (4.14)$$

However if a is small, (4.13) becomes unstable. For such a case, (4.13) and (4.14) can be rearranged,

$$\sin \frac{a}{2} = \left\{ \sin^2 \left[(\varphi_B - \varphi_C) / 2 \right] + \cos \varphi_B \cos \varphi_C \sin^2 \left[(\lambda_B - \lambda_C) / 2 \right] \right\}^{1/2} \quad (4.15)$$

$$\tan \angle C = \frac{\cos \varphi_B \sin(\lambda_B - \lambda_C)}{\cos \varphi_C \sin \varphi_B - \sin \varphi_C \cos \varphi_B \cos(\lambda_B - \lambda_C)} \quad (4.16)$$

(4.16) is preferred for the calculation of C because it is stable when angle a is small (Snyder, 1987).

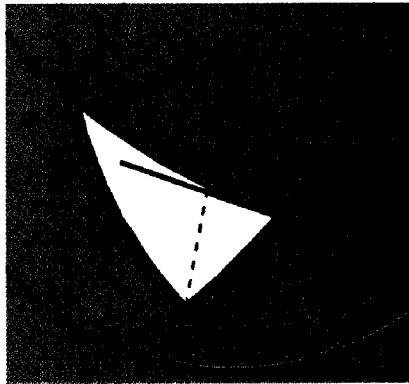


Figure 4.2: A spherical triangles with arcs of length (a, b, c) and vertex angles of $(\angle A, \angle B, \angle C)$

§4.4 Previous studies

Paleomagnetic observations and geological data has suggested that the Oregon block and southern Washington rotate clockwise as a unit with respect to the interior of North America,

causing western Oregon to move northward (*Beck et al.*, 1986; *England and Wells*, 1991; *Magill et al.*, 1982; *Wells*, 1990; *Wells and Coe*, 1985; *Wells and Heller*, 1988; *Walcott*, 1993; *Wells*, 1996; *Wells et al.*, 1998; *Hagstrum et al.*, 1999). Independently, *McCaffrey et al.* (2000) used 71 horizontal GPS vectors and 4 tilt rates in Oregon (a total of 146 observations) to determine a rotation pole for the Oregon block relative to North America. Their result was a pole at $45.9^\circ \pm 0.6^\circ\text{N}$, $241.3^\circ \pm 0.7^\circ\text{E}$ with a clockwise rotation rate of the block of $-1.05 \pm 0.16^\circ/\text{Ma}$. *McCaffrey et al.* noted the pole lay along the Olympic – Willowa Lineament. *Savage et al.* (2000) used 21 GPS vectors from southern Oregon and determined a different pole, 43.5°N , 240°E with a clockwise rotation rate of $-1.66 \pm 0.33^\circ/\text{Ma}$. *Wells et al.* (2001) combined all poles from paleomagnetic and GPS observations and got an averaged pole which is close to the pole given by *McCaffrey*. *Svarc and Savage* (2002) used 75 GPS sites in western Oregon and southwestern Washington and estimated a rotation pole at $43.4 \pm 0.14^\circ\text{N}$, $240.67 \pm 0.28^\circ\text{W}$ and a rotation rate of $-0.822 \pm 0.057^\circ/\text{Ma}$. The possible tectonic mechanisms that have been proposed for Oregon rotation are 1) varying rates of oblique convergence along the Juan de Fuca plate, 2) Basin and Range spreading, 3) Right-lateral shear resulting from the Pacific – North America plate interaction (*Pezzopane and Weldon*, 1993; *Wells and Simpson*, 2001).

Besides estimating rotation, researchers have used various methods to estimate strain in western Washington. For example, *Lisowski et al.* (1989), and *Savage and Lisowski* (1991) found the strain rate near the Olympic Peninsula was $0.09 \mu\text{strain}/\text{yr}$ and near Seattle was $0.04 \mu\text{strain}/\text{yr}$. Early researchers tried to use dislocation models and thermal models of the CSZ to match geodetic observations. However, the observed site velocities do not decrease with distance away from the CSZ plate boundary as rapidly as predicted by subduction dislocation models (*Dragert et al.*, 1994; *Hyndman and Wang*, 1995; *Fluck et al.*, 1997). *Khazaradze and Qamar* (1999) analyzed three years of continuous GPS data from seven permanent sites and proposed that an additional N-S oriented contraction of $\sim 4\text{mm}/\text{yr}$ over a distance of 250km was present in western Washington besides the dominant Juan de Fuca and North America convergence. *Johnson et al.* (1999) used marine high-resolution and conventional industry seismic-reflection data and found that the Quaternary slip rate across the Seattle fault zone is about $0.7 - 1.1 \text{ mm}/\text{yr}$. *Murray and Lisowski* (2000) combined triangulation, trilateration, and GPS data to get the horizontal strain

rate in the Pacific Northwest. They concluded that shear-strain rates are significantly greater than zero in the forearc zone, but not significant in the arc and backarc regions. *Miller et al (2001)* found 6 – 7 mm/yr north-south contraction within the Washington forearc from GPS observations.

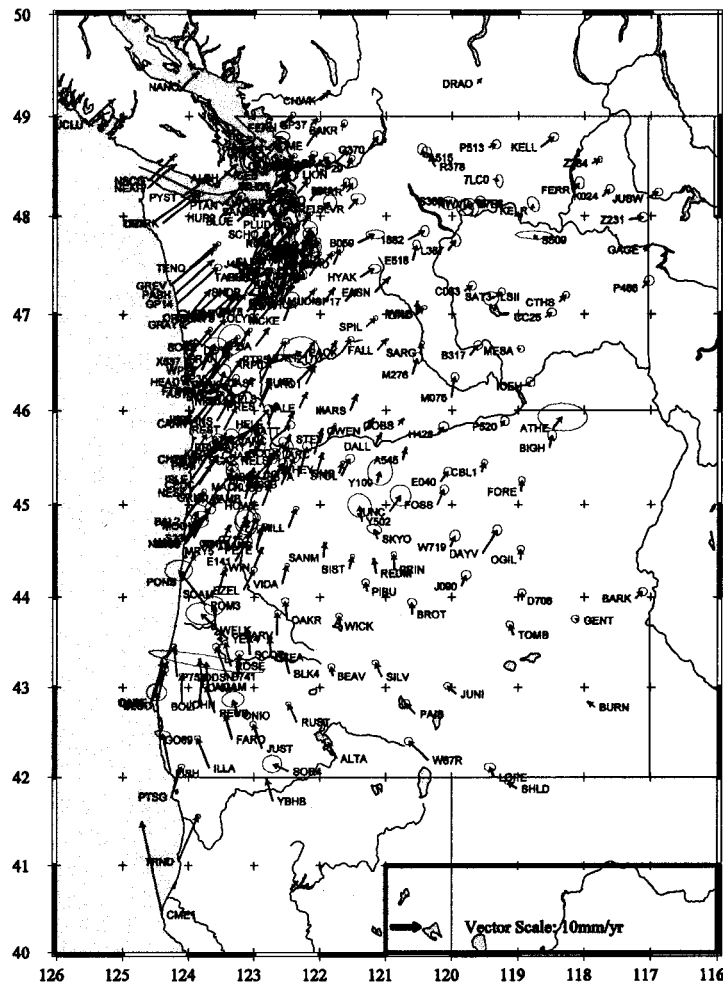


Figure 4.3 The observed site velocity field in the Pacific Northwest relative to stable North America. GPS data from 1994 to 2001 at more than 300 GPS sites, including both campaign and permanent stations.

§4.5 Data resources and analysis

In this chapter, I consider an expanded data set of more than 300 GPS sites including both permanent and campaign sites (Figure 4.3) (In Chapter 3, only a subset of these data were considered, sites mostly in Washington). I used data from the U.S. Geological Survey (USGS),

the Pacific Northwest Geodetic Array (PANGA), the U.S. Coast Guard CORS Array, the IGS, the NGS HARN (National Geodetic Survey High Accuracy Reference Network), the Western Canada Deformation Array (WCDA) of the Geological Survey of Canada (GSC), the University of Washington, the Rensselaer Polytechnic Institute (RPI), and the Oregon State University (OSU). The data were collected from 1994 to 2001. The time span for most sites is more than 4 years. During the 2001 GPS campaign, RPI and UW added some new sites in Oregon, Washington, and Canada, and in particular filled in an area in northeastern Washington. Some of these sites have been observed only twice. Some of the data were processed using GIPSY software using fiducial free orbit solutions, point positioning strategy (*Zumberge et al., 1997*), and ambiguity resolution. The results were expressed in the ITRF2000 reference frame. RPI data were processed using precise satellite orbits and GAMIT/GLOBK analysis software (*King and Bock, 1999; Herring, 1998*) in an ITRF97 reference frame. All site velocities were obtained from analysis of latitude and longitude time-series by using least squares and are expressed relative to the North America (NA) reference frame by removing NA-ITRF97 or NA-ITRF2000 rotation. Only horizontal velocity components whose uncertainty is less than 3mm/yr were used here.

§4.6 Strain rate and translation velocity calculation

The computer program used to calculate both strain rate and the translation velocity of crustal sub-blocks is *straingps* written by Anthony Qamar. It is based on the equations in section §4.2. The program uses least squares to determine unknown parameters in equation (4.1) from site velocities measured on the surface of the Earth. It sets up a local 2 dimensional coordinate system with x pointing to east, y pointing north. The origin is set at the averaged x, y site positions in the input data. The program first converts longitude and latitude in spherical coordinates to local x, y Cartesian coordinate in units of kilometers and computes a "flat-earth" approximation to the strain rates. The output includes longitude, latitude, the maximum principal strain rate $\dot{\epsilon}_1$, the minimum principal strain rate $\dot{\epsilon}_2$, the azimuth of the $\dot{\epsilon}_2$ axis, the standard error of $\dot{\epsilon}_1$ and the standard error of $\dot{\epsilon}_2$. The longitude and latitude are the coordinates of the local frame's origin. The standard errors are 1-sigma estimates of the error in $\dot{\epsilon}_1$ and $\dot{\epsilon}_2$. An additional option of the

program produces the estimated translation vector V_{ox} , V_{oy} , together with $\dot{\omega}$, and error estimates $ErrV_{ox}$, $ErrV_{oy}$ (see equation 4.1). Using this program, we can get the best-fit strain rate, translation vector, and regional rigid block rotation simultaneously.

In order to produce a smoothed view of the spatial variation of strain rate, we have divided the Pacific Northwest into hundreds of small cells. Each “rectangular” cell has dimension of 0.5° in both longitude and latitude. At each node in the grid we compute strain rate parameters by using data from sites within 100km, say, of the grid point. A rigid block rotation $\dot{\omega}$ is computed for each small cell. All sites in the cell are given equal weight in the computation. 3 or more sites are required in each cell for computing all unknown parameters in equation (4.1).

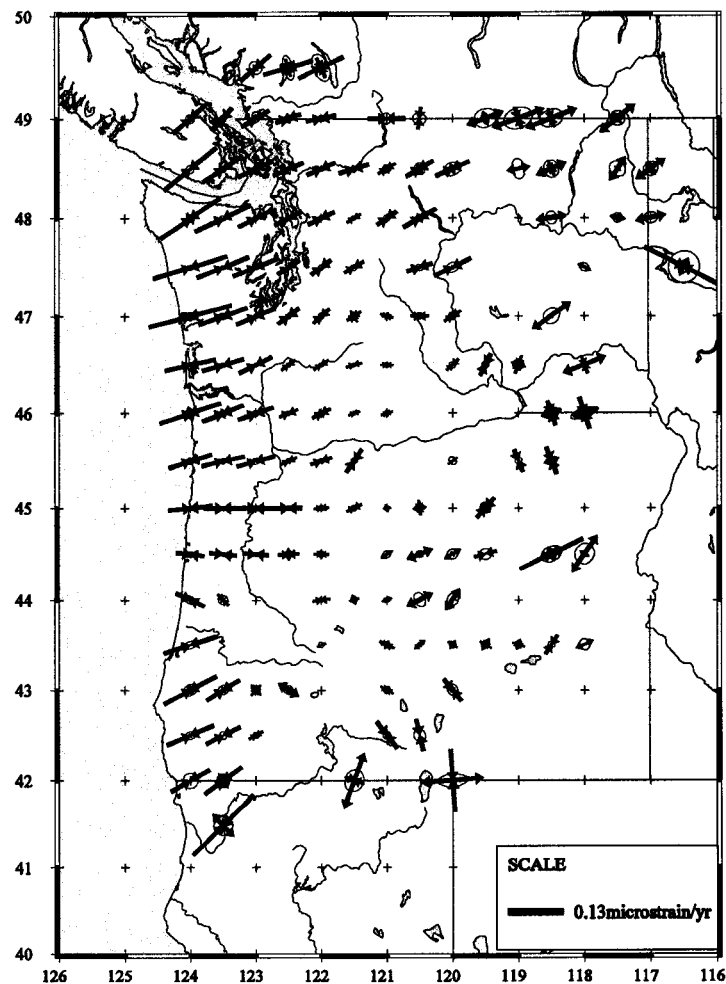


Figure 4.4 Principal strain rates in the Pacific Northwest. Both permanent and campaign GPS data from 1994 – 2001 were used. Outward pointing arrows indicate positive (extension) principal strain rate. Inward pointing arrows indicate a negative (compression) principal strain rate. Ellipses are estimated in one sigma standard errors

Figure 4.4 shows that the principal strain rates near the coast are uniaxial and oriented approximately along the direction of JDF – NA convergence, although some of the strain is more normal to the trench than the plate convergence direction. This result is consistent with previous studies (e.g. *Murray MH and Lisowski, 2000*). On the Olympic peninsula, the strain rates are $\epsilon_1 = -0.013 \pm 0.007 \mu\text{strain/yr}$, $\epsilon_2 = -0.083 \pm 0.008 \mu\text{strain/yr}$ N56°E. In the Puget Sound, ϵ_1 is about $0.007 \pm 0.005 \mu\text{strain/yr}$, ϵ_2 is about $-0.034 \pm 0.007 \mu\text{strain/yr}$ N63°E. These strain rate estimates are very consistent with those *Savage et al.* calculated in 1991. In Mt. Rainier, ϵ_1 is about $-0.005 \pm 0.005 \mu\text{strain/yr}$, ϵ_2 is about $-0.020 \pm 0.006 \mu\text{strain/yr}$ N53°E. In northern Oregon coast, ϵ_1 is about $-0.004 \pm 0.005 \mu\text{strain/yr}$, ϵ_2 is about $-0.051 \pm 0.014 \mu\text{strain/yr}$ N85°E. In central Oregon, ϵ_1 is about $0.011 \pm 0.006 \mu\text{strain/yr}$, ϵ_2 is about $-0.010 \pm 0.006 \mu\text{strain/yr}$ N71°E. The strain rates decay rapidly away from the coast and reach minimum values in central Washington and central Oregon. The onshore area in western Oregon mainly shows east-west compression, while other onshore areas show northeast-southwest convergence. In northern and eastern Washington, and in eastern Oregon, strain rates are larger and have various orientations, but the results may be misleading because of greater uncertainties there. These areas are so far from the Cascadia Subduction Zone (CSZ) that the CSZ's influence is relatively small. Therefore, any detectable strain in these areas would be of interest because it would be caused by tectonic forces unrelated to the CSZ.

We use the same program (*straingps*) to compute translation velocity for the center of mass of each cell. Along the Canada – US boundary, the translation vectors should be close to zero but are biased by stations that exist only to the south in the smoothing process (see Figure 4.3). In northeastern Washington, since we do not have enough data, the estimated site velocities have large uncertainties; thus the computed translation vectors there are also very uncertain. In eastern Washington and eastern Oregon, we also have poor data coverage. The translation velocities there reflect large scale smoothing (Figure 4.5). From northern California to northern Washington, directions of station motion change from northwest to northeast. Stations along the northern California and southern Oregon coasts move northward with almost the same rates (Figure 4.5). Some nodes in northern and eastern Washington, eastern Oregon, and northern California do not

have translation vectors since circular cells at these nodes do not contain sufficient sites with uncertainty less than 3.0 mm/yr.

The translation velocity field (Figure 4.5) is a smoothed version of the site velocity field shown in figure 4.3. However, it is useful to look in detail in figure 4.3 to evaluate some inconsistencies in figure 4.5. Figure 4.3 shows that a few stations in close proximity to one another move in different directions, for example, LIND and WILS in Ellensburg, ARP0 and PTS5 in southwestern Washington, and some sites located in Puget Sound and along the central Oregon

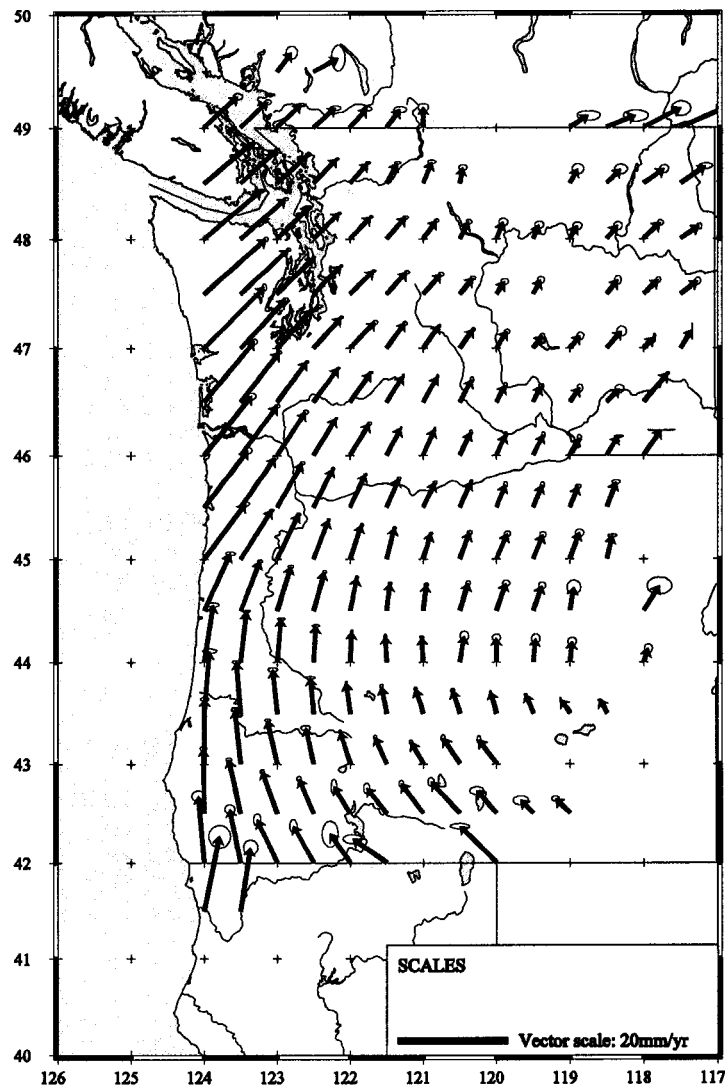


Figure 4.5 Smoothed translation vectors in the Pacific Northwest. The components of the translation vectors are V_{ox} and V_{oy} from equation 4.1. The uncertainty of each vector is derived from a least squares fit to site velocities within 100km of each grid point. More than 300 GPS sites including both permanent and temporary sites were used.

coast. The north component time series of LIND and WILS are very similar, while the east components differ (Figure 4.3). North of Lake Chelan, sites such as 7LCO, A515, R378 move to the northwest, which differs from other stations nearby. Also there is a lot of variation in the uncertainty of site velocities computed for each velocity vector. Most permanent sites and some campaign sites, like OLYM, MORT, THUN, APSA, have small uncertainties. Other sites like ARP0, 9040, ATHE, and some sites in southwest Oregon, have large uncertainties. Different places have a varying density of GPS stations. Generally, western Oregon and the Puget Sound have a high station density whereas the Olympic Peninsula, the arc, and back-arc areas have low station density. In the rest of this chapter, I will use the smoothed translation velocity field shown in figure 4.5 for all my work. However, as described above, there are still some sites where apparent inconsistencies need to be addressed in the future.

§4.7 Rigid Block Rotation in Oregon and Washington

Paleomagnetic evidence, geological data, and GPS data suggest western Oregon is rotating clockwise (*Wells, 1998; McCaffrey et al., 2000; Savage et al., 2000*). In Oregon the smoothed velocity field in Figure 4.5 clearly shows a clockwise block rotation whose pole is somewhere in eastern Oregon, and this rotation appears to affect parts of Washington. However, in Washington the velocity vectors are nearly parallel, so the applicability of block rotation is not as clear as in Oregon. We first check if Oregon and Washington can be treated as one rigid block. To do this we calculate a theoretical pole of rotation for all available data after removing the effect of the CSZ plate coupling and check the residuals to see how good our original assumption is. We use a program to estimate a rotation pole by least squares called *findpole* written by Anthony Qamar. It uses equations in section 4.3 to find a best - fit rotation pole for a given block containing GPS sites. The best estimated pole for the combined Washington-Oregon block is at $245.11 \pm 0.30^\circ\text{E}$, $45.53 \pm 0.11^\circ\text{N}$ with a clockwise rotation rate of $-0.55 \pm 0.02^\circ/\text{Ma}$, which is just east of the figure. Most sites do not match well (as judged by the large residuals) except in central Washington and central Oregon (Figure 4.6).

To improve the fit we try an alternative method. Since previous studies have shown that a rigid

block rotation model fits Oregon data well, we begin by using the Oregon data only to get the rotation pole and assume Washington is rotating around the same pole with the same rotation rate. This gives a residual map shown in Figure 4.7. The estimated pole of rotation is located at $243.18 \pm 0.18^\circ\text{E}$, $44.80 \pm 0.06^\circ\text{N}$ and the estimated rotation rate is $-0.9^\circ/\text{Ma}$. This assumption fits the data

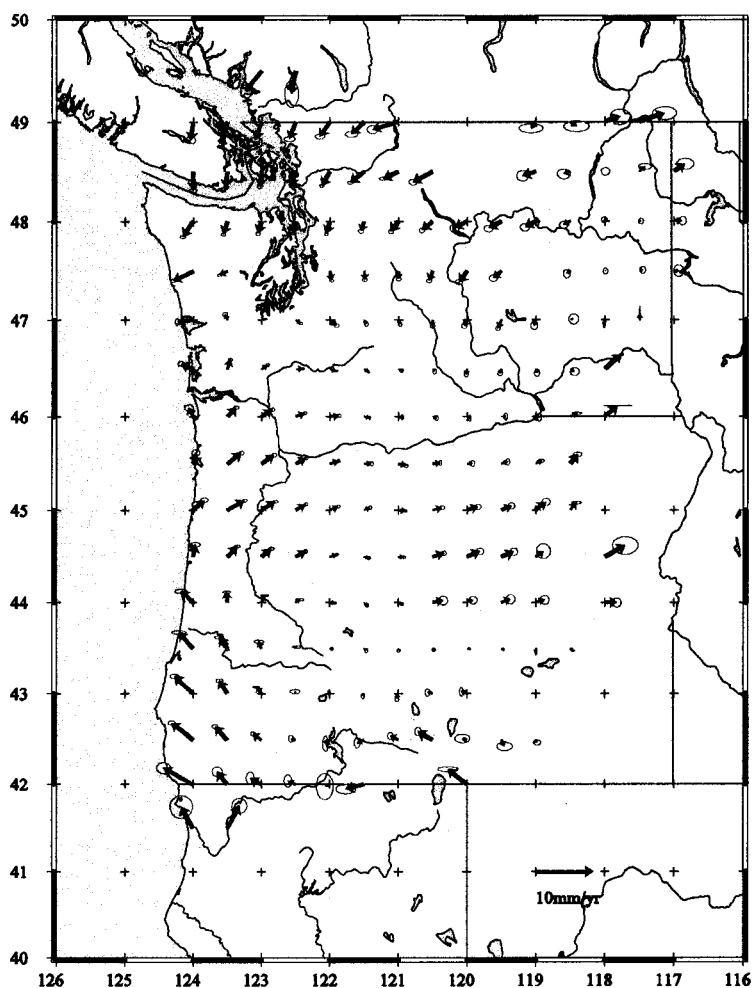


Figure 4.6. Vectors shown here are the residual velocities after removing plate locking and clockwise rigid block rotation assuming Oregon and Washington act as one rigid block.

in Oregon and southern Washington very well, but not the rest of Washington. In the coastal area in southwestern Oregon, residual vectors at several sites point to the west with relatively large magnitudes. This may indicate an inappropriate Cascadia Subduction Zone model in southwest Oregon or tectonic complexity there (*Miller et al., 2001*). From Oregon to Washington, the residuals become steadily larger. North of latitude 46.5°N , the residuals show a counter-clockwise

rotation indicating that the rigid-block rotation model of Oregon does not fit large areas of Washington. This suggests that Oregon and Washington are not one rigid block.

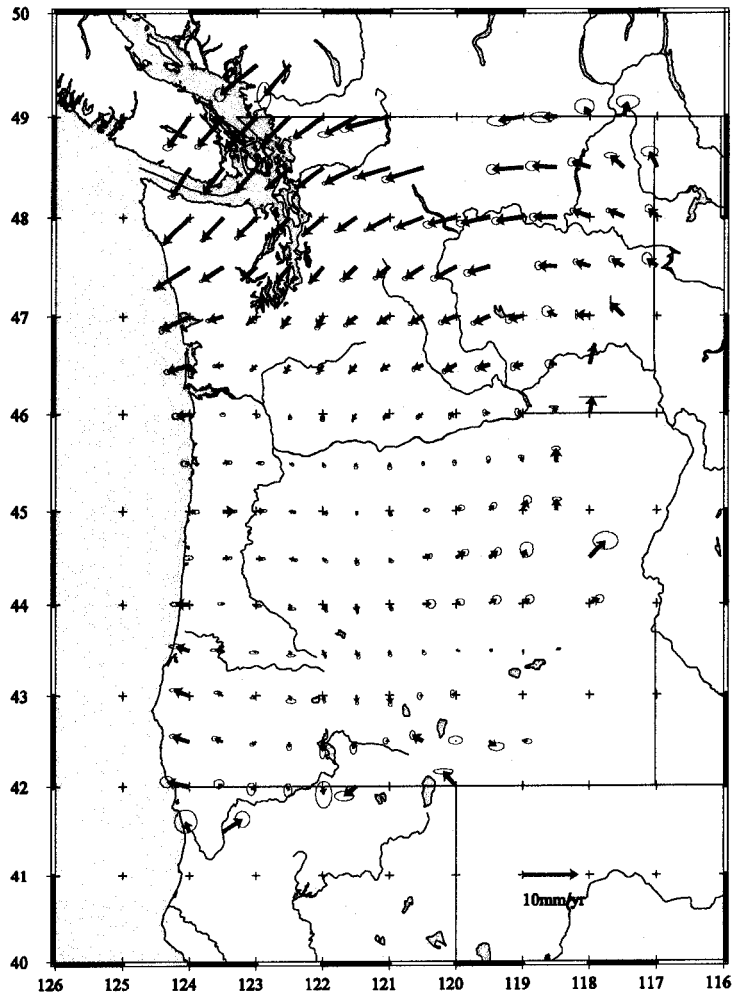


Figure 4.7. Residuals after removing contributions from plate locking and rigid Oregon block rotation. The assumption here is that Washington rotates around the same pole as Oregon with the same rate estimated from Oregon data

We next attempt to divide Washington and Oregon into two rigid blocks with a boundary at 46°N as suggested by the residual pattern shown in Figure 4.7. Assuming Washington is a rigid block and using the same approach as before we obtain an estimated pole of rotation for Washington at $247.56 \pm 1.04^\circ\text{E}$, $44.43 \pm 0.48^\circ\text{N}$ with a clockwise rotation rate of $-0.32 \pm 0.04^\circ/\text{Ma}$ which is only one third of the rotation rate of the Oregon block. We also estimated the maximum principal residual strain rate for this block which indicates a roughly north-south compression with a magnitude of $0.85\text{mm}/\text{yr}$ per degree of latitude (Figure 4.8). In western Washington along the coast, residuals of some sites point west or northwest, suggesting that either the CSZ plate

locking is over-estimated, or the assumption that Washington is one rigid block does not work well. Residuals of some sites in the southwest Washington coast decrease quickly from west to east and from south to north, and reach zero at the northern Olympic Peninsula and the Cascade arc. The residuals at northern Washington sites point to the south, indicating north-south compression in western Washington. The three northeast sites have big residuals, most likely caused by that fact that there are insufficient data to estimate accurate velocities there. The same situation exists in southeastern Washington where there are insufficient data (Figure 4.8). Most sites fit the Washington block rotation model reasonably well.

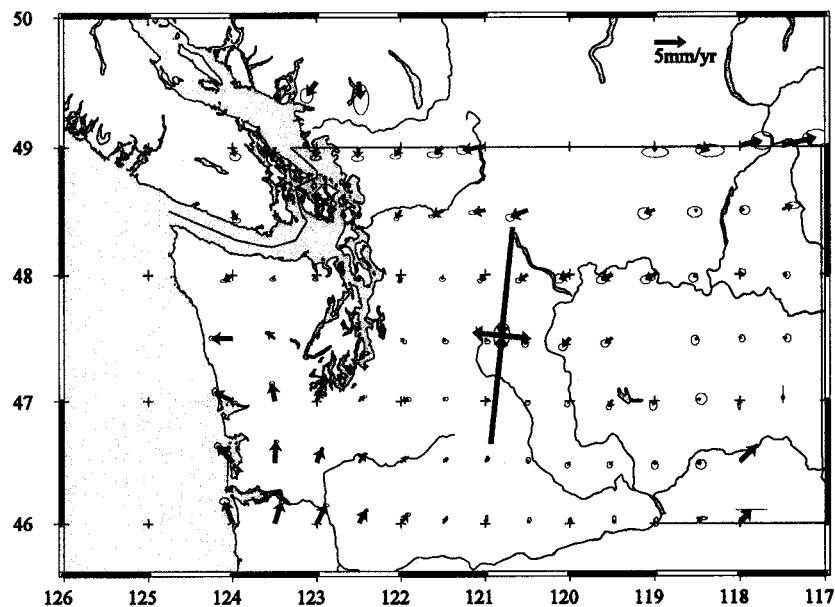


Figure 4.8 Assume Washington is in one rigid rotating block separated from Oregon. Then compute the rotation of Washington after removing effects from the CSZ and estimate a principal residual strain rate after subtracting CSZ plate locking and rotation contributions from the site velocities. Red arrows are final velocity residuals. Blue arrows are principal strain rates. Inward arrow means compression. Outward arrow means expansion. The magnitude of the minimum principal residual strain rate is about -0.84mm/yr per degree of latitude.

We have treated Oregon and Washington as two different blocks. After removing effects of the CSZ, the GPS site velocities yield poles and rotation rates different in Oregon and Washington. The residual figure 4.9 shows that such a model can match the observed velocity data reasonably well. Comparing figure 4.7 and figure 4.8, the area between 46°N and 47°N may act as a transition zone, since the residuals in figure 4.7 increase gradually and in figure 4.8 decrease gradually from south to north. Using the two estimated poles of rotation, we can calculate theoretical site velocities in the Pacific Northwest (Figure 4.10). On the arbitrary 46°N boundary

between these two blocks, the velocity of sites on the Oregon side differs from sites on the Washington side. Since Oregon rotates faster than Washington, this model implies that Washington is being compressed across this boundary, with the largest compression along the coast and smaller compression further inland. In reality, this compression is probably distributed throughout Washington, rather than just at the block boundary. In eastern Washington, the only mechanisms likely to affect site velocities are block rotation and regional strain accumulation unrelated to the CSZ plate coupling, because the CSZ has negligible influence there (Figure 4.9). Near the coast the N-S compression rate between the Oregon and Washington blocks for the 2 – block model is around 5mm/yr, and the averaged strain rate in Washington is about 2.5mm/yr. Residuals in northern Washington are still large and suggest a counter-clockwise rotation, which means we over-estimated the rotation in this area. The big residuals in southwestern Washington

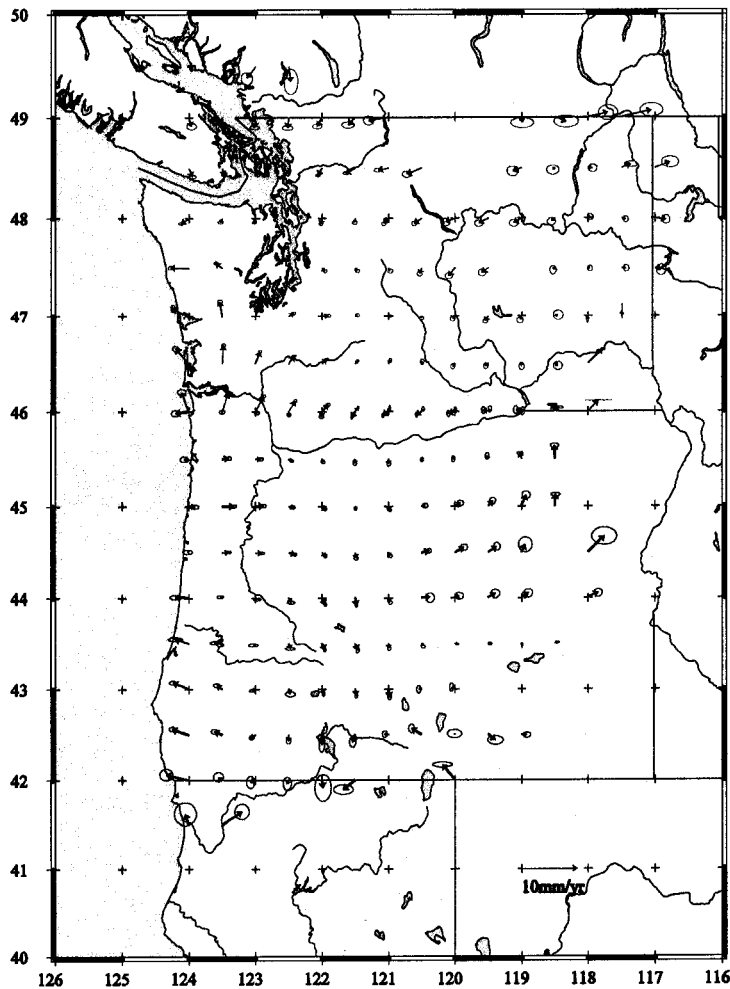


Figure 4.9 Residuals in the Pacific Northwest. Blue vectors are for Oregon block, red vectors are for Washington block.

also suggest that we under-estimated the rotation there. An obvious question is how the interaction between the Oregon and Washington blocks affects the tectonics in the Pacific Northwest and why different areas in Washington and Oregon have different earthquake distributions (Figure 4.11). The variation in seismicity suggests that the assumption that most of Washington is one rigid block is an oversimplification.

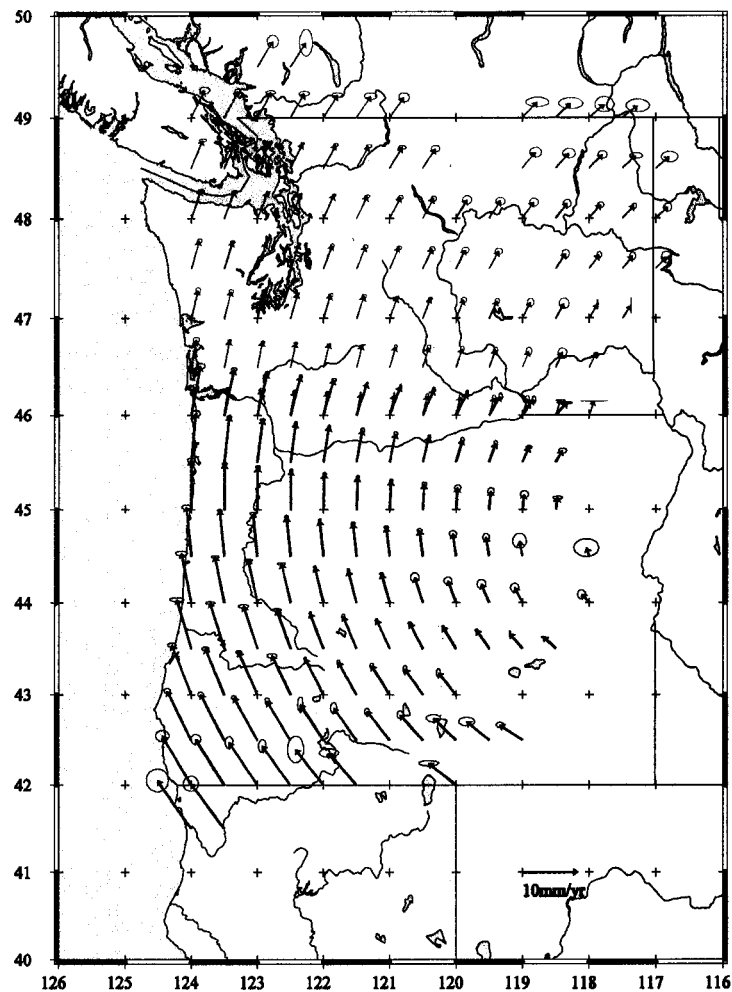


Figure 4.10 Theoretical site velocities resulted from two estimated poles for Oregon and Washington blocks. Blue vectors are from the Oregon pole, red vectors are from the rotation pole of Washington.

§4.8 Where are the Block Boundaries?

From the previous section we know the Pacific Northwest is not one rigid block, and Washington also does not act as one rigid block. It is difficult to distinguish block boundaries from GPS data

alone. We will use seismicity, geology, heat flow, and volcanic data to help us identify appropriate boundaries.

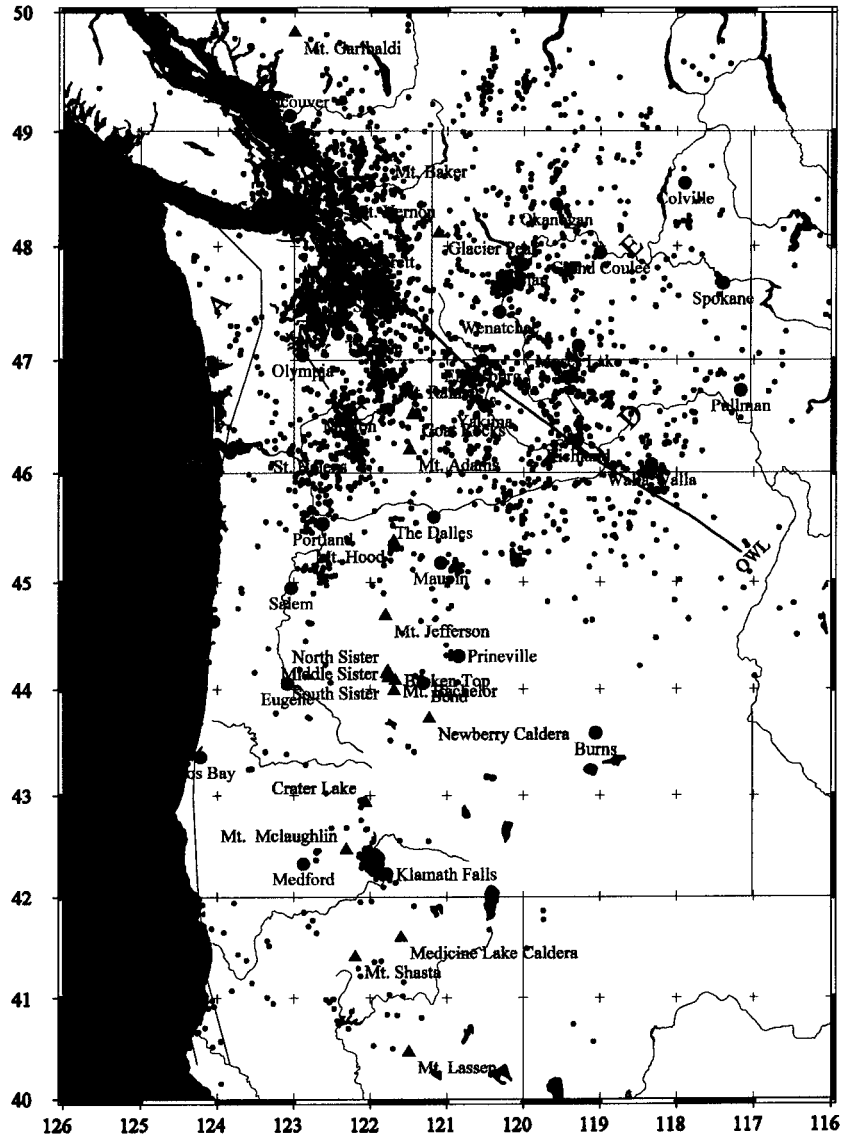


Figure 4.11 Seismicity and sub-block separation. Blue triangles are volcanoes. Red circles are cities. Small dots are shallow earthquakes whose depths are less than 30 kilometers and magnitudes are greater than 2.0. Blue lines are the boundaries of the CSZ. Thin red lines are faults. Thick red line is the Olympic - Wallowa Lineament (*Raisz, 1945*). The capital letters A, B, C, D, E are sub - blocks.

In the Pacific Northwest, earthquakes mainly occur along the Juan de Fuca-Pacific plate boundary, and in British Columbia, Washington, Oregon, and northern California. Few earthquakes occur along the CSZ. Crustal seismicity in Washington concentrates on a north-south strip from the Georgia Strait - Puget lowland to Portland just west of the volcanic arc. Along the

Washington coast there are very few earthquakes. Under the Cascades there is a seismicity gap. In the back-arc, earthquakes are shallower, with 0 – 15km depths, and occur mainly from Richland to Moses Lake, and from Yakima to Ellensburg. Southwest of Chelan there is also a concentration of seismicity. Compared to Washington, Oregon is seismically inactive (Figure 4.11). Thus, seismicity seems to confirm that there is a tectonic boundary between Oregon and Washington.

Based on the distribution of approximate 2800 volcanic vents in the Pacific Northwest and northwestern Nevada in the past 16Ma, *Guffanti and Weaver* (1988) separated the volcanoes into six segments. Two of the segments are in Washington and one is in Oregon. Volcanoes in Washington are stratovolcanoes with a smaller magmatic extrusion rate than Oregon. They form a compressive arc (*Wells et al.*, 1998). In Oregon, volcanoes form an extensive arc with a high rate of magma extrusion. The Washington Cascade Range has high surface elevations and topographic relief (*Reiners et al.*, 2002).

There are several other lines of evidence that suggest Washington and Oregon may be divided tectonically into smaller blocks. The thickness of the Coast Range (CR) reaches a maximum of 24 – 32 km beneath west central Oregon (*Tréchu et al.*, 1994) but is only 20km beneath southwestern Washington (*Stanley et al.*, 1987; *Tréchu et al.*, 1994; *Parsons et al.*, 1998) and the pre-Tertiary terranes of Vancouver Island (*Hyndman et al.*, 1995). Western Washington contains several east-west or northwest-oriented faults which separate the forearc into folded basement and small blocks that may act independently (Figure 4.12), such as the Bellingham, Chehalis, Everett, Seattle, and Tacoma basins (*Pratt et al.*, 1997). Paleomagnetic evidence and geodetic studies show that western Oregon has a larger clockwise rotation than Washington as we have seen (*Wells et al.*, 1984, 1998, 2001; *McCaffrey et al.*, 2000; *Savage et al.*, 2000; *Svarc et al.*, 2002; this study). Heat-flow data in the Pacific Northwest shows that Washington has lower heat flow than Oregon (*Blackwell et al.*, 1990a; *Gutscher et al.*, 2003). Furthermore, the dip of the slab in the Cascadia Subduction Zone is shallower in Washington than in Oregon. *Gutscher et al.* (2003) suggested that the flat subduction between 46° and 49° has a causal relation to the observed variation in heat flow and seismicity. All these characteristics indicate that Washington and Oregon cannot be treated tectonically as one rigid block (Figure 1.3) (*Wells et al.*, 1998) and

support the idea of a boundary near 46°N. The evidence also suggests ways to further divide Cascadia into additional sub-blocks.

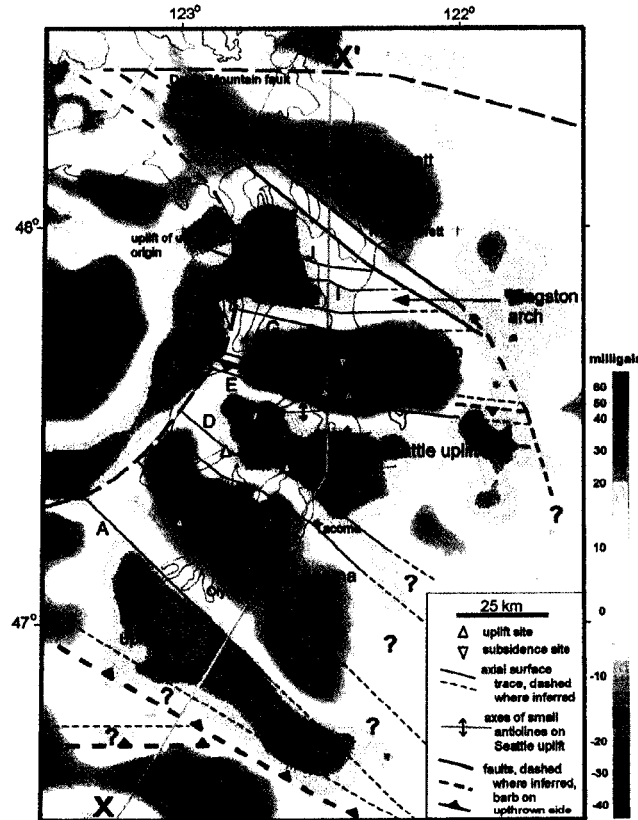


Figure 4.12 Bouguer gravity map of the Puget Sound overlain by locations of faults and the surface projections of axial surface of folds (letters A-K, M) interpreted from the seismic reflection, geologic and potential field data. Bouguer gravity values are residual values after removing wavelengths greater than 100 km (Finn et al., 1991); low values (blue and green) generally correspond with basins and high values (red) with uplifts, the exception being the Olympic Mountains core rocks which are of relatively low density. The triangles denote uplifts and inverted triangles denote subsidence 1000 to 1100 years ago (Bucknam et al., 1992), Axial surface F is the active tip of the Seattle fault. Figure is extracted from *Pratt et al. (1997)*.

From the last section we have concluded that Washington does not act as one rigid block. The Cascade arc separates Washington into a fore-arc and a back-arc and serves as a possible block boundary (Figure 1.3). The depths of crustal seismicity in the fore-arc are greater than in the back-arc and little seismicity exists beneath the arc, again suggesting that the Cascades form a natural boundary. The Cascade arc consists of Tertiary to recent magmatic rocks. The Puget Lowland – Willamette Valley is composed of continental and marine sediments as well as volcanoclastic rocks underlain by lower and middle Eocene marine basalt of the Crescent Formation (e.g. *Wells et al., 1984, Snavely, 1987*). Continental thickness is ~20km at the coast

line, ~30km beneath the Coast Range, ~40 – 45km beneath the arc, and ~30 – 38km under the Columbia Plateau (*Parsons et al.*, 1998). Heat flow in the fore-arc is low, ~ 35–50 mW/m². The maximum heat flow, ~ 120 – 150 mW/m², is found in the Cascade arc (*Gutscher et al.*, 2003). In northeastern Washington, heat flow is greater than 70 mW/m² while in southeastern Washington it is 60 mW/m². So again, the arc appears to be a natural choice for a block boundary in Washington.

The Olympic Peninsula is the largest onshore continental area in the Cascadia Accretionary Wedge (Figure 1.10, Figure 1.11 in Chapter 1). The core rocks of the Olympics have been locally exposed and uplifted since ~18 million years ago. The uplift has exposed the Crescent formation and tilted the peripheral sequence into eastward-dipping anticlines (*Tabor et al.*, 1978). The core of the Olympics is separated from eastern coast range terrane and Puget Sound by the Hurricane Ridge Fault (Figure 1.13) (*Tabor et al.*, 1978). Combined with changes in the seismicity pattern in Washington (section 1.2.2.2 in chapter 1 and the beginning of this section), the geology suggests that a N-S boundary at 123°W is a natural block boundary to divide the fore-arc in western Washington into an outer fore-arc block (the Olympic block) and an inner fore-arc block.

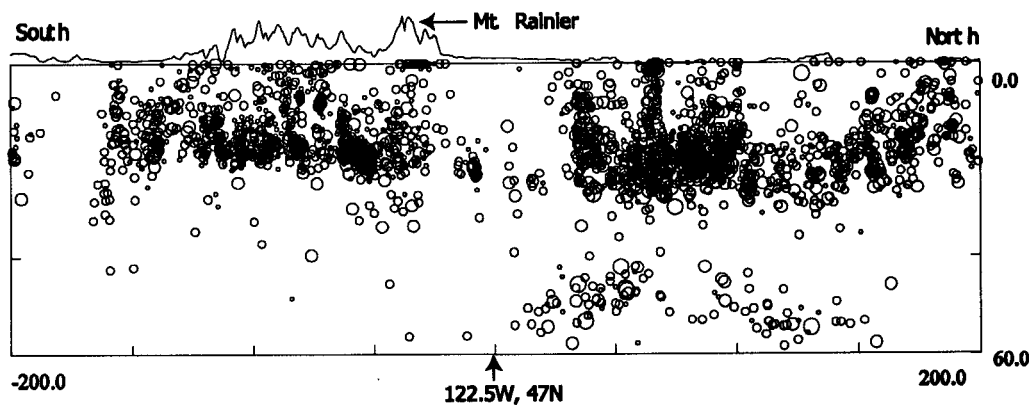


Figure 4.13. Cross section of earthquake hypocenters centered at 122.5°W, 47°N. Left of the figure is south. Events from 1969 to 2002 that fall in ±200km on N-S direction, ±10km on E-W direction, and depth from 0 to 60km are used in this figure.

There is evidence that the inner fore-arc block should be further subdivided at 47°N. For example, according to *Guffanti and Weaver* (1988), there exists a 90km wide gap in the volcanism of the arc which may be related to the shallower subduction slab beneath the Puget Sound (*Crosson and Owens*, 1987). There is a similar gap in seismicity at latitude 47°N (Figure 4.13). The number of

Quaternary volcanic eruptions and the number of volcanic vents decrease dramatically north of Mount Rainier (*Wells et al.*, 1998). In addition, the Puget Lowland contains E-W folds and faults, together with depositional basins north of 47°. The basins are filled with sedimentary sequences eroded from the Olympic Mountains during Miocene uplift and during Pleistocene glaciation (*Tabor*, 1972). The southern Washington Cascades are filled with a large volume of Tertiary sediments and volcanics which have high velocity in the upper crust (*Miller et al.*, 1997). Thus, the Puget Sound to the north and the Mt. Rainier/Mt. St. Helens area to the south have different tectonic expressions, suggesting a boundary separating the inner-fore-arc at 47°N.

In the back-arc, seismicity concentrates mainly in the Yakima fold and thrust belt. Northeastern Washington is possibly part of the stable North America plate. The so-called Olympic – Wallowa Lineament (OWL) (*Raiz*, 1945) appears to tectonically separate the Yakima fold belt from northeastern Washington. Heat flow in northeastern Washington is higher than southeastern Washington (Figure 1.14) (*Blackwell et al.*, 1990a). So we tentatively divide eastern Washington into two sub-blocks: the northeastern block and the southeastern block (Yakima block).

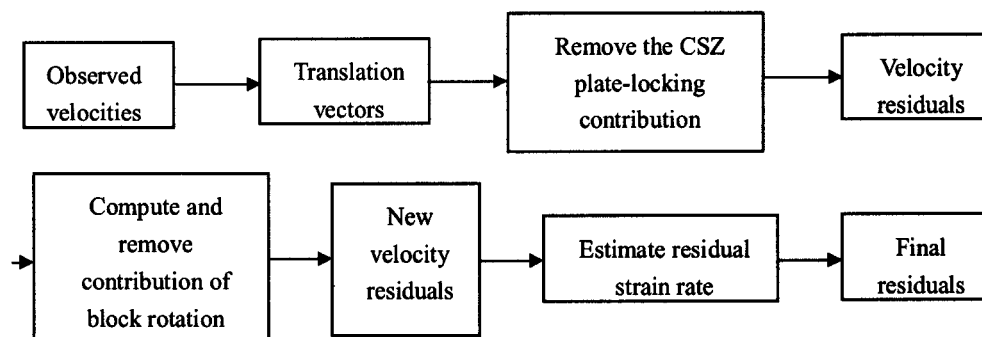
For the purpose of geodetic modeling, we have defined five small sub-blocks in Washington and one big block in Oregon. Details about these blocks are in Table 4.1.

Table 4.1. Sub-block Separation in Washington State (Figure 4.11)

Name	Simple Description	Longitude(°W)	Latitude(°N)
Coast Block (A)	Coast area from Columbia river to southern Vancouver Island includes the Olympic Peninsula.	125 – 123	46-49
Puget Sound (B)	Puget Sound with high seismicity and range from the Olympia to the U.S.-Canada border	123 – 121.2	47 – 49
Mt. Rainier (C)	Range from Portland to Olympia including Mt. Rainier, Mt. Adams, Mt. St. Helens	123 – 121.2	46 – 47
Yakima (D)	Southeastern Washington	121.2 – 116	46 – 47
Northeast (E)	Northeastern Washington	121.2 – 116	47 – 49

§4.9 Strain rate and block rotation

We can extend the analysis procedure of section 4.7 to the 5 sub-blocks in Table 4.1. We use the 3D modeling program from *Wang* (Pers. Comm.) and *Fluke et al.* (1997) to remove the contribution to site velocities from the Cascadia Subduction Zone using the plate – locking geometry calculated in Chapter 3. Then we compute block rotation and residual strain rate distribution in each of the new sub-blocks. The flow chart of the processing procedure is:



The program *findpole* is used to find a best-fit rotation pole and rotation rate from horizontal components of surface deformation velocity. It is an iterative non – linear fitting procedure that requires initial estimates of the unknown parameters. As described in the last section, the program does not converge well to a solution if the block is distant from the pole. Strain rates are computed using equations in section §4.2.

All estimated poles are listed in Table 4.2. The Oregon block has the biggest clockwise rotation rate of $0.90 \pm 0.03^\circ/\text{Ma}$. Its pole is at $243.18 \pm 0.18^\circ\text{E}$, $44.8 \pm 0.06^\circ\text{N}$. This pole is near the border between Oregon and Idaho and is very close to the Olympic-Wallowa lineament (OWL), different from the pole given by *Rob McCaffrey et al.* (2000) and the poles from *Savage et al.* (2000) and *Svarc et al.* (2002). However, the location is still within the confidence ellipse of the rotation pole for the Oregon Coast fore-arc block with respect to North America as given by *Wells et al.* (2001). The Mt. Rainier block in SW Washington rotates clockwise at a slower rate than the Oregon sub-block. Its pole is at $243.87 \pm 1.46^\circ\text{E}$, $44.81 \pm 0.46^\circ\text{N}$ with a rate of $0.66^\circ/\text{Ma}$.

Paleomagnetic and geologic evidence in this area also shows small-scale tectonic rotation in southwest Washington (*Wells, 1985, Hagstrum 1999*). In the Puget Sound block (B), site-velocity vectors are similar in magnitude and nearly parallel, so the location uncertainty of the estimated pole is large. The rotation rate here is not significantly different from zero. In eastern Washington blocks (block D and E), most site velocities are small and uncertainties are large (Figure 4.3). Their estimated rotation poles are farther to the southeast. The computed uncertainties in the rotation rates are probably under-estimated in Table 1.2. In general the clockwise rotation of subblocks appears to decrease from south to north (Oregon to Washington). Site velocities clearly decrease to almost zero in southern BC so the rotation must stop somewhere north of the US – Canadian border but the details of what happens to the rotation in northern Washington is still unclear and will require more data in the future.

Table 4.2 Estimated poles for all blocks in the Pacific Northwest

Block Name	Longitude(°)	Latitude(°)	Rotation Rate ² (°/Ma _s)	RMS of final residual ⁴ (mm/yr _s)
Oregon Block	243.18±0.18	44.8±0.06	-0.90±0.03	1.07
A ¹	249.28±8.61	44.90±1.96	-0.32±0.19	1.58
B ¹	266.29±30.61	31.56±26.39	-0.08±0.11	0.75
C ¹	243.87±1.46	44.81±0.46	-0.66±0.16	0.52
D ¹	254.73±7.99	40.93±4.62	-0.16±0.11 ³	0.77
E ¹	249.27±3.22	43.12±2.13	-0.21±0.09 ³	1.09

¹: For the definitions of these block, please refer to Table 4.1

²: '+' means counter-clockwise rotation, '-' means clockwise rotation.

³: Uncertainties probably under-estimated because uncertainties in the velocity vectors were not taken into account.

⁴: The RMS is for the final residuals. The procedures to get them is in the above flow chart.

⁵: 'a' or 'yr' means 'years', 'Ma' means 'million years'.

After removing contributions to the site velocities from CSZ plate coupling and rigid block rotation, we can use the residuals to calculate residual strain rate in each sub-block (Table 4.3). The Oregon block has the smallest residual strain accumulation, with $\epsilon_2 = -0.001 \pm 0.001$ $\mu\text{strain/yr}$. It also has the biggest block rotation rate. The residual strain in the Oregon sub-block is therefore not significant. CSZ plate locking and rigid block rotation are sufficient to explain the observed crustal velocities (*McCaffrey, 2000; Savage et al., 2000; Svarc et al. 2002; Wells, 1998, 2001*). The lack of strain may explain why seismicity in Oregon is much less than in Washington. At the same time, the Oregon is experiencing a small east-west extension with a rate of $0.002 \mu\text{strain/yr}$.

The Mt Rainier sub-block is defined here as extending from 46°N to 47°N latitude. Its minimum (compressive) principal residual strain rate ϵ_2 is -0.015 ± 0.001 $\mu\text{strain/yr}$ oriented in the direction of N31.54°E. Over the whole block, this is equivalent to 1.7mm/yr of compression. From Mt. Rainier to the Puget Lowland, the direction of the minimum residual strain rate rotates closer to north, but has about the same magnitude of -0.013 ± 0.001 $\mu\text{strain/yr}$ oriented N25°E. This is equivalent to 3mm/yr of shortening across block B (Puget Sound), slightly smaller than Khazaradze's (1999) result of 4mm/yr north-south compression over a distance of 250km.

In the Yakima sub-block (D), the dominant strain accumulation is a marginally significant north-south compression with a rate of -0.01 ± 0.004 $\mu\text{strain/yr}$, N6.26°E, equivalent to 1.1mm/yr compression across the block. For northeast Washington (block E), an approximate E-W extension dominates it with a rate of 0.007 ± 0.001 $\mu\text{strain/yr}$. Due to lack of good data there, this apparently significant result may not reflect the real situation. This area will need more survey work.

The residual strain in the Olympic sub-block (A) shows both E-W extension and N-S compression and the largest strain rates. The compressive rate is 0.017 ± 0.001 $\mu\text{strain/yr}$, equivalent to 6mm northward contraction across the Olympics each year.

Table 4.3 Residual strain and translation in pacific northwest

Block Name ¹	Principal Strain Rates ($\mu\text{strain/yr}$)			Translation (mm/yr)	
	$\epsilon_1 \pm 1\sigma$ ²	$\epsilon_2 \pm 1\sigma$ ³	Θ (°) $\pm 1\sigma$ ⁴	$V_e \pm 1\sigma$	$V_n \pm 1\sigma$
Oregon	0.002 \pm 0.001	-0.001 \pm 0.001	155.44 \pm 8.54	0.01 \pm 0.28	0.01 \pm 0.20
A	0.019 \pm 0.005	-0.017 \pm 0.001	179.23 \pm 2.70	0.00 \pm 0.24	0.00 \pm 0.11
B	-0.001 \pm 0.001	-0.013 \pm 0.001	25.06 \pm 4.67	0.00 \pm 0.10	0.00 \pm 0.84
C	0.002 \pm 0.001	-0.015 \pm 0.001	31.54 \pm 3.17	-0.01 \pm 0.08	0.01 \pm 0.05
D	0.003 \pm 0.001	-0.010 \pm 0.004	6.26 \pm 7.67	-0.00 \pm 0.14	0.00 \pm 0.17
E	0.007 \pm 0.001	0.000 \pm 0.001	168.84 \pm 10.41	0.00 \pm 0.19	-0.02 \pm 0.84

1. for the block names, refer to Table 4.1
2. the maximum principal stress, '+' means extension represented by outward-pointing arrows
3. the minimum principal stress, negative values is compression represented by inward-pointing arrows
4. Azimuth of ϵ_2 measured clockwise from North.

Figure 4.14 shows that the residuals to the multi-block model are small. The computed RMS of the residuals for each sub-block is less than 1.6 mm/yr (Table 1.2). Thus the multi-block model

matches the observations very well. However, relatively big residuals in northeast Washington and northeast Oregon still exist where we have sparse data. Large residuals along southern Oregon coast may come from inadequate modeling of plate locking on the CSZ or from an over-simplified geometry of the 3-D subduction model. For more discussion, please refer to Chapter 5.

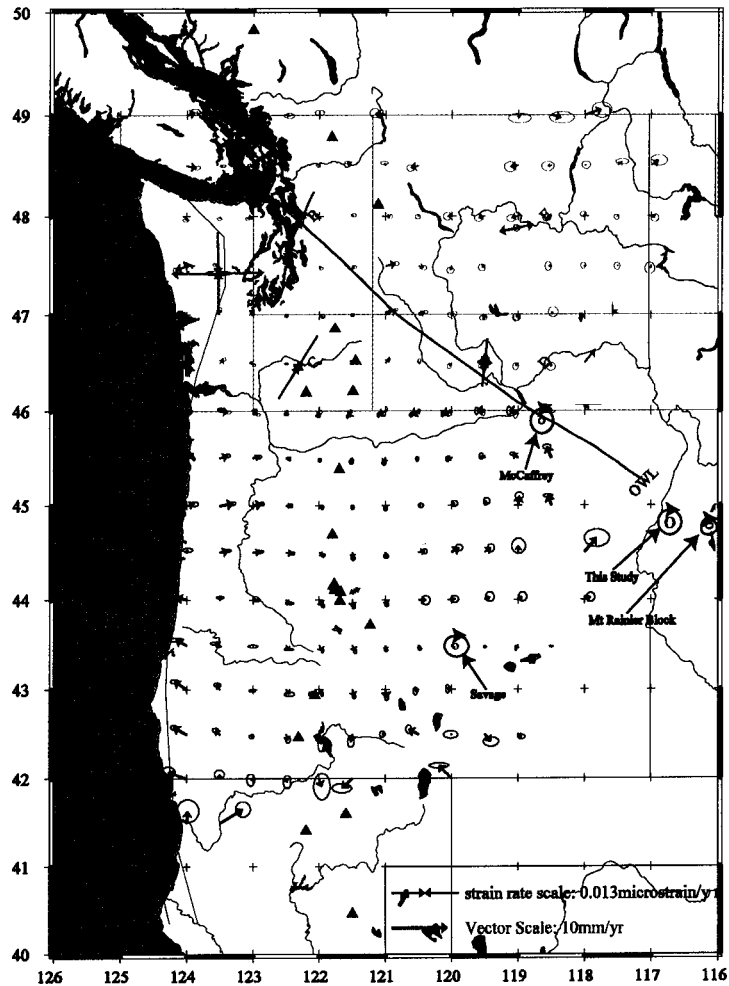


Figure 4.14. Residual vectors of averaged site velocities and principal strain rates for a multi-block model. All residuals are from removing the contributions from plate locking, rigid block rotation and strain within each block. Blue vectors are the principal residual strain rates estimated from the residuals after removing both CSZ and block rotations' contribution in each sub-block. Locations of rotation poles for Oregon are presented by circles with an arrow and an "o" character. Arrows indicate sources (McCaffrey et al. 2000, Savage et al. 2000). The other pole, marked with an "O", is from this study. Rotation pole for Mt. Rainier block is also plotted.

Chapter 5: Discussion

§5.1 Introduction

In the previous two chapters, we have used a 3-D inverse model to obtain the geometry of the Cascadia Subduction Zone and we have found a preferred model to explain the observed velocity field in the Pacific Northwest. In this chapter, I will further discuss the CSZ geometry, sub-block boundaries, and the mechanisms causing surface motion, and I will interpret the results using available geologic, volcanic, and seismic data. I will also focus on several interesting areas within the sub-blocks.

§5.2 The Cascadia Subduction Zone (CSZ)

Hyndman and Wang (1993) argued that the geometry of the CSZ is controlled primarily by temperature. The updip limit of the locked zone is controlled by the transition of stable sliding clays like smectite to illite and chlorite at 100 - 150°C. This transition occurs by dehydration of the clays. The temperature at the deformation front is about 250°C. They argue that the temperature controlling the downdip limit of the locked zone is about 350°C, where a critical transition occurs from seismogenic velocity-weakening to stable-sliding velocity-strengthening. The downdip limit of the transition zone is at a temperature around 450°C, where feldspars begin to behave plastically. They concluded that the fully locked zone is about 40km wide beneath the outer shelf of Vancouver Island, and the transition zone extends another 60km to the east, where it reaches the coast. They estimated that the widths of the locked and transition zones are slightly wider along the Oregon margin and much wider near the Olympic Peninsula under Washington. *Dragert et al.* (1994) compared tide gauge data, leveling data, gravity data, and horizontal strain data with the predictions from elastic dislocation and viscoelastic models. Their elastic model has a locked zone 40km wide and a transition zone 60 km wide. They also produced a viscoelastic model with a wider locked zone and a narrower transition zone. *Dragert and Hyndman* (1995) obtained a locked zone and a transition zone of comparable widths at southern Vancouver Island and the northern Olympic Peninsula by using GPS data: each zone was 80 – 100 km wide.

Hyndman and Wang's (1995) dislocation model for the entire length of the CSZ indicates that the total width of the locked and transition zones changes from 70km in central Oregon to northern California (35km locked, 35km transition) to 180km in northern Washington (90 + 90 km) and 120km in Vancouver Island (60 + 60 km) with a uncertainty of about 15% or 10km. A 3D elastic dislocation model developed by *Flück* (1996, 1997) with a width of 40 + 40 km for Oregon, 100 + 100 km for Washington, and 60 + 60 km for Vancouver also fits deformation data reasonably well. *Khazaradze and Qamar* (1999) suggested that the maximum locked and transition widths of the seismogenic zone under the Olympic Peninsular reach 100 km and 130 km respectively, based on data from seven permanent GPS sites. In 2001, *Wang et al.* developed a 3D viscoelastic interseismic deformation model and found that some inland sites will actually have seaward motion (SW) during the early interseismic period after a great megathrust earthquake. By 300 years after the earthquake, all stations are moving to the NE as observed today. They did not find that the CSZ geometry required a significant change from the elastic dislocation - based model. *Gutscher et al.* (2003) adopted finite element thermal models of six transects across three different subduction zones in the world and obtained a 170km (100 + 70 km) wide seismogenic zone in their Olympics – Puget Sound transect thermal model, and a 140km (80 + 60km) wide seismogenic zone in their central Oregon thermal model. *Wang et al.* (2003) revised previous 3D elastic dislocation model by using a slip deficit rate that changes exponentially with downdip distance, rather than linearly. They introduced a new concept for the transition zone based on the new slip deficit rate function which is called the “effective transition zone” (ETZ). This modified model yielded a width for the locked zone that was similar to earlier models, but a width for the transition zone that was twice as wide as *Flück's* model.

My analysis of GPS data in Chapter 3 using a 3-D elastic dislocation model in a half space, required only small shifts in the positions of the locked and transition zones given by *Flück et al.* (1997). The northern part of the trench moves westward, generally less than 1.5 kilometers. The central part migrates less than 2.0 km westward while the southern part moves less than one kilometer westward. The transition zone at the north part of the CSZ was made wider by less than one kilometer. At the bend of the CSZ, the transition zone is less than one kilometer wider than the transition zone in *Flück's* model. In the central part of the subduction zone between latitude

44° and 46°, the locked zone is 0 – 3 kilometers wider and the transition zone moves less than one kilometer eastward with no width change. The southern part of the subduction below latitude 44° is unchanged. In general, the widths of the locked zone and transition zone did not require significant changes from Flück's model.

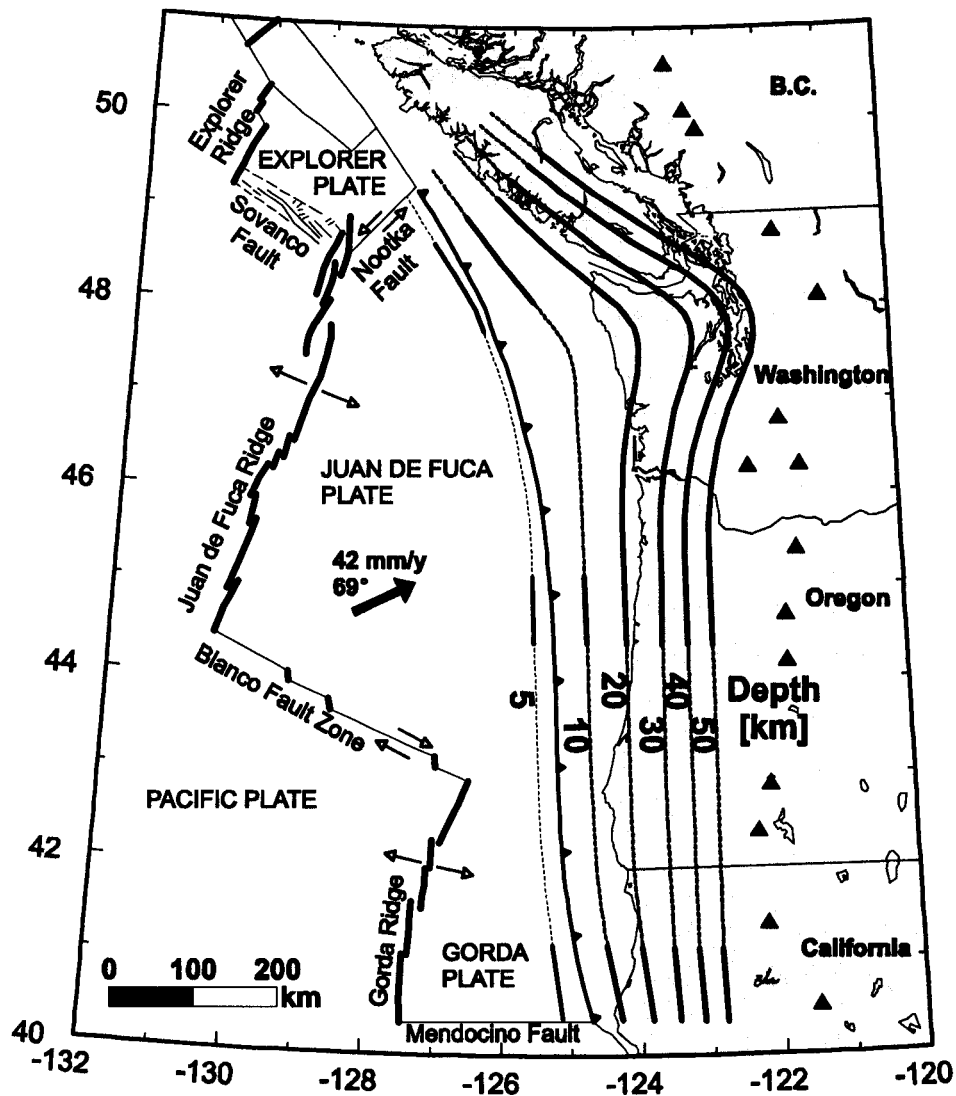


Figure 5.1. Depth contours on the top of the Cascadia subducting slab. The numbers are the depth in km below sea level. Solid lines are well defined by seismicity data. Dashed lines are extrapolated. The triangles are volcanoes. This map is adopted from Flück et al, 1997.

The depth contours of the top of the Cascadia subducting slab (Juan de Fuca plate) are well defined by seismic data from earthquake in the Benioff-Wadati zone, seismic reflection and refraction data, and teleseismic waveform analysis and tomography in Vancouver Island,

Washington and northern California (Figure 5.1). The depth of the upper seaward part of the slab is known mainly from marine multichannel seismic reflection data. The depth of the middle part below 60km is constrained mainly by Benioff - Wadati earthquakes (Figure 5.2). The geometry of the deep part of the slab is known from seismic tomography.

Along Vancouver Island, multichannel seismic reflection and refraction yield a good image of the CSZ slab (e.g. *Hyndman et al.*, 1990, 1994) whose depth is in good agreement with receiver function analysis results using teleseismic broadband seismometer data (*Cassidy et al.*, 1993, 1995) and the depths of Benioff – Wadati zone earthquakes (*Rogers et al.*, 1994). Beneath northern Washington, the slab depths are well constrained by active Benioff – Wadati zone seismicity. *Crosson and Owens* (1987) analyzed receiver functions of teleseismic waves and the depths of local earthquake hypocenters, and determined the position of the slab between depths of 20km and 60km quite well. The slab in the northern part of CSZ has been detected to a depth of at least 400 km (*Bostock and VanDecar*, 1995) by seismic tomography.

Beneath southern Washington and Oregon, the slab has been detected to 300km and 150km respectively using tomography (*Rasmussen et al.*, 1988). Oregon does not have much Benioff – Wadati zone seismicity to define the shallow part of JDF plate boundary. However, *Tréhu et al.* (1994) used observations from a seismic experiment between 44° and 46° to show that the slab in Oregon extends to a depth of 50km. In the southern part of the CSZ, the slab is mainly constrained by Benioff – Wadati zone seismicity (e.g., *Wang and Rogers*, 1994).

Our 3-D model has a trench that is shifted westward less than 1.5 kilometers compared to the model of *Flück and Wang*. The lower end of the locked zone is less than one kilometer shallower at the bend of the CSZ and less than 1.5 kilometers deeper to the north and south of the bend. The bottom end of the transition zone extends a little bit deeper, generally less than 1.5 kilometers.

Flück and Wang's Cascadia subduction geometry model is based on a depth-contour map of the top of the subducting slab, constrained by seismic data (Figure 5.1). Their estimated error for the seaward end of the slab based on seismicity is $\pm 0.5\text{km}$ and increases to $\pm 5\text{km}$ at a depth of 50km.

Our model is not significantly different than theirs and there are no abrupt bends in the plate along the margin.

Given the average slip displacement d and the fault area A , we can calculate the seismic moment M_0 released by an earthquake on the CSZ by using the formula (Aki and Richards, 1980)

$$M_0 = \mu d A \quad (5.1)$$

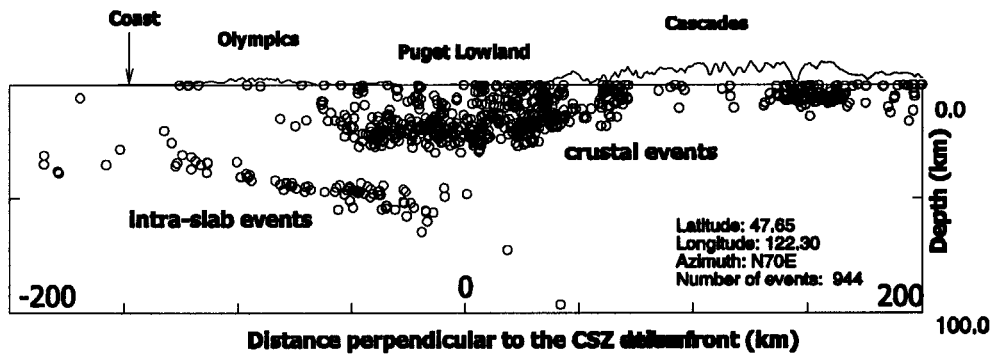


Figure 5.2: Depth distribution of earthquakes within a box which is 1° wide and 400 km long centered on Seattle and perpendicular to the deformation front. Total number of earthquakes shown is 944. 86 events between 30 and 100 km depth define the “Wadati-Benioff” zone and are presumed to take place near the top of the subducting JDF plate. The wiggly line on top of the plot represents a crude topography with 5:1 vertical to horizontal exaggeration. This figure is adopted from *Khazaradze* (1999)

Here μ is the shear modulus, d is the fault displacement, and A is the fault area. For continental crust, μ is approximately $3.3 \times 10^{10} \text{ Nm}^{-2}$ (e.g., *Brune*, 1968). Since we assume a model that varies linearly from completely locked to free slip across the width of the transition zone, and since we assume that both the locked and transition zones have the same widths, the average slip in a great earthquake is $\frac{3}{4} \times v_0 \times t$. v_0 is the convergence rate of the Juan de Fuca plate relative to the North America plate and t is the interseismic period t (500 years, e.g., *Atwater*, 1996). From this the average slip is about 15.8m. The fault area of the CSZ in our 3-D model is $1.14 \times 10^5 \text{ km}^2$, and the seismic moment is $5.9 \times 10^{22} \text{ Nm}$. If we use the empirical formula $M_w = (2 \times \log_{10} M_0) / 3 - 10.7$ given by *Kanamori* (1977), the maximum moment magnitude M_w for a great earthquake is 9.1. Even if only one tenth of the fault area ruptures, M_w is still greater than 8.0 which means the CSZ has a potential for a huge mega-thrust earthquake in the future.

The site velocities at most terrestrial GPS stations are theoretically affected by plate locking on the CSZ by amounts shown in Figure 5.3 (model shown in Figure 3.4). The maximum sensitivity

of CSZ model parameters to the site velocity field observed on the surface is 0.2mm/yr/km , produced by a depth change of the middle of the locked zone (control point B in Figure 3.9 and Figure 3.8). Changing the widths of the locked zone or the transition zone has a smaller effect than changing the depths of control points A, B, and C in figure 3.9. For sites far away from the trench, especially on the eastern side of the Cascades, the CSZ's contribution to crustal deformation is very small (Figure 5.3). To fit the magnitude of observed site velocities in the back-arc would increase the width of the seismogenic zone. But this would not produce the correct orientations of site velocity vectors and it would also cause site velocities at stations along coast to increase dramatically. Consequently, observed station velocities on the coast and east of the Cascades cannot be fit simultaneously with a simple dislocation model of plate locking.

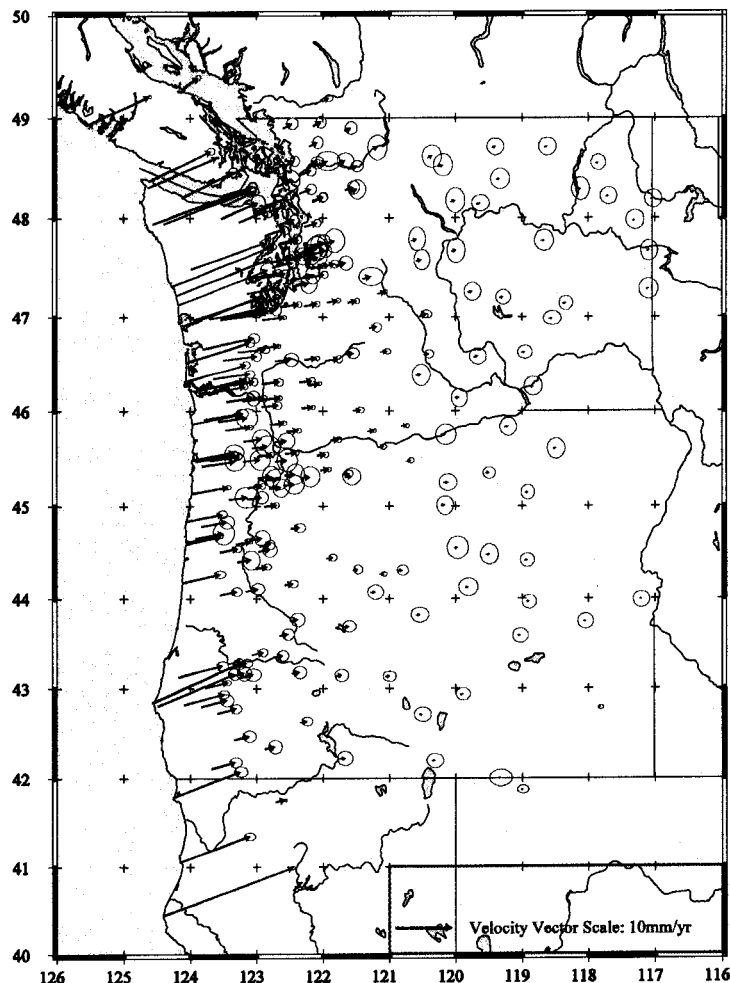


Figure 5.3 Predicted contribution of plate locking on the CSZ to site velocity at existing GPS sites. The ellipses are the uncertainties of the observed site velocity at each GPS station, not the uncertainty of the theoretical site velocity from the modeling. Sites with uncertainty larger than 3.0mm/yr are not shown.

A measure of the fit of the 3-D model to the observed site velocity is estimated from the variance σ^2 given in equation (3.20). The final model of Washington in Chapter 3 that includes plate locking, rigid-block rotation and north-south compression produces $\sigma^2 = 4.0 \text{ (mm/yr)}^2$ ($\sigma \sim 2.0 \text{ mm/yr}$) (Chapter 3). If we constrain the control points A, B, and C in Figure 3.8 to move freely only along the initial curve defining the top of the subducting plate, we can estimate the changes to σ^2 caused by physically reasonable changes in the widths of the locked and transition zones. The maximum contribution to σ^2 is about 23 (mm/yr)^2 caused by a 75km variation in the position of the downdip end of the locked zone. The F-test shows that the uncertainty of the horizontal position is about 58km for control point A, 25km for control point B, and 30km for control point C (Figure 3.12). This indicates that a 25km variation in the width of the transition zone and a 30km variation in the width of the locked zone are possible given current GPS observations. In principle, GPS observations of vertical velocity could further constrain the seismogenic zone.

Figure 5.4 shows that there are few stations directly over the transition zone along the Washington coast. This makes modeling of the subduction geometry more difficult. There are several ways to solve this problem. The first is to increase the number of GPS sites in the Olympic Peninsula which is located right above the transition zone. Deploying more GPS sites there would help us understand the mechanism that gives rise to the Olympic Mountains, and would provide information about the uplift rate (from future observation of v_z), which will further help us constrain the geometry of the CSZ (Flück *et al.*, 1997).

Currently the forward 3-D elastic model of plate locking assumes that the transition zone changes linearly from completely locked at its upper end to free slipping at its lower end. This assumption causes the surface velocity to decay rapidly to the northeast, so that it is hard to adjust the CSZ's geometry to find a "best-fit" model. Wang *et al.* (2003) modified this assumption in their "revised" 3-D elastic model. They assumed an exponential rather than a linear function from 100% locked to free slip, and called the newly defined transition zone an "effective transition zone" (ETZ). They found that a wider ETZ (two times as wide as the original transition zone) can fit the observed site velocity field better.

Figure 5.4 shows that residuals after removing the influence of the CSZ from the site velocities are large. The motion is about 11 – 30 mm/yr WNW in the southernmost fore-arc, and 4 – 8mm/yr N in the northernmost fore-arc. Thus plate coupling alone cannot explain the observations. Figure 5.4 also shows a clear image of clockwise rotation. In the following sections, I will discuss other possible mechanisms that contribute to the observed deformation in the Pacific Northwest, including block rotation.

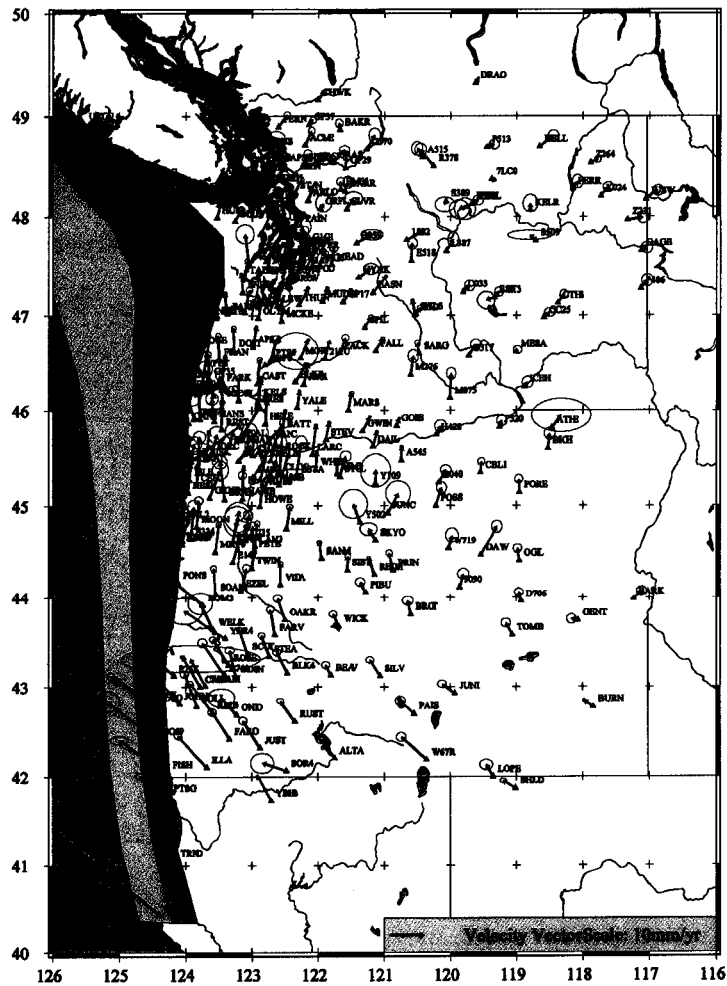


Figure 5.4 Residuals after removing contributions of CSZ plate locking from the observed site velocity field in the Pacific Northwest. Ellipses show uncertainties of site velocities. The velocity field that is left must be explained by block rotation and internal deformation from other physical mechanisms.

§5.2 Rigid-block rotation in Oregon

McCaffrey *et al.* (2000) used GPS data mainly from Oregon to show that plate locking and

rigid-block rotation are sufficient to explain crustal deformation in Oregon. Their best-fit pole for the western Oregon block is located at $45.9^\circ \pm 0.6^\circ\text{N}$, $118.7^\circ \pm 0.7^\circ\text{W}$, near the eastern Oregon/Washington boundary, and has a clockwise rotation rate of $-1.05^\circ \pm 0.16^\circ/\text{Ma}$. This rotation pole is close to the pole from paleomagnetic evidence (*Wells et al.*, 1998), but far from the pole inferred from GPS data in southern Oregon and northern California by *Savage et al.* (2000), which is at $43.4^\circ \pm 0.1^\circ\text{N}$, $120.0^\circ \pm 0.4^\circ\text{W}$ with a rotation rate of $-1.67^\circ \pm 0.17^\circ (\text{ma})^{-1}$. *Svarc et al.* (2002) obtained a clockwise rotation pole at $43.40^\circ \pm 0.14^\circ\text{N}$, $119.33^\circ \pm 0.28^\circ\text{W}$ with a rotation rate of $-0.822^\circ \pm 0.057^\circ (\text{Ma})^{-1}$, very close to the pole in *Savage's* results, by using 75 GPS monuments in western Oregon and southern Washington. *Wells and Simpson* (2001) used paleomagnetic evidence to show that western Oregon has rotated at a constant rate of $-1.19^\circ \pm 0.10^\circ (\text{Ma})^{-1}$ with a pole location close to *McCaffrey's* when averaged over the last 10 – 60 Ma. Based on more than 110 GPS sites, our preferred model shows that the Oregon forearc rotates $-0.90 \pm 0.03^\circ (\text{Ma})^{-1}$ (or -15.7 ± 0.5 nanoradians/yr) with a pole at $44.80 \pm 0.06^\circ\text{N}$, $116.82 \pm 0.18^\circ\text{W}$. This rotation rate is close to paleomagnetically determined rotation rates of basalt flows along the Columbia River between Oregon and Washington (*Hagstrum et al.*, 1999) and to the rotation rate of $-0.82^\circ \pm 0.06^\circ$ given by *Svarc et al.* (2002). It also fits the rate estimated from a kinematic model for western Oregon rotation given by *Wells et al.* (1998). The average rotation rate from paleomagnetic data 225 km away from the trench is -18 ± 2 nanoradians/yr for 15 Ma flows (*England and Wells*, 1991).

Our rotation pole is different from *McCaffrey's* (2000) because we used different models for the CSZ. Also, their model does not include regional strain, although inclusion of this parameter in Oregon does not affect the rotation rate very much. In our model, the geometry of the CSZ consists of two parts: a fully locked zone and a transition zone that changes linearly from fully locked to unlocked. Their model deals with partial locking differently (ϕ parameter in their model). Our data are from more than 140 GPS sites that cover most Oregon, while *McCaffrey's* (2000) rotation pole is derived from data in central and northern Oregon with only 71 GPS sites. *Savage et al.* (2000) used a conventional 2D model for the CSZ and a limited number of GPS sites from Cape Blanco on the Oregon coast to the volcanic arc near Newberry Crater. *Svarc et al.* (2002) also used a conventional 2D CSZ model and a somewhat larger number of stations but

their data set still does not cover the area from southern Washington to northern California. Generally, the rotation pole given by *McCaffrey et al. (2000)* fits the observations in northern Oregon. The pole estimated by *Savage et al. (2000)* fits the observations in southern Oregon. Our data cover all of Oregon and our estimated pole fits observations there. Thus, the differences of the CSZ model and GPS dataset cause the differences in the rotation poles for western Oregon rotation. One should remember that the rotation estimates from GPS observations reflect only a short-term motion, unlike paleomagnetic data which reflect long-term motion over millions of years. It is remarkable that rotation rates from paleomagnetic data and modern GPS observations agree so well.

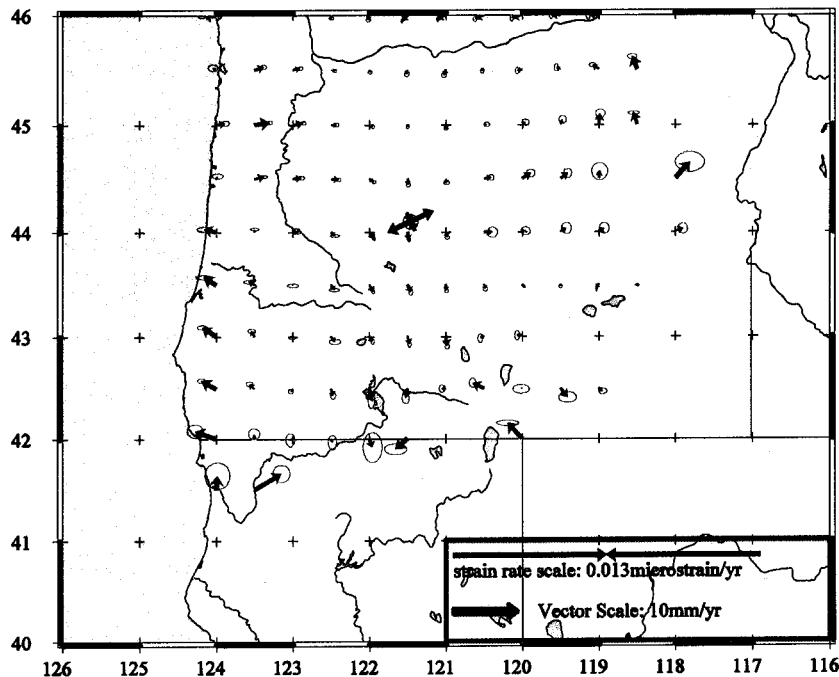


Figure 5.5 Site velocity residuals in Oregon. Red vectors are residuals after subtracting contributions from plate coupling and rigid block rotation. The blue arrows are the principal strain rates by assuming regional strain is uniform.

Plate coupling and rigid block rotation dominate crustal deformation in Oregon, and any residual strain is very small. If we assume that residual strain is uniform in Oregon, the principal residual strain rates $\dot{\epsilon}_1$ and $\dot{\epsilon}_2$ are 0.25 ± 0.07 and -0.09 ± 0.07 $\text{mm}(\text{yr})^{-1}(\text{km})^{-1}$ (2.3 ± 0.6 and -0.8 ± 0.6 nanostrain/yr, extension reckoned positive) respectively with an azimuth of the minimum principal axis of 155.4° . The minimum principal residual strain rate is only 6% of the residual

strain rates computed for western Washington. This indicates that Oregon undergoes a small amount of southwest – northeast extension (regional strain rate shown in Figure 5.5) which might be caused by magma circulation below the Cascades produced by the descending JDF lithosphere (Taylor, 1989). In general, the regional strain in the Oregon fore-arc is not significant, compared to regional strain rates in western Washington.

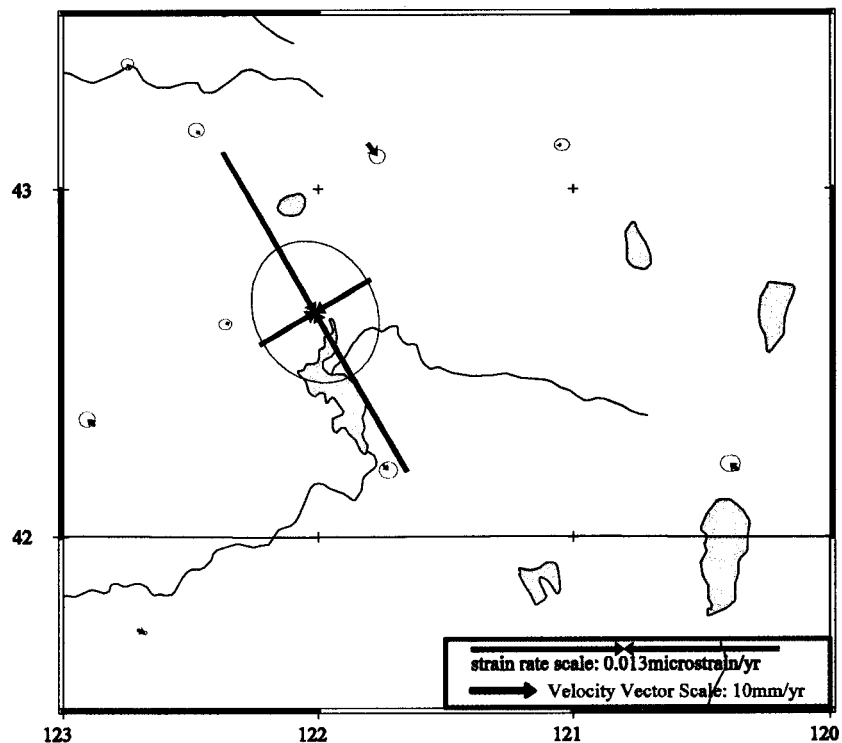


Figure 5.6 Residual strain rate in the vicinity of the Klamath mountains. Red vectors are final residuals after subtracting CSZ plate coupling, Oregon rigid block rotation, and regional strain from observed site velocities estimated at sites in this figure. Site velocities with a 3.00mm/yr uncertainty do not participate in the estimation.

The Klamath graben is located at the junction of northwestern Basin and Range, northern California, and southern Oregon. It is in the Cascade arc – Basin and Range transition zone, and bounded on the north by the Crater Lake caldera and on the west by the west Klamath Lake fault zone, formed by north to northwest trending, east-facing normal faults (Hawkins *et al.*, 1989; Bacon *et al.*, 1999). Very few earthquakes were known in this region before two M 6.0 earthquakes occurred on Sept. 20, 1993, followed by thousands of aftershocks (Sherrod, 1993; Braunmiller *et al.*, 1995). Using an empirical relation between earthquake magnitude and surface rupture length for normal fault or earthquake magnitude and downdip rupture area, Bacon *et al.* (1999) estimated that this area may have earthquakes of M6 to M7.2. We have used several GPS

sites to estimate the local strain accumulation in the Klamath graben. The result shown in Figure 5.6 is dominated by northwest-southeast compression with a magnitude of roughly 0.013 microstrain/yr. The computed strain field from the GPS data is not consistent with the normal faulting observed from the geology of the Basin and Range.

In southwestern Oregon and northwestern California, the model does not fit the GPS data well. This region is tectonically complex. The Mendocino transform is located to the west. The Eastern California shear zone and the San Andreas fault system such as the Ma'acama and Barlett Springs faults lie to the southeast. The Basin and Range province is to the east. The interactions of all of these are expected to contribute to the observed crustal site velocity. In general, such a complicated system cannot be modeling by a simple elastic dislocation model in a half space.

§5.4 Kinematics in Washington

§5.4.1 Introduction

The previous sections show that CSZ plate locking and block rotation are the two major mechanisms driving surface motion in Oregon. In Chapter 4, we already showed that Washington cannot be modeled as one block. Based on geologic, seismic, volcanic, and paleomagnetic evidence, Washington has been divided into five sub-blocks. In the following sections, I discuss the kinematics of these sub-blocks.

§5.4.2 Rigid body rotation in Washington

There are two ways to estimate rigid block rotation parameters. The first method is to determine the age and directions of remnant magnetization of rocks laid down in the past few millions of years. This gives a long term average rotation. The second method is to geodetically determine the current rotation for individual regions, using GPS data. This gives a short term average rotation over a few years. Paleomagnetic measurements in rocks of the forearc, arc, and back-arc blocks of the CSZ indicate clockwise rotations in Cenozoic (<62 Ma) rocks. These paleomagnetically estimated rotations have the following two characteristics (*Magill et al.*, 1982; *Beck et al.*, 1986; *Wells*, 1990; *England and Wells*, 1991; *Hagstrum et al.*, 1999):

- The youngest paleomagnetic rotations estimated from Columbia River basalts of Miocene age (12-15 Ma) exhibit a rotation that decreases from west to east: from $\sim 30^\circ$ along the coast to $\sim 6^\circ$ 300 km away from the CSZ trench (*England and Wells, 1991*). This is equivalent to rotation rates of ~ 2.2 and $\sim 0.4^\circ/\text{Ma}$, respectively.
- Rotation rates decrease from South to North. A maximum total rotation of 80° is found in the Paleocene (~ 60 Ma) rocks of southwest Oregon, equivalent to a rotation rate of $\sim 1.5^\circ/\text{Ma}$ (*Wells, 1990*).

I compare rotation rates estimated from paleomagnetism and geodesy in Table 5.1 and Table 5.2. The Oregon block, Mt. Rainier block, and Puget Sound block can be used to check the relationship between rotation rate and latitude. The Oregon block, Mt. Rainier block, and Yakima block can be used to test the dependence of rotation rate on longitude. Table 5.2 mostly confirms the observation that geodetically estimated rotation rates decrease from west to east and from south to north, in agreement with paleomagnetism. Our current estimated rotation rate for the Oregon block is $-0.9 \pm 0.03^\circ/\text{Ma}$. The long term Neogene rotation rate is $-2.2 \pm 1.8^\circ/\text{Ma}$ estimated by *England and Wells (1991)*. The match is also reasonable further inland. The rotation rate estimated from GPS data for the Mt. Rainier block is $-0.66 \pm 0.16^\circ/\text{Ma}$ and the Neogene deformation rate estimated approximately 300 km away from the deformation front is $\sim -0.4 \pm 1.5^\circ/\text{Ma}$. *Hagstrum et al. (1999)* used paleomagnetic data from a transect across the Cascadia arc in southwestern Washington and grouped them into three sets. Set I showed $34^\circ \pm 13^\circ$ clockwise rotation between 39 and 30 Ma. Set II showed $17^\circ \pm 11^\circ$ clockwise rotation between 30 and 24 Ma. Set III showed $20^\circ \pm 12^\circ$ clockwise rotation between 24 and 16 Ma.

Table 5.1 Variation of paleomagnetically determined rotation rates

Direction	Rotation rate($^\circ/\text{Ma}$)	Uncertainty($^\circ/\text{Ma}$)	Reference*
West \rightarrow East	-2.2 \rightarrow -0.4	1.8	1,2
South \rightarrow North	-1.5 \rightarrow 0.0	1.5	1,3

*: (1) *Magill et al. (1982)*; (2) *England and Wells (1991)*; (3) *Wells (1990)*.

I have converted the rotations to average rates in Table 5.3. Our estimated rates for the Oregon block ($-0.9^\circ/\text{Ma}$) and the Mt. Rainier block ($-0.66^\circ/\text{Ma}$) match paleomagnetic results reasonably well. From west to east our estimated rotation rate changes from $-0.9^\circ/\text{Ma}$ in the

western Oregon block to -0.66 °/Ma in the Mt. Rainier block, and finally to -0.16 °/Ma in the Yakima block, a rate which decreases to the east. From south to north, the geodetically determined clockwise rotation rate changes from -0.9 °/Ma in Oregon to -0.66 °/Ma in the Mt. Rainier block, and finally to -0.08 °/Ma in the Puget Sound block, also clearly demonstrating a trend of decreasing rotation rate with latitude. However, from the coast block to the Mt. Rainier

Table 5.2 Estimated rotation rates for all blocks in the Pacific Northwest from GPS data³

	Coast Block (A ¹)	The Puget Sound Block (B ¹)	Yakima Block (D ¹)
Block Name	-0.32±0.19	-0.08±0.11	-0.16±0.11
Rotation Rate ± uncertainty ² (°/Ma)		Mt. Rainier Block (C ¹)	
		-0.66±0.16	

¹: For the definitions of these blocks, please refer to table 4.1

²: '+' means counter-clockwise rotation, '-' means clockwise rotation.

³: Shaded areas are small blocks. Each shaded area has two lines. The first line is the name of the block. The second line is the estimated rotation rate in that block

block and from the Yakima block to the northeast block, one sees an opposite trend. The discrepancy for the coast block might be caused by over-estimating the widths or under-estimating the depths of the Cascadia subduction zone. These errors would produce larger westward residual components. The discrepancy in the northeast block may be due to insufficient and inaccurate GPS data there. Of course the paleomagnetically determined rotation rate is a long-term average rate, while the geodetically estimated clockwise rotation rate is an instantaneous rate, so the two rates cannot be necessarily expected to agree.

Table 5.3 Paleomagnetically determined rotation rates in southwestern Washington (Hagstrum et al., 1999)

Set name	Rotation rate(°/Ma)*	Time (Ma)
Set I	-1.0	39 ~ 30
Set II	-0.6	30 ~ 24
Set III	-1.0	24 ~ 16

*: Minus sign means clockwise rotation

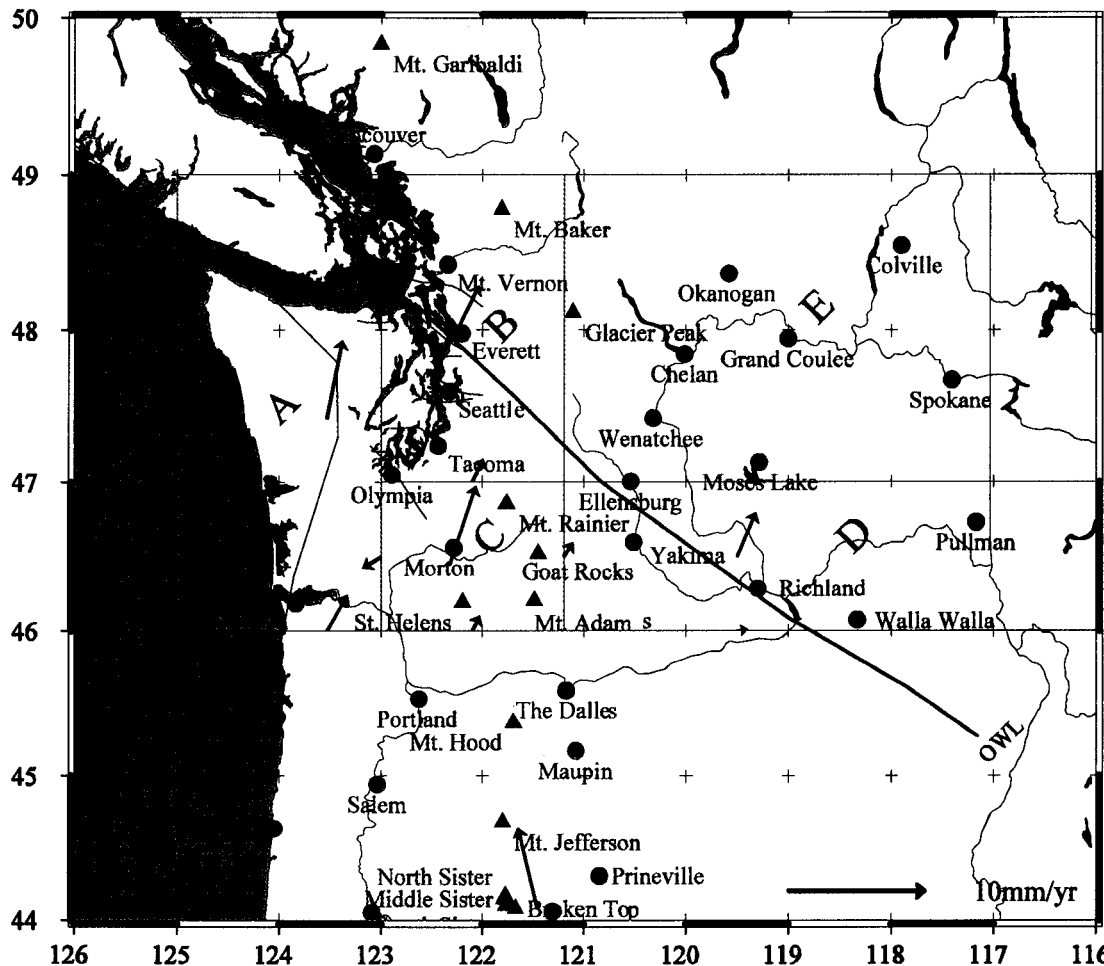


Figure 5.7 Relative motion on boundaries between sub-blocks. Black arrows in middle of blocks are motions caused by block rotations. Black velocities on horizontal boundaries are motions of lower blocks relative to upper blocks, and on vertical boundaries they are motions of left blocks relative to right blocks. Green lines are boundaries of sub-blocks. The long red line is the OWL (Raisz, 1945). The thin blue lines are faults. The offshore lines on the left show boundaries of locked and transition zones for the CSZ.

In general, the GPS rotation rates match remarkably well with paleomagnetically determined rotation rates. In Washington, all blocks rotate clockwise according to the GPS data, and the rotation rates decrease from west to east and from south to north. In northern Washington, close to British Columbia, rotation is quite small. The rotation in northeastern Washington and the back-arc is still very uncertain because we lack well-constrained site velocities there. The poles and rotation rates of all blocks are given Table 4.2. The possible driving forces for these rotations are: 1) dextral shear along the coast due to the PA/NA plate interaction (e.g. *Pezzopane and Weldon, 1993*); 2) the tangential component of JDF/NA oblique subduction (e.g. *Beck, 1993; Wang, 1995*). Both of these forces would contribute to margin-parallel translation of the forearc; 3)

intra-continental extension in the Basin and Range (Figure 5.3), causing clockwise rotation in the forearc of the CSZ (e.g. *Walcott, 1993; Wells et al., 1998*).

The computed block rotations in the Pacific Northwest would generate relative motions between sub-blocks (Figure 5.7). The Oregon block pushes northward on the Washington coast block (A) and Mt. Rainier block (C). The Washington coast (A) moves faster to the north than the Puget Sound (B) and produces northwest relative motion between the two blocks, in agreement with evidence of strike-slip (right-lateral) offset shown on the 6 to 7 km wide South Whidbey Island fault zone (Figure 1.12) (*Johnson et al., 1996*). The Mt. Rainier block (C) pushes to the northeast on the Puget Sound block (B) and generates N-S compression in the Puget-Georgia basin. The northeastward motion of the Mt. Rainier block relative to the Yakima block may contribute to the formation of a compressive arc in Washington (*Weaver et al., 1983, 1985; Rogers, 1985*).

In Chapter 4, we showed that after subtracting contributions from CSZ plate locking and rigid block rotation, there is still an unmodeled component of the velocity field which may reflect regional strain accumulation. In the next section, I discuss such strains, together with other geological and seismological data.

§5.4.3 Residual strain analysis in Washington

In Chapter 4, we computed maximum and minimum principal residual strain rates in all modeled blocks in Washington. These are summarized in tables 5.4. and 5.5. The bottom of both tables corresponds to south, top to north, right side to east, left side to west. Rotation rates decreases from south to north, but most of central west Washington shows a uniform N-S residual strain rate of about $0.013\mu\text{strain/yr}$. Remarkably, a similar N-S residual strain rate is seen east of the Cascades in the Yakima block. These minimum principal residual strain rates exhibit a slight change in rate from south to north and from west to east. The total N-S contraction is about 4.7 mm/yr across the Puget Sound – Mt. St. Helens corridor, about 5.7mm/yr across the coast block, and about 1mm/yr across the Yakima block. This Washington fore-arc “residual compression” agrees well with the north-south shortening predicted by the kinematic model of the Cascadia

Table 5.4 The minimum principal residual strain rates ϵ_2 estimated regionally for all blocks in Washington GPS data³

Block Name		³ Puget Sound Block (B ¹)	
Regional strain Rate \pm error ² (μ strain/yr)		-0.013 \pm 0.001	
	Azimuth($^\circ$)	25.06	
		³ Mt. Rainier Block (C)	³ Yakima Block (D ¹)
		-0.015 \pm 0.001	-0.010 \pm 0.004
			6.26

¹: For the definitions of these block, please refer to table 4.1

²: '+' means expansion, '-' means compression.

³: Shaded areas are small blocks. Each shaded area has two cells. The first cell is the name of the block. The second cell is the minimum principal strain rate and its error as well as the azimuth to the ϵ_2 axis

Table 5.5 The maximum principal residual strain rates ϵ_1 estimated regionally for all blocks in Washington GPS data³

Block Name		Puget Sound Block (B ¹)	
Regional strain Rate \pm error ² (μ strain/yr)		-0.001 \pm 0.001	
		³ Mt. Rainier Block (C)	³ Yakima Block (D ¹)
		0.002 \pm 0.001	0.003 \pm 0.001

¹: For the definitions of these block, please refer to table 4.1

²: '+' means expansion, '-' means compression.

³: Shade areas are small blocks. Each shade area has two cells. The first cell is the name of that block. The second cell is the maximum principal strain rate and its error

forearc blocks proposed by *Wells et al.* (1998) (Figure 1.3). According to this model, the Washington block (shown as a green shaded area) is characterized by the presence of several broken sub-blocks squeezed against the Canadian Coast Mountains to the north. This squeezing is most likely due to the northward translation of the central Oregon block (shown as a pink shaded area in Figure 1.3) driven by Pacific-North America dextral shear that dominates tectonics in California (*Pezzopane and Weldon, 1993; Wells et al., 1998*) and/or by the margin-parallel translation of the forearc segments driven by oblique subduction across the CSZ (*McCaffrey,*

1992; Wang, 1996).

Seismicity in the Mt. St. Helens and Rainier block is grouped into two narrow NW-SE clusters (Figure 5.8). One is located to the north of Mt. St. Helens and called the St. Helens seismic Zone (SHZ) (Weaver and Smith, 1983; Grant *et al.*, 1984). The other is roughly 15km west of Mt. Rainier and called the western Rainier seismic zone (WRSZ) (Thompson and Qamar, 1989; Malone *et al.*, 1991). Our residual strain rate estimation in this area is $-0.015 \pm 0.001 \mu\text{strain}/\text{yr}$ oriented $N31.54^\circ\text{E}$. Fault plane solutions show that most earthquakes occurred in the Mt. St. Helens and Mt. Rainier area from 1970 to present are associated with NE-SW direction of maximum principal stress, consistent with the direction of compressional residual strain rate (Figure 5.9).

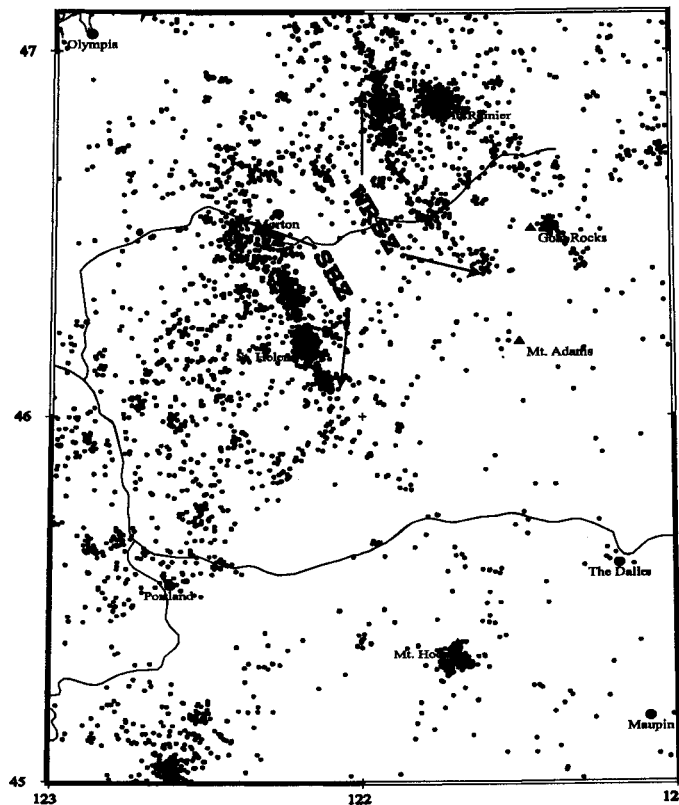


Figure 5.8 Map showing locations of earthquakes whose magnitude is bigger than 1.0 within block C from 1969 to 2002.

The crustal seismicity continues northward to Puget-Sound. Due to heavy vegetation, thick Quaternary glacial deposits, and alluvium, seismicity here has not been generally correlated with

specific faults visible at the surface, except in some instances such as the E-W trending Seattle fault. Our model shows a N-S contraction at a strain rate of $0.013 \pm 0.001 \mu\text{strain/yr}$ in the direction $N25^\circ E$ in block B. Over the whole Puget Sound, the estimated shortening rate is 3mm/yr , consistent with *Hyndman et al. (2003)*. The geologically determined north – south contraction rate accommodated by all the faults in this area is roughly $3 - 6 \text{ mm/yr}$ (*Wells and Simpson, 2001*), in approximate agreement with the GPS estimates. Focal mechanisms (e.g. *Crosson, 1972; Wang et al., 1995; Ma et al., 1996*) and geologic data (*Johnson et al., 1994; Pratt et al., 1997; Johnson et al., 1999*) also suggest that crustal seismicity in Puget Sound reflects N-S contraction. East-west or northwest trending reverse faults in this region accommodate this compression. The largest active fault so far mapped in this region is the Seattle fault. If we assume that the fault is 7km wide and 110km long (Figure 1.12), and that all accumulated strain energy is released by this fault in one earthquake, and that such earthquakes have a recurrence

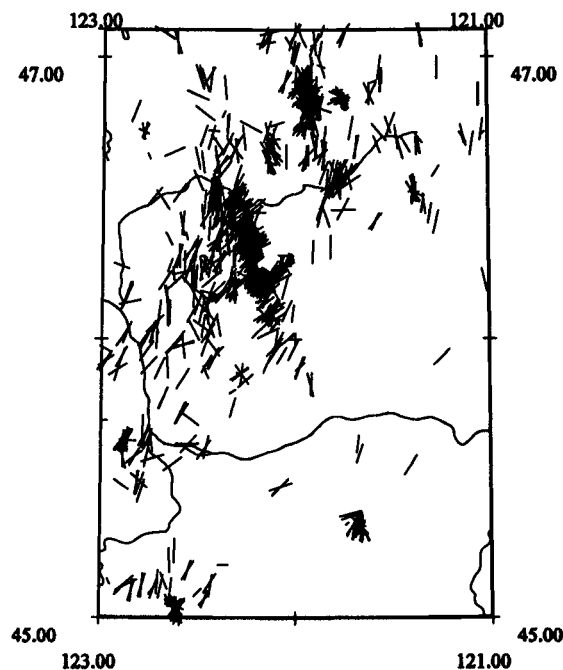


Figure 5.9 Horizontal projection of the maximum principal stress axis of earthquakes in block C from 1970 to 2003.

time of 1000 years, then the area of rupture is about $770(\text{km})^2$ and the average slip is 2.9m per event. Using equation 5.1 and $3.3 \times 10^{10} \text{ Nm}^{-2}$ for the shear modulus μ (e.g., *Brune, 1968*), we estimate the seismic moment M_0 will be $7.4 \times 10^{19} \text{ N}\cdot\text{m}$. Using $M_w = 2/3 \log_{10}^{M_0} - 10.7$ given by

Kanamori (1977), the moment magnitude M_w is about 7.2. Alternatively if we use the relation $\log A = -4.07 + M$ from *Wells and Coppersmith* (1994), the magnitude M is also about 7. The most recent such event occurred about 1000 years ago (e.g., *Johnson et al.*, 1999). *Hyndman et al.* (2003) used earthquake catalog statistics to predict that the recurrence times are 45 years for $M > 6$ and 400 years for $M > 7$ (Figure 5.10). If we use their method (Figure 5.10) but consider the size of our Puget Sound block, the recurrence for $M > 7$ is about 770 years. *Hyndman et al.* counted the number of earthquakes vs. depth, and concluded that the depth of maximum seismicity for the western part of this region is about 20km and for the eastern part about 10km (*Hyndman et al.*, 2003) (Figure 5.11). So the effective depth for the west part is about 18km and is 6km for the east

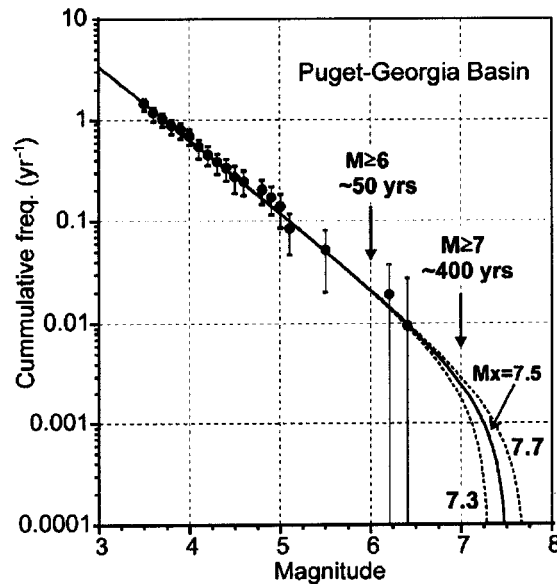


Figure 5.10. Earthquake magnitude versus cumulative frequency of occurrence for crustal events in the Puget Sound – S. Georgia Strait region using the method of Weichert (1980). The error estimates assume the statistics are Poissonian. The figure is extracted from *Hyndman et al.* (2003).

part (% of earthquakes times depth/total percent). So for the whole Puget sound, the effective depth of crustal earthquakes is about 12km. The overall seismic slip rate in a broadly converging region can be estimated (*Kostrov*, 1974) by a simple formula:

$$s = CM'_o / (2\mu A') \quad (5.2)$$

Where C is a constant and depends on the orientation of the faulting with respect to the regional

motion, A' is an effective cross-sectional area of the converging zone perpendicular to the shortening direction, M_o' is the seismic moment per unit time (Nm/yr). If the fault dip angle is 45° , $C = 1.0$. For the Seattle fault, the angle has been estimated variously between $25-30^\circ$ and $55 - 65^\circ$ (Brocher *et al.*, 2001; Pratt *et al.*, 1997). Here we make $C=1$. Then, the seismic slip rate can be calculated by

$$s = M_o' / (2\mu A') \quad (5.3)$$

If we assume the Seattle fault is 110km long (Figure 1.12), and the effective depth of the crustal seismicity is 12km, the seismic moment rate of a maximum M7.5 earthquake in the Puget sound is 2.4×10^{17} Nm/yr (Hyndman *et al.*, 2003), and the seismic slip rate is 2.8mm/yr, matching our geodetically estimated slip rate fairly well.

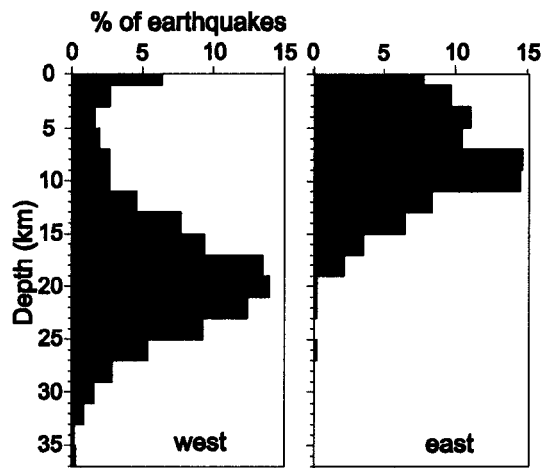


Figure 5.11 Number of earthquakes (1985 – 2001) as a function of depth for the Puget – Georgia basin small study region, similar to our block B. Extracted from Hyndman *et al.*, 2003

Unlike Puget Sound, the Olympic Peninsula has few earthquakes. The core rocks of the Olympics have been locally exposed and uplifted since ~ 18 million years ago (Tabor *et al.*, 1978). GPS observations show that this region has the largest north-south strain rate about -0.017 ± 0.001 $\mu\text{strain/yr}$. Geologically, Magee and Zoback (1992) found that this region south of the Copalis River is undergoing shortening with a $N14^\circ E$ principal compressive stress, and south of Joe Creek is undergoing a $N5^\circ W$ directed contraction. Young marine strata off the Washington coast also show evidence of north-south oriented folding and faulting (McCrorry, 1996). This N-S

compression might also contribute to the uplift of the Olympic Mountains (e.g., *Walcott, 1993*). At the same time, the GPS data show that this region also has the largest east-west extension rate ($0.019\mu\text{strain/yr}$) after accounting for plate locking on the CSZ. This may indicate that the plate coupling on the CSZ in this region has been over-estimated.

The Olympic – Wallowa Lineament (OWL) goes through the Yakima fold and thrust belt in block D. The OWL consists a set of east – west trending anticlinal ridges and associated thrust faults and has several seismic zones (one is along the Idaho-Oregon border, another one is along Washington – Oregon border) (*Mann et al., 1993*). The GPS observations show that the Yakima block is shortening from north to south by about 1.1mm/yr. This may produce the E-W trending anticlines in the Yakima fold belt (*Malone et al., 1975*). The seismicity in much of this region has not been correlated to specific faults, but fault plane solutions show most earthquakes in this region are caused by N-S compression (Figure 5.12).

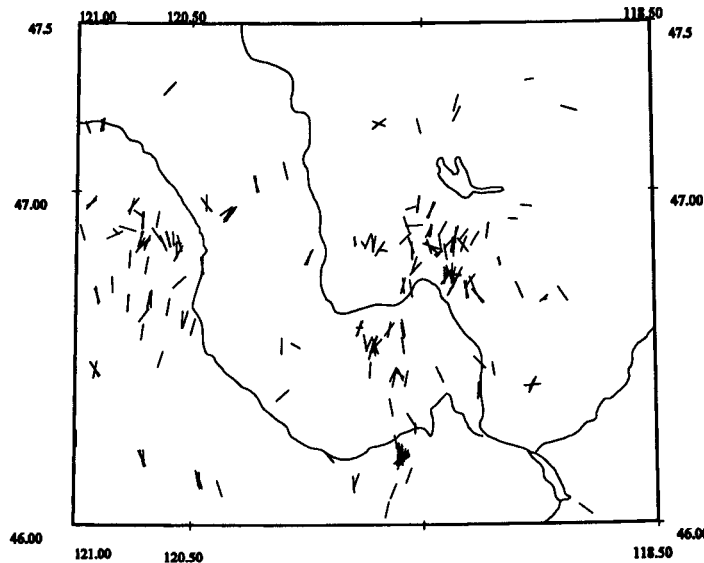


Figure 5.12 Horizontal projection of the maximum principal stress axis of earthquakes in the Yakima block from 1970 to 2003.

Most of the seismicity in northeastern Washington (block E) lies between Wenatchee and Chelan near the boundary of the north Cascades and Columbia Plateau geologic provinces, and near the northern edge of the Yakima fold belt. The biggest known earthquake in this region occurred on 15 Dec. 1872. It was probably a shallow earthquake near the south end of Lake Chelan with an “intensity magnitude” MI 6.8 (*Bakun et al., 2002*). This region is actively deforming, but the

recurrence time for such earthquakes is unknown. Focal mechanisms for earthquakes from 1970 to 2003 indicate a predominantly northwest – southeast direction of maximum principal stress on the west side of the Columbia River (a few earthquakes in the east side exhibit a northeast – southwest maximum stress direction (Figure 5.13)). GPS data in this region are probably not good enough yet to determine principal strain rate directions.

The Washington coastal block (A) has high strain rate and low short-term seismicity. Puget Sound (block B) and Mt. Rainier (block C) have high regional strain rates and high crustal seismicity. The Yakima (D) block has a lower strain rate and lower seismicity. The Oregon block has the lowest regional strain rate and is seismically quiet. Thus, crustal seismicity is usually greater when strain rates are high, but the coastal region, where the strain rate is high, is an exception. Of course this region is subject to megathrust earthquake every few hundred years.

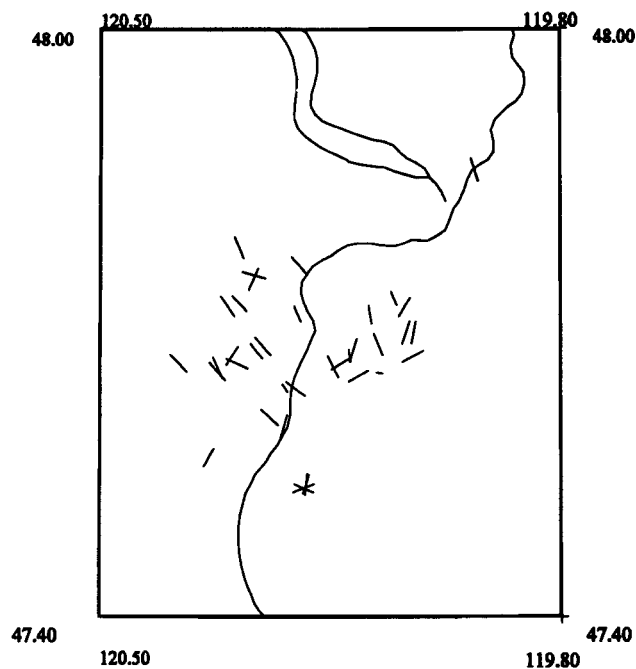


Figure 5.13. Orientations of P axes for the lake Chelan region determined by routine first-motion analysis for earthquakes from 1970 to 2003 recorded by the Pacific Northwest Seismograph Network (PNSN) of Univ. of Washington.

§5.5 Further discussion

We used tectonic, seismic, geologic, and heat-flow evidence to separate Washington into five

small blocks. Others propose that the Olympic – Willowa Lineament (OWL) (*Raisz, 1945*), a prominent topographic feature extending from northern edge of the Olympic Peninsula to northeastern of Oregon, serves as a major block boundary and that portion of Washington south of the OWL, and most of Oregon are in one rigid block. But so far GPS observations do not show any obvious changes across the OWL. As we have seen, other block boundaries are required to explain observed geodetic data, seismicity, etc.

§5.6 Postglacial rebound

Besides CSZ plate coupling, block rotation, and regional strain accumulation, another possible mechanism for surface deformation in the Pacific Northwest is postglacial rebound, especially in the northern part of the CSZ.

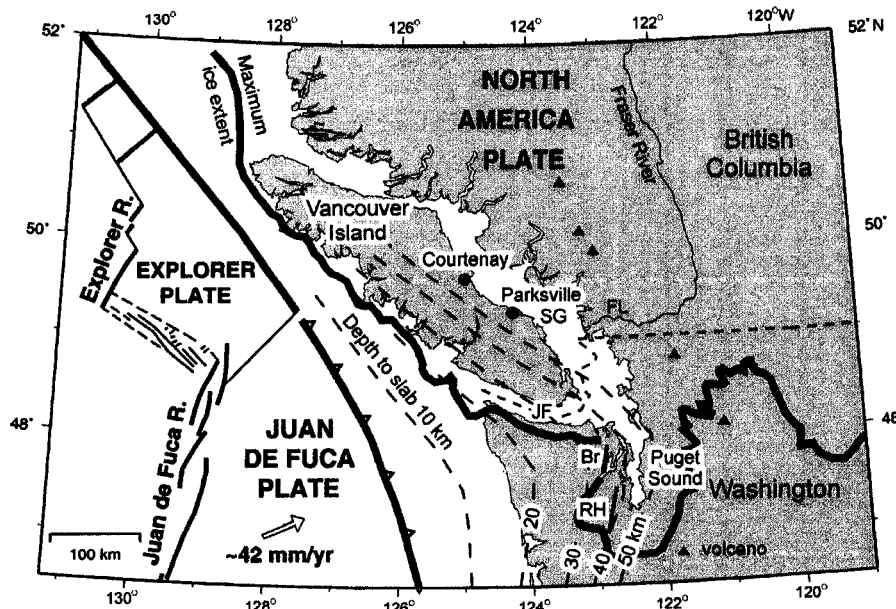


Figure 5.14. Tectonic setting of the northern Cascadia subduction zone, where the Juan de Fuca plate subducts beneath North America. Dashed lines show the depth to the top of the subducting plate (Fluck et al., 1997). Heavy line shows the maximum extent of the Cordilleran ice-sheet at about 14 ka (Clague, 1983). Location of profiles from which Puget Sound proglacial lake shoreline tilts were determined are designated RH (Lake Russell-Hood) and Br (western Lake Bretz). Relative sea level data locations are marked with filled circles. FL is Fraser Lowland, SG is Strait of Georgia, and JF is strait of Juan de Fuc. Adopted from *James et al.* (2000).

At its maximum extent, the Cordilleran ice-sheet once covered southwestern British Columbia and the Puget Sound in northwestern Washington State (Figure 5.14) and depressed this region. During deglaciation from 14 to about 10ka, northern NA experienced postglacial rebound which

depends on original ice thickness, deglaciation history, effective elastic lithosphere thickness, and the viscosity of the underlying mantle. According to two commonly used global rebound models, ICE-3G (Tushingham and Peltier, 1991) and ICE-4G (Peltier, 1994), the rebound process is still contributing to crustal deformation in the northern Cascadia forearc at rates comparable to that due to subduction earthquakes. ICE-3G and ICE-4G assumed a 120 km thick elastic lithosphere and a viscosity of 10^{21} Pa s for the upper mantle. However, based on a local rebound model constrained by shoreline tilts of pro-glacial lakes in Washington and relative sea level changes in southern British Columbia, James et al. (2000) claimed that appreciable land tilt due to rebound is negligible in this region at present, a result that was confirmed by Clague and James in 2002. Postglacial rebound influences primarily vertical uplift, and in this study we have used horizontal components of motion only, so we can ignore this effect.

Chapter 6: Conclusion

Nearly 300 GPS sites, including both permanent and campaign sites, are used in this geodetic study of Cascadia. Observed horizontal components of velocities are large at coastal sites and generally smaller to the east. The directions of the site velocity vectors are roughly normal to the continental margin in northern Washington and southern British Columbia, oblique (northeast directed) from southern Washington to northern Oregon, and parallel to the continental margin from central Oregon to northern California. Thus, from northern California to northern Washington, these GPS sites respond to plate locking on the Cascadia Subduction Zone but also display a clockwise “rotation” of the crust in Oregon and Washington. A simple rotation model works well in Oregon. A more complex model is required in Washington.

Modeling shows that contemporary crustal deformation rates at coastal sites are strongly influenced by the convergence of the Juan de Fuca and North America plates. The CSZ is accumulating elastic strain energy for a next megathrust earthquake (*Wang et al.*, 1995; *Fluck et al.*, 1997; *Khazaradze et al.*, 1999; *Wang et al.*, 2003). Inverse 3-D modeling in this study results in only small changes to the plate locking model of the CSZ given by *Fluck et al.* (1997).

In modeling plate locking we find that the influence of plate locking on the Cascadia subduction zone decreases rapidly to the east and the observed site velocity field is more sensitive to the depth of the lower end of the CSZ's locked zone than other model parameters. The uncertainty in the widths of the locked and transition zones is about 25km - 40km.

The GPS observations also show that plate locking alone cannot explain observed GPS velocities, and that the Pacific Northwest cannot be modeled as one rigid block. Based on seismicity as well as tectonic, and geologic evidence, we have divided the Pacific Northwest into six blocks. With this model, western Oregon rotates clockwise, consistent with previous studies (*Wells et al.*, 1984, 1990, 1998, 2001; *Savage et al.*, 2000; *McCaffrey et al.*, 2000). The clockwise rotation pole is at $116.82 \pm 0.18^\circ\text{W}$, $44.8 \pm 0.06^\circ\text{N}$ with a rotation rate of $-0.90 \pm 0.03^\circ/\text{Ma}$. The location of this pole is between *McCaffrey's* (2000) pole and *Savage's* (2000) pole and fits better the observed site

velocity field. The results also indicate that CSZ plate coupling and rigid block rotation are the two major mechanisms driving crustal deformation in Oregon, consistent with previous studies (e.g. *McCaffrey et al.*, 2000; *Svarc et al.*, 2002)

After subtracting contributions of the CSZ and block rotation from observed velocities, we found slight extension between western Oregon and eastern Oregon. Southwestern Oregon is tectonically complex (*Miller et al.*; 2001). Our model over-simplifies this region and does not fit GPS data well.

In Washington, the preferred model requires several sub-blocks. Clockwise rotation rates of sub-blocks decrease from south to north. The rate decreases from $0.90^\circ/\text{Ma}$ in Oregon to $0.08^\circ/\text{Ma}$ in the Puget Sound. Clockwise rotation also decreases from west to east with rates of $0.90^\circ/\text{Ma}$ in Oregon, $0.66^\circ/\text{Ma}$ in Mt. Rainier area, and $0.16^\circ/\text{Ma}$ in the Yakima area. These rates are consistent with long term rates determined from paleomagnetic studies (*Magill et al.*, 1982; *Beck et al.*, 1986; *Wells*, 1990; *England and Wells*, 1991; *Hagstrum et al.*, 1999). The clockwise rotation in western Oregon pushes on Washington to the northeast and generates N-S compression in the Washington forearc. The varying rotations in sub-blocks produce relative motion between blocks in this model that may explain compression in the arc in Washington.

Short-term strain accumulation from the Cascadia subduction zone in Washington dominates GPS observations at coastal stations. In addition, there is a long-term residual strain buildup further inland that is unrelated to subduction. This long-term residual strain is also detectable from the GPS observations. From south to north, the residual strain rate increases from less than $-0.001\mu\text{strain}/\text{yr}$ in Oregon to $-0.013\mu\text{strain}/\text{yr}$ in the Puget Sound. From west to east in Washington, the residual strain rate decreases from $0.017\mu\text{strain}/\text{yr}$ in the Olympic Peninsula to $-0.010\mu\text{strain}/\text{yr}$ in the Yakima block.

The residual strain in the Olympic Peninsula does not currently produce a high rate of crustal seismicity, but probably contributes to aseismic deformation that produces uplift in the core of the Olympics. Crustal seismicity in other blocks appears to be proportional to the residual strain

accumulation rate. For example seismicity in Puget Sound is high where N-S residual strain rate is relatively high. This relationship between residual strain rate and crustal earthquakes seems to explain why Oregon has much less seismicity than Washington.

Except in the northeast Washington block, where GPS site velocities are still uncertain, other blocks in Washington show generally north – south compression with different residual strain rates. This compression is consistent with the principal stress directions derived from earthquake focal mechanism solutions. The residual strain rate along the Washington coast (block A) is equivalent to 6mm/yr of N-S shortening across the block. In Puget Sound (block B), the shortening is about 3mm/yr, in the Mt. Rainier area (block C) the shortening is 2mm/yr, and in the Yakima area it is about 1mm/yr, in agreement with previous studies (e.g. *Wells et al.*, 1998; *Miller et al.*, 2001; *Hyndman et al.*, 2003).

In the Puget Lowland, CSZ plate coupling and N-S shortening are the two major mechanisms driving crustal deformation. Rigid block rotation in this region is negligible. The N-S contraction probably controls current seismicity in the crust, and is sufficient to produce M7.0+ earthquakes in the future, for example on the Seattle fault. The geodetically estimated regional strain rate is in agreement with the seismic strain rate derived from historical earthquakes.

The Oregon block has the highest clockwise rotation rate and the lowest regional strain rate. The Mt. Rainier block has an intermediate rotation rate and regional strain rate. The Puget Sound has a negligible clockwise rotation rate and a high N-S shortening rate. This suggests that southern Washington acts as a transition zone between Oregon and the rest of Washington. This zone transforms the rigid block rotation in Oregon into N-S compression in western Washington.

The Cascadia arc tectonically separates the Pacific Northwest into two parts: the fore-arc and the back-arc. From geologic evidence, the arc in Oregon is extensional, whereas in Washington it is compressive. This has obvious implications for GPS site velocities. For example, one might expect block rotation in western Oregon and Washington to not be transmitted across the arc. However, current GPS observations suggest such rotation does transfer across the arc.

Future work

From the observed site velocity field, one can see that the back-arc currently has very poor data coverage, but this region holds the key to what happens to the rotation induced by western Oregon. Although we have surveyed some NGS monuments in northeastern Washington, and we added new benchmarks in 2001, we need more measurements at these sites to improve the precision of the site velocities. The Olympic Peninsula is also of great interest because it is the only region on land right above the transition zone of the CSZ. We should take advantage of this region in order to monitor the uplift of the Olympic Mountains and to constrain the geometry of the CSZ. Ideally, one should have stations across the boundary of the locked and transition zones to provide the best constraints on models but such places are offshore! Some GPS sites in the Pacific Northwest have large uncertainties and abnormal site velocities compared with sites nearby. These may have unstable monuments or just need more occupations.

In current modeling, only horizontal components of site velocities are used. However, in many cases the models are not very sensitive to these components. If vertical components of site velocities could be used, depths of the locked and transition zones of the CSZ could be better constrained (Figure 6.1). The sensitivity of the vertical velocity to slab depth is up to 0.5mm/a/km, which is twice as much as the sensitivity of horizontal velocity to slab depth. The sensitivity of velocity to slab depth decays with distance from the trench but measurements of vertical velocity might improve constraints on the geometry of the CSZ (Figure 6.1, Figure 3.9).

Currently vertical components of site velocities from GPS data have large uncertainties. We may have to use other survey techniques like leveling or gravity surveys to obtain vertical components with higher accuracy.

In our preferred model, we assumed a fully locked zone plus a transition zone varying linearly from 100% locked to 0% locked. *Wang et al.* (2003) used an exponential relationship in their “revised” 3-D elastic dislocation model in a half space, and concluded that the transition zone could be twice as wide as their old 3-D model result that used a linear transition zone. What is the real character of the transition zone? With improved GPS data including vertical velocities we

may eventually be able to answer this question.

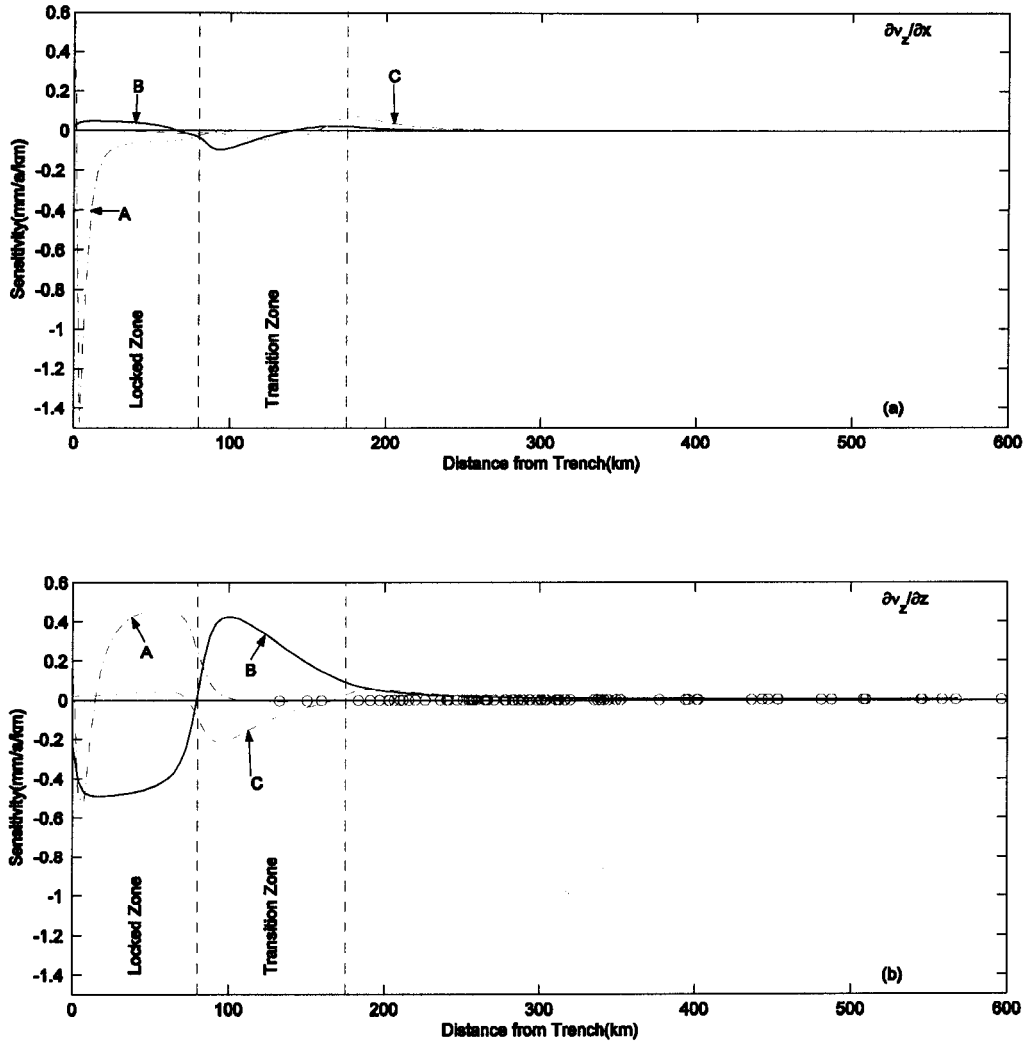


Figure 6.1: Sensitivity of vertical surface velocity V_z to variations in the X, Z coordinates of model control points, A, B and C (shown in Figure 3.8). The upper figure (a) shows the sensitivity to changing X at the control-points. The lower figure (b) shows the sensitivity to changing Z. The dashdotted curve is for control point A, the solid curve is for control point B, and the dashed curve is for control point C. In each figure, the origin is at the trench. The red circles are locations of projected GPS stations between latitude 47°N and 50°N . The vertical dashed lines indicate the boundaries between the locked and transition zones. The model parameters in this figure correspond to a NE cross-section through Seattle. For sensitivity of horizontal velocity V_x to variations in the X, Z coordinates of model control points, A, B and C, please refer to Figure 3.9

Bibliography

- Adams, J., Paleoseismicity of the Cascadia subduction zone: Evidence from turbidites off the Oregon-Washington margin, *Tectonics*, 9, 569-583, 1990.
- Argus, D.F., and R.G. Gordon, Current Sierra Nevada-North America motion from Very Long Baseline Interferometry: Implications for the kinematics of the western United States, *Geology*, 19, 1085-1088, 1991.
- Argus, D.F., and M.B. Heflin, Plate motion and crustal deformation estimated with geodetic data from the Global Positioning System, *Geophys. Res. Lett.*, 22 (15), 1973-1976, 1995.
- Argus, D.E., and R.G. Gordon, Tests of the rigid-plate hypothesis and bounds on intraplate deformation using geodetic data from very long baseline interferometry, *J. Geophys. Res.*, 101 (6), 13,555-13,572, 1996.
- Aki, K., and P.G. Richards, *Quantitative Seismology*, 557 pp., W. H. Freeman and Company, New York, USA, 1980.
- Atwater, T., Implications of plate tectonics for the Cenozoic tectonic evolution of western North America, *Bulletin of the Geological Society of America*, 81, 3513-3536, 1970.
- Atwater, B.F., Evidence for great Holocene earthquakes along the outer coast of Washington state, *Science*, 236, 942-944, 1987.
- Atwater, B.F., M. Stuiver, and D.K. Yamaguchi, Radiocarbon test of earthquake magnitude at the Cascadia subduction zone, *Nature*, 353 (6340), 156-158, 1991.
- Atwater, B.F., A.R. Nelson, J.J. Clague, G.A. Carver, D.K. Yamaguchi, P.T. Bobrowsky, J. Bourgeois, M.E. Darienzo, W.C. Grant, E. Hemphill-Haley, H.M. Kelsey, G.C. Jacoby, S.P. Nishenko, S.P. Palmer, C.D. Peterson, and M.A. Reinhart, Summary of coastal geologic evidence for past great earthquakes at the Cascadia subduction zone, *Earthquake Spectra*, 11 (1), 1-18, 1995.
- Atwater, B.F., Coastal evidence for great earthquakes in western Washington, *U. S. Geological Survey Professional Paper*, 1560, 77-90, 1996.
- Bacon, C.R., M.A. Lanphere, and D.E. Champion, Late Quaternary slip rate and seismic hazards of the West Klamath Lake fault zone near Crater Lake, Oregon Cascades, *Geology*, 27(1), 43 - 46, 1999.
- Bakun, W.H., Seismicity of California's north coast, *Bulletin of the Seismo. Soc. of America*, 90 (4), 797-812, 2000.
- Bakun, W.H., R.A. Haugerud, M.G. Hopper, and R.S. Ludwin, The December 1872 Washington State earthquake, *Bull. Seismol. Soc. Am.*, 92 (8): 3239-3258, 2002.

- Bar-Sever, Y.E., P.M. Kroger, and J.A. Borjesson, Estimating horizontal gradients of tropospheric path delay with a single GPS receiver, *J. Geophys. Res.*, 103 (3), 5019-5035, 1998.
- Batt, G.E., Brandon, M.T., Farley, K.A., Roden-Tice, M., Tectonic synthesis of the Olympic mountains segment of the Cascadia wedge, using two – dimensional thermal and kinematic modeling of thermochronological ages, *J. Geophys. Res.*, 106 (B11), 20731 – 20746, 2001.
- Beck, M.E., Has the Washington and Oregon Coast Range moved northward? *Geology*, 12, 737-740, 1984.
- Beck, M.E., Jr., R.F. Burmester, D.E. Craig, C.S. Gromme, and R.E. Wells, Paleomagnetism of middle Tertiary volcanic rocks from the Western Cascade Series, Northern California, *J. Geophys. Res.*, 91 (8), 8219-8230, 1986.
- Beeson, M.H., and T.L. Tolan, The Columbia River Basalt Group in the Cascade Range: A middle Miocene reference datum for structural analysis, *J. Geophys. Res.*, 95, 19,547 – 19,559, 1990.
- Blackwell, D.D., J.L. Steele, S. Kelley, and M.A. Korosec, Heat flow in the state of Washington and thermal conditions in the Cascade Range, *J. Geophys. Res.*, 95 (12), 19,495-19,516, 1990a.
- Blackwell, D.D., J.L. Steele, S. Kelley, and M.A. Korosec, Heat flow in the state of Washington and thermal conditions in the Cascade Range, *J. Geophys. Res.*, 95 (12), 19,495-19,516, 1990b.
- Blakely, R.J., and R.C. Jachens, Volcanism, isostatic residual gravity, and regional tectonic setting of the Cascade volcanic province, *J. Geophys. Res.*, 95 (12), 19, 1990.
- Blewitt, G., Carrier phase ambiguity resolution for the Global Positioning System applied to geodetic baselines up to 2000 km, *J. Geophys. Res.*, 94 (8), 10,187-11,203, 1989.
- Blewitt, G., Advances in Global Positioning System technology for geodynamics investigations: 1978-1992, in *Contributions of Space Geodesy to Geodynamics Technology*, Geodyn. Ser., edited by D.E. Smith, and D.L. Turcotte, pp. 195-213, AGU, Washington, D.C., 1993.
- Blewitt, G., M.B. Heflin, K.J. Hurst, D.C. Jefferson, F.H. Webb, and J.F. Zumberge, Absolute far-field displacements from the 28 June 1992 Landers earthquake sequence, *Nature*, 361 (6410), 340-342, 1993.
- Bostock, M.G., and J.C. VanDecar, Upper mantle structure of the northern Cascadia subduction zone, *Can. J. Earth Sci.*, 32, 1 – 12, 1995.
- Boucher, C., Z. Altamimi, and P. Sillard, The 1997 International Terrestrial Reference Frame (ITRF97), in, Observatoire de Paris, Paris, France, 1999.
- Brandon, M. T., and Calderwood, A. R., High-pressure metamorphism and uplift of the Olympic subduction complex: *Geology*, v. 18, p. 1252–1255, 1990.

- Brandon, M.T., and J.A. Vance, Tectonic evolution of the Cenozoic Olympic subduction complex, Washington State, as deduced from fission track ages for detrital zircons, *Amer. J. of Sci.*, 22 (8), 565-636, 1992.
- Brandon, M.T., M.K. Roden, and J.I. Garver, Late Cenozoic exhumation of the Cascadia accretionary wedge in the Olympic Mountains, Northwest Washington State, *Geol. Soc. Am. Bull.*, 110 (8), 985-1009, 1998.
- Braunmiller, J., J Nabelek, B. Leitner, and A. Qamar, The 1993 Klamath Falls, Oregon, earthquake sequence: Source mechanisms from regional data: *Geophys. Res. Let.*, v. 22, p. 105-108, 1995.
- Brocher, T.M., ten Brink US, T Abramovitz, Synthesis of crustal seismic structure and implications for the concept of a slab gap beneath coastal California, *Intl. Geol. Rew.*, 41(3), 263-274, 1999.
- Brocher, T.M., Parsons, T., et. Al., Upper crustal structure in Puget Lowland, Washington: Results from the 1998 Seismic Hazards Investigation in Puget Sound, *Journal of Geophysical Research*, 106 (B7), 13541-13564, 2001.
- Brune, J. N., Seismic moment, seismicity and rate of slip along major fault zones, *J. Geophys. Res.*, 73, 777-784, 1968.
- Bruning, J.L, and B.L. Kintz, Computational handbook of statistics, Scott, Foresman and Co., 308, 1977.
- Bucknam, R.C., H.E. Hemphill, and E.B. Leopold, Abrupt uplift within the past 1700 years at southern Puget Sound, Washington, *Science*, 258 (5088), 1611-1614, 1992.
- Cassidy, J.F., Teleseismic receiver function analysis of the crust and upper mantle of southwestern British Columbia, *Ph. D. Thesis*, University of British Columbia, Vancouver, BC, Canada, 1991.
- Cassidy, J.F., R.M. Ellis, S-wave velocity structure of the northern Cascadia subduction zone, *J. Geophys. Res.*, 98 (B3), 4,407-4,421, 1993.
- Cassidy, J.F., A comparison of the receiver structure beneath stations of the Canadian National Seismograph Network, *Can. J. Earth Sci.*, 32, 938-951, 1995.
- Clague, J.J., Naesgaard, E., and Nelson, A.R., Age and significance of earthquake-induced liquefaction near Vancouver, British Columbia, Canada: *Canadian Geotechnical Journal*, V.34, 53-62, 1997.
- Clague, J.J., Bobrowsky, P.T., Evidence for a large earthquake and tsunami 100-400 years ago on western Vancouver-Island, British-Columbia, *Quaternary Research*, 41 (2), 176-184, 1994.
- Clague, J.J., Bobrowsky, P.T., The geological signature of great earthquakes off Canada's West Coast, *Geoscience Canada*, 26 (1), 1-15, 1999.

- Clague, J.J., and T. S. James, History and isostatic effects of the last ice sheet in southern British Columbia, *Quat. Sci. Rev.*, 21, 71– 87, 2002.
- Clowes, R.M., M.T. Brandon, A.G. Green, C.J. Yorath, A. Sutherland Brown, E.R. Kanasewich, and C. Spencer, LITHOPROBE-Southern Vancouver Island: Cenozoic subduction complex imaged by deep seismic reflections, *Can. J. Earth Sci.*, 24, 31-51, 1987.
- Crosson, R.S., Small earthquakes, structure, and tectonics of the Puget Sound region, *Bull. Seismol. Soc. Am.*, 62, 1133 – 1171, 1972.
- Crosson, R.S., and T.J. Owens, Slab geometry of the Cascadia subduction zone beneath Washington from earthquake hypocenters and teleseismic converted waves, *Geophys. Res. Lett.*, 14 (8), 824-827, 1987.
- Darienzo, M.E., and C.D. Peterson, Magnitude and frequency of subduction-zone earthquakes along the northern Oregon coast in the past 3,000 years, *Oregon Geology*, 57, 3-12, 1995.
- DeMets, C., R.G. Gordon, D.F. Argus, and S. Stein, Current plate motions, *Geophys. J. Int.*, 101 (2), 425-478, 1990.
- DeMets, C., R.G. Gordon, D.F. Argus, and S. Stein, Effect of recent revisions to the geomagnetic reversal time scale on estimates of current plate motions, *Geophys. Res. Lett.*, 21 (20), 2191-2194, 1994.
- Dewberry, S.R., and R.S. Crosson, The M (sub D) 5.0 earthquake of 29 January 1995 in the Puget Lowland of western Washington; an event on the Seattle Fault?, *Bull. Seismol. Soc. Amer.*, 86 (4), 1167-1172, 1996.
- Dixon, T.H., An introduction to the Global Positioning System and some geological applications, *Rev. Geophys.*, 29 (2), 249-276, 1991.
- Dragert, H., R.D. Hyndman, R.G. C., and K. Wang, Current deformation and the width of the seismogenic zone of the northern Cascadia subduction thrust, *J. Geophys. Res.*, 99 (1), 653-668, 1994.
- Dragert, H., and R.D. Hyndman, Continuous GPS monitoring of elastic strain in the northern Cascadia subduction zone, *Geophys. Res. Lett.*, 22 (7), 755-758, 1995.
- Dragert, H., X. Chen, and J. Kouba, GPS monitoring of crustal strain in Southwest British Columbia with the Western Canada deformation array, *Geomatica*, 49 (3), 301-313, 1995.
- Dragert, H., Wang, K., and James, T. S., A silent slip event on the deeper Cascadia subduction interface, *Science*, 292 (5521): 1525-1528, 2001.
- Duncan, R.A., and K.D. LeVerne, Plate tectonic evolution of the Cascades arc-subduction complex, in *Neotectonics of North America*, edited by D.B. Slemmons, E.R. Engdahl, M.D. Zoback, and D.D. Blackwell, pp. 413-438, Geological Society of America, Boulder, CO, United States., 1991.

- Engebretson, D.C., A. Cox, and R.G. Gordon, Relative motions between oceanic plates of the Pacific Basin, *J. Geophys. Res.*, 89 (12), 10,291-210,310, 1984.
- England, P.C., and R.E. Wells, Neogene rotations and quasicontinuous deformation of the Pacific Northwest continental margin, *Geology*, 19,978-981, 1991.
- Finn, C.A., Geophysical constraints on Washington convergent margin structure, *J. Geophys. Res.*, 95 (12), 19, 1990.
- Fleming, S. W., and A. M. Tréhu, Crustal structure beneath the central Oregon convergent margin from potential-field modeling: Evidence for a buried basement ridge in local contact with seaward dipping backstop, *J. Geophys. Res.*, 104 (B9), 20,431 – 20,447, 1999.
- Flück, P., 3-D dislocation model for great earthquakes of the Cascadia subduction zone, *Diploma Thesis*, Swiss Federal Institute of Technology (ETH), Zürich, Switzerland, 1996.
- Flück, P., R.D. Hyndman, and K. Wang, Three-dimensional dislocation model for great earthquakes of the Cascadia subduction zone, *J. Geophys. Res.*, 102 (9), 20,539-20,550, 1997.
- Freund, L.B., and D.M. Barnett, A two-dimensional analysis of surface deformation due to slipslip faulting, *Bull. Seis. Soc. Am.*, 66 (3), 667-675, 1976.
- Gardner, C.A., K.M. Scott, C.D. Miller, B. Myers, W. Hildreth, and P.T. Pringle, Potential Volcanic Hazards from Future Activity of Mount Baker, Washington, *USGS Open-File Report 95-498*, 1995.
- Goldfinger, C., and eight others, Neotectonic map of the Oregon continental margin and adjacent abyssal plain: Oregon Department of Geology and Mineral Industries Open-File Report 0-92-4, 17 p., 1992b.
- Goldfinger, C., L.D. Kulm, R.S. Yeats, L. McNeill, and C. Hummon, Oblique strike-slip faulting of the central Cascadia submarine forearc, *J. Geophys. Res.*, 102 (4), 8217-8243, 1997.
- Gower, H.D., J.C. Yount, and R.S. Crosson, Seismotectonic map of the Puget Sound region, Washington, U. S. Geological Survey, Reston, VA, United States., 1985.
- Grant, W.C., C.S. Weaver, and J.E. Zollweg, The 14 February Elk Lake, Washington, earthquake sequence, *Bull. Seismol. Soc. Am.*, 74, 1289 – 1309, 1984.
- Gregorius, T., *GIPSY-OASIS II: How it works*, 109 pp., University of Newcastle upon Tyne, Newcastle upon Tyne, U.K., 1996.
- Guffanti, M., and C.S. Weaver, Distribution of late Cenozoic volcanic vents in the Cascade Range; volcanic arc segmentation and regional tectonic considerations, *J. Geophys. Res.*, 93 (6), 6513-6529, 1988.
- Gurtner, W., G. Mader, and D. MacArthur, A common exchange format for GPS data, in *GPS*

Bulletin, pp. 1-11, National Geodetic Survey, Rockville, Maryland, 1989.

- Gutscher, M.-A., W. Spakman, H. Bijwaard, and E. R. Engdahl, Geodynamics of flat subduction: Seismicity and tomographic constraints from the Andean margin, *Tectonics*, 9, 814–833, 2000.
- Gutscher, Marc-Andre, S.M. Peacock, Thermal models of flat subduction and the rupture zone of great subduction earthquakes, *J. GEOPHYS. RES.*, V. 108 (B1), 2009, doi:10.1029/2001JB000787, 2003.
- Hagstrum JT, Swanson DA, Evarts RC, Paleomagnetism of an east-west transect across the Cascade arc in southern Washington: Implications for regional tectonism, *JGR*, 104(B6), p12853-12863, Jun 10 1999.
- Hawkins, F.F., L.L. Foley, and R.C. LaForge, Seismotectonic study for Fish Lake and Fourmile Lake dams, Rogue River project, Oregon, *Seismotectonic Report 98-3*, 26 pp., U.S. Bureau of Reclamation, Denver, Col., 1989.
- Heaton, T.H., and H. Kanamori, Seismic potential associated with subduction in the Northwestern United States, *Bull. Seismol. Soc. Amer.*, 74 (3), 933-941, 1984.
- Heaton, T.H., and S.H. Hartzell, Earthquake hazards on the Cascadia subduction zone, *Science*, 236, 162-168, 1987.
- Heller, P.L., R.W. Tabor, and C.A. Siczek, Paleogeographic evolution of the United States Pacific Northwest during Paleogene time, *Can. J. Earth Sci.*, 24, 1652-1667, 1987.
- Henry, S. G., and H. N. Pollack, Terrestrial heat flow above the Andean subduction zone in Bolivia and Peru, *J. Geophys. Res.*, 93, 15,153 – 15,162, 1988.
- Hughes, J.M., R.E. Stoiber, and M.J. Carr, Segmentation of the Cascade volcanic chain, *Geology*, 8, 15 – 17, 1980.
- Hutchinson, I., Guilbault, J.P., Clague, J.J., Bobrowsky, P.T., Tsunamis and tectonic deformation at the northern cascadia margin: a 3000-year record from Deserted Lake, Vancouver Island, British Columbia, Canada, Holocene, 10 (4), 429-439, 2000.
- Hyndman, R.D., C.J. Yorath, R.M. Clowes, and E.E. Davis, The northern Cascadia subduction zone at Vancouver Island: Seismic structure and tectonic history, *Can. J. Earth Sci.*, 27, 313-329, 1990.
- Hyndman, R.D., G.D. Spence, T. Yuan, and E.E. Davis, Regional geophysics and structural framework of the Vancouver Island margin accretionary prism, *Proc. Ocean Drill. Program, Initial Rep.*, 146, 399-419, 1994.
- Hyndman, R.D., and K. Wang, Thermal constraints on the zone of major thrust earthquake failure; the Cascadia subduction zone, *J. Geophys. Res.*, 98 (2), 2039-2060, 1993.
- Hyndman, R.D., K. Wang, and M. Yamano, Thermal constraints on the seismogenic portion of

the southwestern Japan subduction thrust, *J. Geophys. Res.*, 100 (8), 15,373-315,392, 1995.

- Hyndman, R.D., and K. Wang, The rupture zone of Cascadia great earthquakes from current deformation and the thermal regime, *J. Geophys. Res.*, 100 (11), 22,133-122,154, 1995.
- Hyndman, R.D., M. Yamano, and D.A. Oleskevich, The seismogenic zone of subduction thrust faults, *The Island Arc*, 6 (3), 244-260, 1997.
- Hyndman, R.D, S. Mazzotti, D. Weichert, and G.C. Rogers, Frequency of large crustal earthquakes in Puget Sound – Southern Georgia Strait predicted from geodetic and geological deformation rates, *Jour. Geophys. Res.*, 108(B1), 20033, 2003.
- Irving, E., Paleopoles and paleolatitudes of North America and speculations about displaced terranes, *Can. J. Earth Sci.*, 16, 669–694, 1979.
- Jacoby, G.C., Bunker, D.E., and Benson, B.E., Tree-ring evidence for an A.D. 1700 Cascadia earthquake in Washington and Northern Oregon, *Geology*, V. 25, 999-1002, 1997.
- James, T. S., J. J. Clague, K. Wang, and I. Hutchinson, Postglacial rebound at the northern Cascadia subduction zone, *Quat. Sci. Rev.*, 19, 1527–1541, 2000.
- Johnson, S. Y., Evidence for a margin-truncating transcurrent fault (pre–late Eocene) in western Washington: *Geology*, 12, 538–541, 1984a.
- Johnson, S.Y., Eocene strike-slip faulting and nonmarine basin formation in Washington, *in* Biddle, K. T., and Christie-Blick, N., eds., *Strike-slip deformation, basin formation, and sedimentation: Society of Economic Paleontologists and Mineralogists Special Publication 37*, 283–30, 1985.
- Johnson, S.Y., C.J. Potter, and J.M. Armentrout, Origin and evolution of the Seattle Fault and Seattle Basin, Washington, *Geology*, 22 (1), ages 71-74, 1994.
- Johnson, S.Y., C.J. Potter, J.M. Armentrout, J.J. Miller, C.A. Finn, and C.S. Weaver, The southern Whidbey Island Fault; an active structure in the Puget Lowland, Washington, *Geol. Soc. Am. Bull.*, 108 (3), 334-354, 1996.
- Johnson, S.Y., Dadisman, S.V., Childs, J. R., Stanley, W.D., Active tectonics of the Seattle fault and central Puget Sound, Washington – Implications for earthquake hazards, *Geological Society of America Bulletin*, 111 (7), 1042 -1053, 1999.
- Kanamori, H., The energy release in great earthquakes, *J. Geophys. Res.*, 82, 2981-2987, 1977.
- Karlin, R.E., Abella, S.E.B., A history of Pacific Northwest earthquakes recorded in Holocene sediments from Lake Washington, 101 (B3), 6137-6150, 1996.
- Kato, T., G.S. El Fiky, E.N. Oware, and S. Miyazaki, Crustal strains in the Japanese islands as deduced from dense GPS array, *Geophys. Res. Lett.*, 25 (18), 3445-3448, 1998.
- Kelsey, H.M., Witter, R.C., Hemphill-Haley, E., Plate-boundary earthquakes and tsunamis of

the past 5500 years, Sixes River estuary, southern Oregon, Geological Society of America Bulletin, 114 (3), 298-314, 2002.

- Khazaradze G., A. Qamar, and H. Dragert, Tectonic deformation in western Washington from continuous GPS measurements, , *Geophys. Res. Letters*, v.26, p3153-3156, 1999.
- King, R. W. and Y. Bock, Documentation for the GAMIT GPS analysis software, Release 9.82, Massachusetts Institute of Technology, Cambridge, 1999.
- Kostrov, V.V., Seismic moment and energy of earthquakes, and seismic flow of rock, *Izv. Acad. Sci. USSR Phys. Solid Earth*, English Transl., 1, 13-21, 1974.
- Lapp, D.B., Owens T.J., Crosson R.S., P-wave-form analysis for local subduction geometry south of Puget Sound, Washington, *Pure and Applied Geophys.*, 133 (2): 349-365 1990.
- Leick, A., GPS satellite surveying, 560 pp., John Wiley and Sons, New York, NY, United States, 1995.
- Lisowski, M., W.H. Prescott, H. Dragert, and S.R. Holdahl, Results from 1986 and 1987 GPS survey across the Strait of Juan de Fuca, Washington and British Columbia, *Seismol. Res. Lett.*, 60, 1, 1989.
- Ludwin, R.S., C.S. Weaver, and R.S. Crosson, Seismicity of Washington and Oregon, in *Neotectonics of North America*, edited by D.B. Slemmons, E.R. Engdahl, M.D. Zoback, and D.D. Blackwell, pp. 77-97, Geological Society of America, Boulder, CO, United States., 1991.
- Ma, L., R. Crosson, and R. Ludwin, Western Washington earthquake focal mechanisms and their relationship to regional tectonic stress, in *Assessing earthquake hazards and reducing risk in the Pacific Northwest: Volume 1*, Edited by A.M. Rogers, T.J. Walsh, W.J. Kockelman, and G.R. Priest, pp. 257 – 283, 1996.
- Magee, M.E., and M.L. Zoback, Wellbore breakout analysis for determining tectonic stress orientations in Washington State, U.S. Geological Survey Open-File Report 92-715, 56p.
- Magill, J.R., R.E. Wells, R.W. Simpson, and A.V. Cox, Post 12 m.y. rotation of southwest Washington, *J. Geophys. Res.*, 87 (5), 3761-3776, 1982.
- Malone, S.D., A. Qamar, and C. Jonientz-Trisler, Recent seismicity at Mount Rainier, Washington, Paper presented at 86th Annual Meeting, Seis. Soc. Am., San Francisco, Calif., April 25 – 27, 1991.
- Malone, S.D., G.H. Rothe, and S.W. Smith, Details of microearthquake swarms in the Columbia Basin, Washington, *Bull. Seismol. Soc. Am.*, 65, 855 – 864, 1975.
- Malone, S.D., S.S. Bor, Attenuation patterns in the Pacific Northwest based on intensity data and the location of the 1872 north Cascades earthquake, *Bull. Seismol. Soc. Am.*, 69 (2), 531-546, 1979.

- Mann, G.M., and C.E. Meyer, Late Cenozoic structure and correlations to seismicity along the Olympic – Wallowa Lineament, northwest United States, *Geol. Soc. Am. Bull.*, 105, 853 – 871, 1993.
- Mastin, L.G., and R. Waitt, Glacier Peak -- History and Hazards of a Cascade Volcano, *USGS Fact Sheet 058-00*, 2000.
- McCaffrey, R., Oblique plate convergence, slip vectors, and forearc deformation, *J. Geophys. Res.*, 97 (6), 8905-8915, 1992.
- McCaffrey, R., and C. Goldfinger, Forearc deformation and great subduction earthquakes: Implications for Cascadia offshore earthquake potential, *Science*, 267, 856-859, 1995.
- McCaffrey, R., M.D. Long, C. Goldfinger, P.C. Zwick, J.L. Nabelek, C.K. Johnson, C. Smith, Rotation and plate locking at the southern Cascadia subduction zone, *J. Geophys. Res.*, 27 (19), 3117-3120, 2000.
- McCrory, P.A., Tectonic model explaining divergent contraction directions along the Cascadia subduction margin, Washington, *Geology*, 24, 929 – 932, 1996.
- Mege, D., Reidel, S.P., A method for estimating 2D wrinkle ridge strain from application of fault displacement scaling to the Yakima folds, Washington, *Geophys. Res. Lett.*, 28 (18), 3545-3548, 2001.
- Michaelson, C.A., and Weaver, C.S., Upper mantle structure from teleseismic P wave arrivals in Washington and northern Oregon, *J. Geophys. Res.*, 91, 2077-2094, 1986.
- Miller, K.C., G.R. Keller, and J.M. Gridley, Crustal structure along the west flank of the Cascades, western Washington, *J. Geophys. Res.*, 102 (B8), 17,857 – 17,873, 1997.
- Miller, M.M., D. J. Johnson, C.M. Rubin, H. Dragert, K. Wang, A. Qamar, and C. Goldfinger, GPS-determination of along-strike variation in Cascadia margin kinematics: Implication for relative plate motion, subduction zone coupling, and permanent deformation, *Tectonics*, 20 (2), 161-176, 2001.
- Miller, M.M., Melbourne, T., Johnson, D.J., Sumner, W.Q., Periodic slow earthquakes from the Cascadia subduction zone, *Science*, 295 (5564): 2423-2423, 2002.
- Mitchell, C.E., P. Vincent, R.J. Weldon, and M.A. Richards, Present-day vertical deformation of the Cascadia margin, Pacific Northwest, United States, *J. Geophys. Res.*, 99 (6), 12,257-212,277, 1994.
- Monger, J.W.H., R.A. Price, and D.J. Tempelman-Kluit, Tectonic accretion and the origin of the two major metamorphic and plutonic belts in the Canadian Cordillera, *Geology*, 10 (2), 70-75, 1982.
- Moran, S.C., Lees, J.M., Malone, S.D., P wave crustal velocity structure in the greater Mount Rainier area from local earthquake tomography, *J. Geophys. Res.*, 104 (B5), 10775-10786, 1999.

- Murray, M.H., and M. Lisowski, Strain accumulation along the Cascadia subduction zone from triangulation, trilateration, and GPS measurements, *EOS, Trans. AGU*, 75 (44), 178, 1994.
- Murray, M.H., G.A. Marshall, M. Lisowski, and R.S. Stein, The 1992 M = Cape Mendocino, California, earthquake; coseismic deformation at the south end of the Cascadia Megathrust, *J. Geophys. Res.*, 101 (8), 17,707-17,725, 1996.
- Murray, M.H., Lisowski M, Strain accumulation along the Cascadia subduction zone, *Geophys. Res. Lett.*, 27 (22), p3631-3634, Nov 15 2000.
- Nelson, A.R., Atwater, B.F., Brobowski, P.T., Bradley, L., Clague, J.L., Carver, G.A., Darienzo, M.A., Grant, W.C., Krueger, H.W., Sparks, R., Stafford, T., and Stuiver, M., Radiocarbon evidence for extensive plate boundary rupture about 300 years ago at the Cascadia subduction zone: *Nature*, v. 378, p. 371-374, 1995.
- Noson, L.L., A. Qamar, and G. W. Thorsen, Washington State Harzards, 1988.
- Okada, Y., Surface deformation due to shear and tensile faults in a half-space, *Bull. Seismol. Soc. Am.*, 75, 1135-1154, 1985.
- Okada, Y., Internal deformation due to shear and tensile faults in a half-space, *Bull. Seismol. Soc. Amer.*, 82 (2): 1018-1040, 1992.
- Oleskevich, D.A., Hyndman, R.D., Wang, K., The updip and wondip limits to great subduction earthquakes: Thermal and structural models of Cascadia, south Alaska, SW Japan, and Chile, *J. Geophys. Res.*, 104(B7), 14965-14991, 1999.
- Owens, T.J., Crosson R.S., Hendrickson M.A., Constraints on the subduction geometry beneath western Washington from broad-band teleseismic waveform modeling, *B SEISMOL SOC AM*, 78 (3): 1319-1334, 1988.
- Parker, R.L., Geophysical inverse theory, Princeton University Press, ISBN 0-691-03634-9, 1994.
- Parsons, T., A.M. Trehu, J.H. Luetgert, K. Miller, F. Kilbride, R.E. Wells, M.A. Fisher, E. Flueh, U.S. ten Brink, and N.I. Christensen, A new view into the Cascadia subduction zone and volcanic arc; implications for earthquake hazards along the Washington margin, *Geology*, 26 (3), 199-202, 1998.
- Pazzaglia, F.J., M.T. Brandon, A fluvial record of long-term steady-state uplift and erosion across the Cascadia forearc high, western Washington State, *Am. J. Sci.*, 301, 385-431, 2001.
- Peterson, C. P., Kulm, L. D., and Gray, J. J., Geologic map of the ocean floor off Oregon and the adjacent continental margin: Oregon Department of Geology and Mineral Industries Map GMS-42, scale 1:500 000, 1986.
- Peltier, W.R., Ice-age paleotopography. *Science* 265, 195-201, 1994.

- Pezzopane, S.K., and R.J. Weldon, II, Tectonic role of active faulting in central Oregon, *Tectonics*, 12 (5), 1140-1169, 1993.
- Pratt, T.L., S.Y. Johnson, C.J. Potter, W.J. Stephenson, and C.A. Finn, Seismic reflection images beneath Puget Sound, western Washington State: The Puget Lowland thrust sheet hypothesis, *J. Geophys. Res.*, 102, 27,469 – 27,489, 1997.
- Priest, G.R., Woller, N.M., Black, G.L., Evans, S.H., Overview of the geology of the central Oregon Cascade Range, Spec. Pap. Oreg. Dep. Geol. Miner. Ind., 15, 3-28, 1983.
- Raisz, E., The Olympic – Wallowa lineament, *American Journal of Science*, V. 243-A, 479 – 485, 1945.
- Qamar, A., and R.S. Ludwin, Stress directions in Washington and northern Oregon inferred from earthquake focal mechanisms, *Seis. Res. Lett.*, 63, 23, 1992.
- Rasmussen, J., and E. Humphreys, Tomographic image of the Juan de Fuca plate beneath Washington and western Oregon using teleseismic P – wave travel times, *Geophys. Res. Lett.*, 15, 1417 – 1420, 1988.
- Reidel, S., The saddle Mountains: The evolution of an anticline in the Yakima fold belt, *Am. J. Sci.*, 284, 942 – 977, 1984.
- Reirners, P.W., T.A. Ehlers, J.I. Garver, S.G. Mitchell, D.R. Montgomery, J.A. Vance, and Stefan Nicolescu, Late Miocene exhumation and uplift of the Washington Cascade Range, *Geology*, 30(9), 767 – 770, 2002.
- Riddihough, R.P., Recent movements of the Juan de Fuca plate system, *J. Geophys. Res.*, 89 (8), 6980-6994, 1984.
- Rielinger, R.E., and J. Adams, Geodetic evidence for active landward tilting of the Oregon and Washington coastal ranges, *Geophysical Research Letters*, 9, 401-403, 1982.
- Rogers, G.C, Variation in Cascade volcanism with margin orientation, *Geology*, 13(7), 495-498, 1985.
- Rogers, G.C, Earthquakes in the Vancouver area, in *Geology and Geological Hazards of the Vancouver Region, Southwestern British Columbia*, edited by J.W.H. Monger, *Geol. Surv. Can. Bull.*, 481, 221-229, 1994.
- Satake, K., K. Shimazaki, Y. Tsuji, and K. Ueda, Time and size of a giant earthquake in Cascadia inferred from Japanese tsunami records of January 1700, *Nature*, 379 (6562), 246-249, 1996.
- Sauber, J., W. Thatcher, S.C. Solomon, and M. Lisowski, Geodetic slip rate for the eastern California shear zone and the recurrence time of Mojave desert earthquakes, *Nature*, 367 (January 20, 1994), 264-266, 1994.
- Savage, J.C., M. Lisowski, and W.H. Prescott, Geodetic strain measurements in Washington, *J.*

Geophys. Res., 86, (6), 4929-4940, 1981.

- Savage, J.C., A dislocation model of strain accumulation and release at a subduction zone, *J. Geophys. Res.*, 88 (6), 4984-4996, 1983.
- Savage, J.C., M. Lisowski, and W.H. Prescott, Strain accumulation in western Washington, *J. Geophys. Res.*, 96 (9), 14,493-414,507, 1991.
- Savage, J.C., and W. Thatcher, Interseismic deformation at the Nankai Trough, Japan, subduction zone, *J. Geophys. Res.*, 97 (7), 11,117-11,135, 1992.
- Savage, J.C., J.L. Svarc, W.H. Prescott, M. H. Murray, Deformation across the forearc of the Cascadia subduction zone at Cape Blanco, Oregon, *J. Geophys. Res.*, 105 (B2), 3095-3102, 2000.
- Sherrod, D.R., Historic and prehistoric earthquakes near Klamath Falls, Oregon, *Earthquakes and volcanoes*, 24, 106 – 120, 1993.
- Smith, R.L., and Luedke, R.G, Potentially active volcanic lineaments and loci in western conterminous United States, in *Explosive Volcanism: Inception, Evolution, Hazards*, 47-66, National Academy Press, Washington D. C., 1984.
- Snavely, P. D., N. S. MacLeod, and H. C. Wagner, Tholeiitic and alkalic basalts of the Eocene Siletz River volcanics, Oregon Coast Range, *Am. J. Sci.*, 266, 454–481, 1968.
- Snavely, P.D., Jr., Tertiary geologic framework, neotectonics, and petroleum potential of the Oregon-Washington continental margin, in *Geology and resource potential of the continental margin of western North America and adjacent ocean basins-Beaufort sea to Baja California*, edited by D.V. Scholl, A. Grantz, and J.G. Vedder, pp. 305-335, Circum Pacific Council for Energy and Mineral Resources, Earth Science Series, 1987.
- Snyder, J.P., Map Projection, A working manual, U.S.G.S. professional paper 1395, 1987.
- Stanley, W.D., C. Finn, and J.L. Plesha, Tectonics and conductivity structures in the southern Washington Cascades, *J. Geophys. Res.*, 92, 10179-10193, 1987.
- Stanley, W.D., W.D. Mooney, G.S. Fuis, Deep crustal structure of the Cascade Range and surrounding regions from seismic refraction and magnetotelluric data, *J. Geophys. Res.*, 95 (B12), 19419-19438, 1990.
- Steketee, L.A., On Volterra's dislocations in a semi-infinite elastic medium, *Can. J. Phys.*, 36, 192-205, 1958a.
- Steketee, L.A., Some geophysical applications of the elasticity theory of dislocations, *Can. J. Phys.*, 36, 1168, 1958b.
- Svarc, J.L., J.C. Savage, W.H. Prescott, M.H. Murraray, Strain accumulation and rotation in western Oregon and southwestern Washington, *JGR*, 107(B5): art. No. 2087 May 10 2002.

- Tabor, R.W., Age of Olympic metamorphism, Washington; K-Ar dating of low – grade metamorphic rocks, *Geol. Soc. Am. Bull.*, 83, 1805 – 1816, 1972.
- Tabor, R. W., and Cady, W. H., Geologic map of the Olympic Peninsula: U.S. Geological Survey Map I-994, scale 1:125000, 1978a.
- Tabor, R. W., and Cady, W. H., The structure of the Olympic Mountains, Washington—Analysis of a subduction zone: U.S. Geological Survey Professional Paper 1033, 38 p, 1978b.
- Thatcher, W., Silent slip on the Cascadia subduction interface, *Science*, 292 (5521): 1495-1496, 2001.
- Thompson, K.L., and A. Qamar, The seismicity of Mount Rainier, Washington (abstract), *Seismol., Res., Lett.*, 60, 31, 1989.
- Turcotte, D.T., and G. Schubert, *Geodynamics, Applications of Continuum Physics to Geological Problems*, 450 pp., John Wiley & Sons, New York, N.Y., USA, 1982.
- Tréhu, A.M., I. Asudeh, T.M. Brocher, J.H. Luetgert, W.D. Mooney, J.L. Nabelek, and Y. Nakamura, Crustal architecture of the Cascadia forearc, *Science*, 266 (5183), 237-243, 1994.
- Tréhu, A.M., G.B. Lin, E. Maxwell, C. Goldfinger, A seismic-reflection profile across the Cascadia subduction zone offshore central Oregon – New constraints on methane distribution and crustal structure, *J. Geophys. Res.*, 100 (B8), 15,101-15,116, 1995.
- Tushingham, A.M., W.R. Peltier, 1991. ICE-3G: a new global model of late Pleistocene deglaciation based upon geophysical predictions of post-glacial relative sea level change. *J. Geophys. Res.*, 69, 4,497 – 4,523, 1991.
- Velasco, A.A., C.J. Ammon, and T. Lay, Recent large earthquakes near Cape Mendocino and in the Gorda Plate - broad-band source time functions, fault orientations, and rupture complexities, *J. Geophys. Res.*, 99 (B1), 711-728, 1994.
- Verdonck, D., Three-dimensional model of vertical deformation at the southern Cascadia subduction zone, Western United States, *Geology*, 23 (3), 261-264, 1995.
- Walcott, D., Neogene kinematics of western North America: *Tectonics*, v. 12, p. 326–333, 1993.
- Wang, K., H. Dragert, and H.J. Melosh, Finite element study of uplift and strain across Vancouver Island, *Can. J. Earth Sci.*, 31 (10), 1510-1522, 1994.
- Wang, K., and G.C. Rogers, Double seismic layers in the subducted Gorda plate and rheology of oceanic lithosphere, *Geophys. Res. Lett.*, 21, 121 – 124, 1994.
- Wang, K., T. Maulder, G.C. Rogers, and R.D. Hyndman, Case for very low coupling stress on the Cascadia subduction fault, *J. Geophys. Res.*, 100 (7), 12,907-12,918, 1995.

- Wang, K., Simplified analysis of horizontal stresses in a buttressed forearc sliver at an oblique subduction zone, *Geophys. Res. Lett.*, 23 (16), 2021-2024, 1996.
- Wang, K., and H. Dragert, Strain_M: computer program to calculate average strain tensor, Pacific Geoscience Centre, *Geological Survey of Canada*, 1998.
- Wang, K., J. He, H. Dragert, and T.S. James, Three-Dimensional viscoelastic deformation model for the Cascadia subduction zone, *Earth Planets Space*, 53, 295-306, 2001.
- Wang, K., R. Wells, S. Mazzotti, R.D. Hyndman, T. Sagiya, A revised dislocation model of interseismic deformation of the Cascadia subduction zone, *J. Geophys. Res.*, 108 (B1), 2026, doi:10.1029/2001JB001227, 2003.
- Watters, T.R., System of tectonic features common to Earth, Mars, and Venus, *Geology*, 20 (7), 609-612, 1992.
- Weaver, C.S., and Smith, S.W., Regional tectonics and earthquake hazard implications of a crustal fault zone in southwestern Washington, *J. Geophys. Res.*, 88, 10371-10383, 1983.
- Weaver, C.S., and Michaelson, C.A., Seismicity and volcanism in the Pacific Northwest: Evidence for the segmentation of the Juan de Fuca plate, *Geophys. Res. Lett.*, 12, 215-218, 1985.
- Weaver, C.S., and G.E. Baker, Geometry of the Juan de Fuca plate beneath Washington and northern Oregon from seismicity, *Bull. Seismol. Soc. Amer.*, 78 (1), 264-275, 1988.
- Webb, F.H., and J.F. Zumberge, *An introduction to GIPSY/OASIS II*, Jet Propulsion Laboratory, Pasadena, USA, 1997.
- Weichert, D. H., Estimation of the earthquake recurrence parameters from unequal observation periods for different magnitudes, *Bull. Seismol. Soc. Am.*, 70, 1337-1346, 1980.
- Wells, R.E., D.C. Engebretson, P.D.J. Snavely, and R.S. Coe, Cenozoic plate motions and the volcano-tectonic evolution of western Oregon and Washington, *Tectonics*, 3 (2), 275 - 294, 1984.
- Wells, R.E., and R.S. Coe, Paleomagnetism and geology of Eocene volcanic rocks of Southwest Washington, implications for mechanisms of tectonic rotation, *J. Geophys. Res.*, 90 (2), 1925- 1947, 1985.
- Wells, R.E., and P.L. Heller, The relative contribution of accretion, shear, and extension to Cenozoic tectonic rotation in the Pacific Northwest, *Geol. Soc. Am. Bull.*, 100 (3), 325-338, 1988.
- Wells, R.E., Paleomagnetic rotations and the Cenozoic tectonics of the Cascade arc, Washington, Oregon, and California, *J. Geophys. Res.*, 95 (12), 19,409-19,417, 1990.
- Wells, D. L., and K. J. Coppersmith, New empirical relationships among magnitude, rupture length, rupture width, rupture area and surface displacement, *Bull. Seismol. Soc. Am.*, 84,

974–1002, 1994.

- Wells, R.E., C.S. Weaver, and R.J. Blakely, Crustal block motions in the Pacific Northwest: Implications for the earthquake potential of the Cascadia forearc, *Geological Society of America Abstracts with Programs*, 28, 123, 1996.
- Wells, R.E., C.S. Weaver, and R.J. Blakely, Fore-arc migration in Cascadia and its neotectonic significance, *Geology*, 26 (8), 759-762, 1998.
- Wells, R. E., and R. W. Simpson, Northward migration of the Cascadia forearc in the northwestern U.S. and implications for subduction deformation, *Earth Planets Space*, 53, 275–283, 2001.
- Yamaguchi, D.K., Atwater, B.F., Bunker, D.E., Benson, B.E., and Reid, M.S., Tree-ring dating the 1700 Cascadia earthquake, *Nature*, V. 389, 922-923, 1997.
- Yelin, T.S., Tarr, A.C., Michael, J.A., Weaver, C.S., Washington and Oregon earthquake history and hazards, Open-File report 94-226B, 1994.
- Zumberge, J.F., M.B. Heflin, D.C. Jefferson, M.M. Watkins, and F.H. Webb, Precise point positioning for the efficient and robust analysis of GPS data from large networks, *J. Geophys. Res.*, 102 (3), 5005-5017, 1997.

h428		USGS							NGS		RPI	UW/RPI
haff				USGS	UW	UW	UW		NGS	UW		UW/RPI
hall									NGS			
hana												UW/RPI
hans												UW/RPI
hc08									NGS			
hchy									NGS			
hele									NGS		RPI	UW/RPI
heml												UW/RPI
hill												UW/RPI
hiltr												UW/RPI
hs12	USGS											
hur2		USGS					USGS				UW	
hutt							UW					
hyak									NGS		UW	UW/RPI
iceb		USGS					USGS				UW	UW/RPI
iceh									NGS		RPI	UW/RPI
j388												UW/RPI
j464								UW	NGS			
jcia							CVO	UW				UW/RPI
jcro		USGS										
jeff												UW/RPI
jorc												UW/RPI
jord	USGS											
jstc												UW/RPI
k024									NGS			UW/RPI
k061									NGS			UW/RPI
k063									NGS			
k485									NGS			
k64x				USGS								
kaml												UW/RPI
kell									NGS			UW/RPI
kelr									NGS			UW/RPI
kely		USGS										
kend							UW				UW	UW/RPI
kibl							UW					
kima											RPI	UW/RPI
king							CVO	UW	UW			UW/RPI
klas												UW/RPI
klso				USGS					NGS			
koit		USGS		USGS								
l387									NGS			UW/RPI
l467									NGS			

rkbv					USGS	USGS						RPI	UW/RPI
rock								UW		NGS		UW	UW/RPI
rosw													UW/RPI
rs26						USGS							
s262										NGS			
s389										NGS			UW/RPI
s509										NGS			UW/RPI
sadl			USGS										
san2								CVO	UW			UW	UW/RPI
sand			USGS		USGS	USGS	USGS	CVO	USGS	NGS		RPI	UW
sarg					USGS		UW	UW	UW			UW	
sat3										NGS		UW	UW/RPI
satu	USGS												
scho								CVO	UW	UW			UW/RPI
sdro								UW				UW	UW/RPI
seas													UW/RPI
shrh	USGS												
sime										NGS			
sita			USGS			UW	UW	UW	UW				
sjcp													UW/RPI
skuk													PGC
slip			USGS										
slpk													UW/RPI
slug										NGS			
slvr												UW	UW/RPI
smit		USGS											
so25								USGS					
sobe					USGS		UW	CVO	UW			RPI	
sout					USGS	CVO							
span								UW					
spil						CVO				NGS		UW	
spit										NGS			
spoo						USGS		UW	UW			UW	UW
spr4					USGS								
squa													UW/RPI
squm													UW
stal													UW/RPI
stan								UW				UW	UW/RPI
stea				USGS				USGS					UW/RPI
stev			USGS							NGS			UW/RPI
strp													UW
summ										NGS			
sunr						CVO							

t1un								USGS				
t26x								UW				
t31n		USGS		USGS								UW
t550					CVO							
taco							UW	UW				
tahu					UW		CVO	UW			RPI	
taun		USGS										
teno						UW	UW	UW	NGS		RPI	UW
thak												UW/RPI
thu9				USGS								
thun					CVO	USGS	UW	USGS			UW	UW/RPI
ti74								UW				
tigr					USGS			UW			UW	
till	USGS				CVO							
tlmk	USGS											
toby												PGC
toct												UW
tolt					USGS							UW
tomt												UW/RPI
tuck		USGS					USGS					
vanc									NGS		RPI	UW/RPI
vntg												UW/RPI
waad		USGS										
wala									NGS			
wapa												UW/RPI
war2		USGS										
webb					USGS							
wege									NGS			
wil1								UW				
wil2								UW				
wils				USGS		USGS	UW	USGS	NGS		UW	
woaz		USGS		USGS			USGS					
wood												UW/RPI
word	USGS	USGS		USGS		UW	USGS	UW		UW		UW/RPI
wpet												UW/RPI
wtwn		USGS										
wyn1												UW
wyn2												UW
x537				USGS			UW	UW	NGS		UW	
yale				USGS							RPI	UW/RPI
youb	USGS											
z070									NGS			
z231									NGS			UW/RPI

150

z264										NGS			UW/RPI
z478					USGS		USGS		USGS				
zseb										NGS			

Vita

Zuoli Ning was born in China. He earned a Bachelor of Science degree at the University of Science and Technology of China and a Master's degree in Electrical Engineering at the University of Washington in Seattle. In 2003, he earned a Doctor of Philosophy at the University of Washington, Seattle in geophysics.